Robust Feature Extraction and Temporal Analysis for Partial Fingerprint Identification

Nathaniel J. Short

Dissertation submitted to the faculty of the Virginia Polytechnic Institute and State University in partial fulfillment of the requirements for the degree of

Doctor of Philosophy
in
Computer Engineering

A. Lynn Abbott
Edward A. Fox
Michael S. Hsiao
Sandeep K. Shukla
Jason J. Xuan

September 5, 2012
Blacksburg, VA

Keywords: Biometrics, Fingerprint, Bayesian Estimation, Extended Features, Temporal Analysis

Robust Feature Extraction and Temporal Analysis for Partial Fingerprint Identification

Nathaniel Short

ABSTRACT

Identification of an individual from discriminating features of the friction ridge surface is one of the oldest and most commonly used biometric techniques. Methods for identification span from tedious, although highly accurate, manual examination to much faster Automated Fingerprint Identification Systems (AFIS). While automatic fingerprint recognition has grown in popularity due to the speed and accuracy of matching minutia features of good quality plain-to-rolled prints, the performance is less than impressive when matching partial fingerprints. For some applications, including forensic analysis where partial prints come in the form of latent prints, it is not always possible to obtain high-quality image samples. Latent prints, which are lifted from a surface, are typically of low quality and low fingerprint surface area. As a result, the overlapping region in which to find corresponding features in the genuine matching ten-print is reduced; this in turn reduces the identification performance. Image quality also can vary substantially during image capture in applications with a high throughput of subjects having limited training, such as in border control. The rushed image capture leads to an overall acceptable sample being obtained where local image region quality may be low.

We propose an improvement to the reliability of features detected in exemplar prints in order to reduce the likelihood of an unreliable overlapping region corresponding with a genuine partial print. A novel approach is proposed for detecting minutiae in low quality image regions. The approach has demonstrated an increase in match performance for a set of fingerprints from a well-known database. While the method is effective at improving match performance for all of the fingerprint images in the database, a more significant improvement is observed for a subset of low quality images.

In addition, a novel method for fingerprint analysis using a sequence of fingerprint images is proposed. The approach uses a sequence of images captured during a single impression of a fingertip. During the impression sequence, the change in fingerprint representation, as the fingertip is provided to the sensor, is recorded. Minutiae and other features are extracted and tracked throughout the sequence for temporal analysis, reducing the negative results from the variation in image quality during image capture. Instead of choosing a single acceptable image from the sequence based on a global measure, we examine the change in quality on a local level and fuse information from multiple images based on the optimal local quality measures.

Acknowledgements

Thank you to each of my committee members, Dr. Lynn Abbott, Dr. Ed Fox, Dr. Michael Hsiao, Dr. Sandeep Shukla, and Dr. Jason Xuan, for their time and support throughout the course of completing this work. I would especially like to thank my advisor, Dr. Abbott, for the guidance he has offered since I arrived at Virginia Tech almost five years ago. I enjoyed the experience attending conferences together, including the overseas trip to London. I would also like to thank each of the professors I had the pleasure of working with for the past two and a half years, Dr. Fox and Dr. Hsiao. In addition, this work would not have been possible without the support from the remaining members of our research team, Dr. Randy Murch and Dr. Bruce Budowle, as well as our sponsor, the National Institute of Justice (2009-DN-BX-K229).

I would also like to thank all of my fellow graduate students I had the opportunity to work with, Sung Hee Park, Supratik Misra, Kevin Hoyle, Nadia Kozievitch, Indira Priyadarshini, and Lin Tzy Li. To the students I met in CESCA while working in the lab, Mahesh Nanjundappa, Bijoy Jose, and Jake Bruce, it was a pleasure meeting and getting to know you all during my time at VT; all the best in your future endeavors. I would also like to thank my colleague, classmate, and friend, Ryan Triplett; for offering assistance and providing contacts within the biometrics community that have been a benefit to this work.

To my family and friends, thank you so much for all of your thoughts and prayers. I am especially thankful for the unwavering love and support from my mom and dad throughout my time in graduate school.

Finally, to my beautiful bride Courtney, thank you for your patience, support, and encouragement. Thank you for distracting me when I needed a break and encouraging me when I was unmotivated to work. This truly would not have been possible without you.

Table of Contents

LIST OF TABLES

LIST OF FIGURES

Chapter 1

Introduction

"The patterns of the friction skin are individual, and, taken together, impossible to duplicate in another individual. The separate ridges, too, show numerous details, which are also so individual that a small area of friction skin, taken even in the most featureless portion, cannot be matched by any other piece." - *Wilder and Wentworth (1918)*

1.1 Motivation

The unique characteristics that define how a person looks, or physiological traits, have been used for human identification since the beginning of human existence. The most common way that humans recognize one another is by their individualizing traits, especially the appearance of the face. When the visual senses are unavailable or inhibited, we revert to our audible sense to identify people by voice. The measurement or study of the different methods for uniquely identifying humans based on their intrinsic physical or behavioral traits is known as biometrics. Face and voice biometrics are only two of the many traits that can be measured and used for identification.

Physiological traits, which relate to the shape or appearance of the body, include the measurement of a fingerprint, face, hand, or iris, to name a few. Behavioral traits, which relate

to the behavior of a person, include measuring gait, voice, and handwriting. Examples of both physiological and behavioral traits are shown in Figure 1-1 (a-d) and (e-g), respectively. Practically any trait can be used for recognition, but the usefulness of a biometric trait for identification is determined by the factors listed in Table 1-1. The table also shows how each of the major biometric traits exhibits the following factors:

- *Universality*: everyone must possess the trait;
- *Distinctiveness*: the trait must be unique to a single person;
- *Permanence*: the trait should be invariant over time; and
- *Collectability*: the trait can be measured.

A biometric system is a device that can be used to acquire, measure, and match samples of a specific biometric trait. These systems operate in two different modes, identification and verification. In identification, a newly acquired sample from an unknown individual is compared to an entire database of previously collected samples in order to determine the identity of the

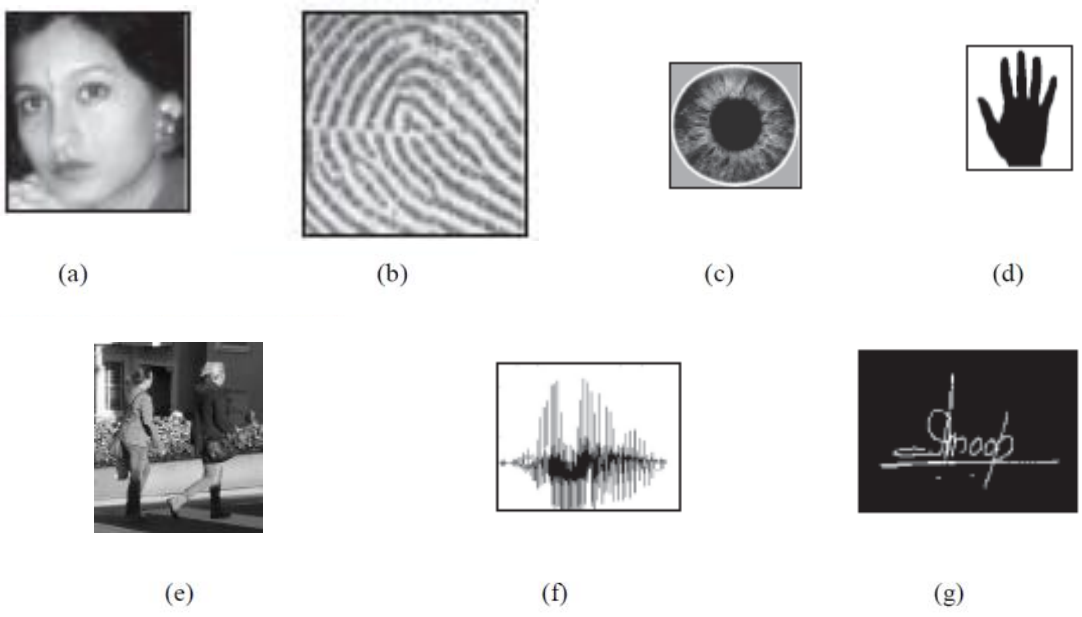

Figure 1-1: A subset of biometric traits: (a) face, (b) fingerprint, (c) iris, (d) hand structure, (e) gait, (f) voice, and (g) signature. (All images, except (e), reproduced from [4])

individual. This is classified as a one-to-many search, as one sample is compared to an entire database of known samples, and answers the question "Who is this person?" In verification mode, a biometric trait is collected along with some user identification information, like a Personal Identification Number (PIN) or user name. The acquired sample is then compared to a known template for the user. This mode of operation is called a one-to-one search, since only the sample print and indexed print are compared, and answers the question "Is this person who they say they are?"

For either identification or verification, the first step in biometric recognition is enrollment. In the enrollment stage, samples are provided from an individual for the respective trait from which a template is created and stored in a database. The template contains discriminating features extracted from the biometric sample. The feature templates describe the structure of the biometric sample and are used for identification or verification with a template generated from the provided sample. The input sample and database samples are referred to as the *probe* and *gallery* templates. In Figure 1-2, a data flow diagram depicts the processes of (a) enrollment, (b) verification, and (c) identification of a biometric sample.

Table 1-1: Biometric traits and fulfillment of requirements for use listed as High, Medium, and Low (H, M, and L).

Requirements	Face	**Fingerprint**	Hand Geometry	Iris	Signature	Voice
Universality	H	**M**	M	H	L	M
Distinctiveness	L	**H**	M	H	L	L
Permanence	M	**H**	M	H	L	L
Collectability	H	**M**	H	M	H	M

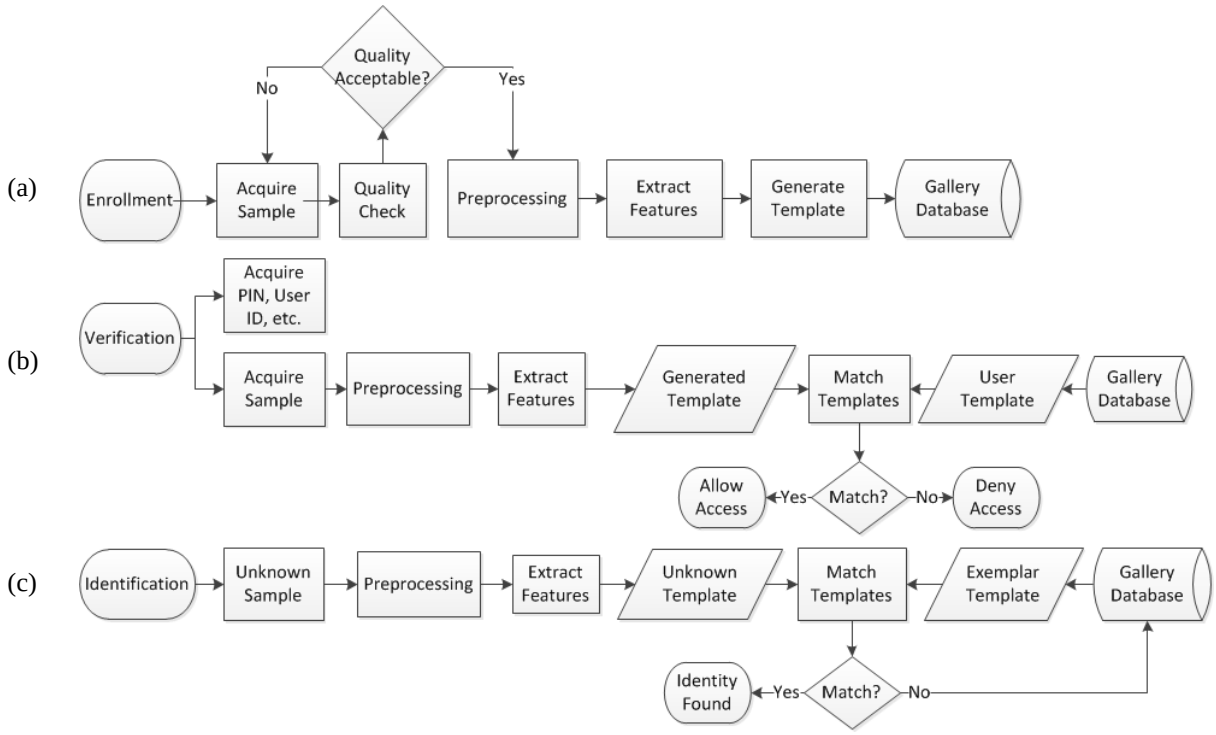

Figure 1-2: A dataflow diagram showing the general workflow of a biometric system for (a) enrollment, (b) verification, and (c) identification.

1.2 Fingerprint Formation

One of the oldest and most reliably used traits for human identification is the fingerprint. Evidence shows that the unique structure of the friction ridge surface found on each person's hands and feet have been used for identification as early as 221 B.C. In China, a clay seal was used on documents with the author's name on one side and his or her fingerprint impression on the other to prove authenticity [9]. Not until 1788 were friction ridge patterns claimed to be unique from person to person [10], a concept that is commonly accepted, but has not actually been proven. The idea of permanence was studied from 1856 – 1897 by Hermann Welcker, who examined the change in an impression of his own fingerprint 43 years apart [11].

Fingerprint features were proposed by Sir Francis Galton in the first book on fingerprints, *Finger Prints*, in 1892 [12]. The features were labeled as Galton details and included uniting and dividing ridges (ridge bifurcations), endings or beginning of ridges (ridge endings), and

enclosures (two bifurcations facing each other). In 1900, the development of the Henry Classification System, a logical method for categorization, spawned the standard practice in England to individualize criminals by fingerprints [13]. Shortly after, in 1902, the first conviction in England was made using bloody fingerprints found on a piece of broken glass at a murder scene [7]. In 1904, fingerprint impressions were taken from all inmates at a federal prison in Kansas, thus beginning the first fingerprint database in the U.S.

The friction ridge surface on the hands and feet has been commonly thought to provide additional friction when grasping objects; however, this line of thinking has recently been questioned [14]. The pattern of ridges and valleys, illustrated in Figure 1-3, is unique and persistent throughout a person's life. The fiction ridge pattern uniqueness is a result of the developmental variability during fetal development. Ridge pattern uniqueness also can be attributed to the position of the hands during development and has been found to be distinctive even in monozygotic twins. While no commonly accepted mechanism for formation currently exists, the size and shape of the volar pad in conjunction with the formation of the epidermal layer is thought to determine the structure of the friction ridge. In the top image of the figure, the primary ridge corresponds to the ridges in the bottom image of the figure and the secondary ridge in the epidermis corresponds to the valleys.

During fetal development, the volar pads on the digital and plantar surface of the hands and feet, shown in Figure 1-4, grow and "regress". The pad, indicated by the dashed red circles, does not actually shrink in size, but the surrounding area growth begins to catch up and the prominence of the volar pad decreases. The time it takes for the pad to regress directly relates to the ridge density, whereas the direction and location of tension in the volar pad during growth is an indication of the class the completed friction ridge pattern will have. The growth followed by regression is shown in Figure 1-4, where the volar pad on a finger starts forming and completely regresses in about eight weeks. In this example, the pad starts out with a uniform shape and then at about 12 weeks, the pad shifts to the upper left of the digit. At this stage, the pattern of the finished fingerprint has changed from whorl type to that of a left loop.

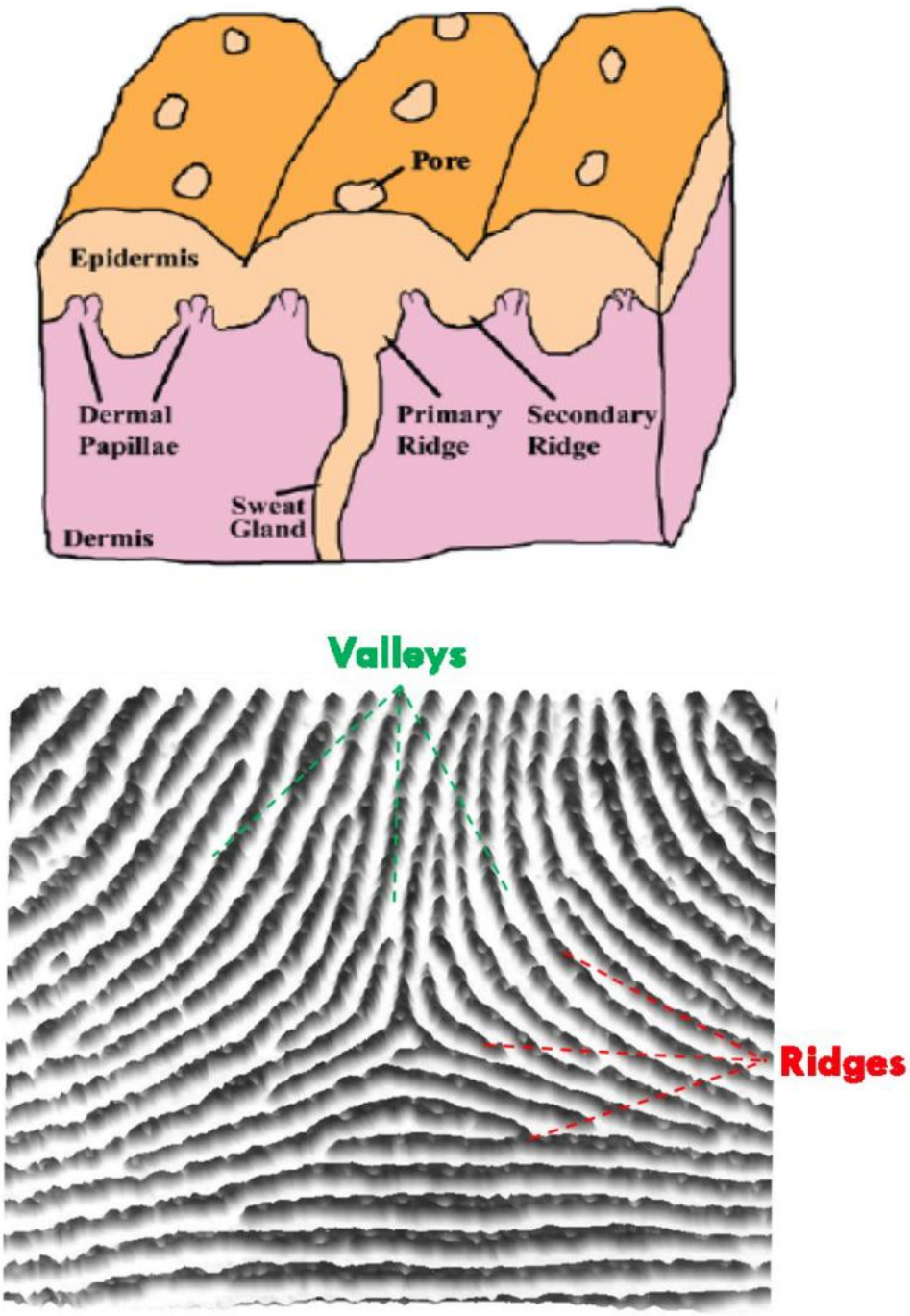

Figure 1-3: Fingerprint ridges and valleys; (top) sub-surface (from [7]) and (b) surface structure.

Figure 1-4: The growth and regression of volar pads (dashed circles) is shown with potential core (green circle) and delta (blue triangle) points.

This shows just how variable fingerprint patterns are, where something as small as the hand position during development can cause the volar pad to be forced to the left or right. In this particular example, the potential locations for deltas and core points are shown as red triangles and green circles, respectively. In the beginning of the formation, two possible delta locations are shown, but as the development progresses, the volar pad shifts to the upper left causing only one prospective delta region to remain.

1.3 Acquisition

Various methods exist for obtaining an impression of an individual's friction ridge surface for enrollment and identification purposes. The choice in acquisition method is sometimes limited due to the context in which the sample is presented. Fingerprint samples fall into two categories as far as presentation, exemplar or latent prints. Exemplar prints, also known as plain, slap, or rolled, are those in which the sample is provided willingly from a known subject. Conversely,

latent prints which may be left inadvertently on various surfaces without any identifying information. A single finger, as represented by these different types of fingerprint presentations, is shown in Figure 1-5.

1.3.1 Exemplar Prints

An exemplar, or known print, is provided by an individual as a sample during the enrollment process. A template is created and stored in a database to be accessed later for verification or identification purposes. Fingerprint enrollment is typically conducted in an environment where quality is controlled and an optimal sample is obtained. The type of print collected can be any subset of the following: plain, rolled, or slap. In a rolled print, each finger is rolled across the acquisition surface from "nail to nail" as defined by the Federal Bureau of Investigation's (FBI) Type-4 impression specification [15]. A plain, or flat print, is provided by pressing the finger flat against the acquisition surface. Included with the plain print in the Type-14 specification for

(a) (b) (c)

Figure 1-5: Example of (a) rolled, (b) plain, and (c) latent impressions of the same finger.

FBI impression types, the slap print is a simultaneous flat capture of the four fingers (index, middle, ring, and little) of either hand. The FBI standards for capture are as specific as the ideal finger sequence during acquisition all the way to an optimal height for the capture surface to be set off the ground.

Due to the larger surface area provided by rolled prints, as shown in Figure 1-5, more features can be extracted for matching purposes than in plain prints, with a tradeoff in enrollment time. However, due to the non-uniform pressure applied during capture of a rolled sample, features located in the outer region of the rolled print can suffer from distortion. The variation in pressure magnitude and direction, in conjunction with the elastic property of the skin, causes stretching and compressing of the fingerprint during capture. The distortion is typically more severe towards the outer region of the contact area.

Traditionally, exemplar prints are captured off-line by placing the finger in ink and then pressing or rolling the finger onto a paper card. More recently, electronic live-scan devices are being used to capture static fingerprint impressions on-line. Figure 1-6 shows an example of an off-line ink and on-line live-scan capture of the slap-type fingerprint impression from the same hand.

The most popular live-scan devices for law enforcement applications are optical scanners. Optical sensors are able to collect fingerprint images at both the American National Standards Institute (ANSI) and the National Institute of Standards and Technology (NIST) required minimum image resolution of 500 pixels per inch (ppi) [3]; however, some are designed to collect at a higher resolution of 1000 ppi. The obvious benefits to higher resolution images relate to the level of detail visible in the sample, from which additional feature types can be extracted. The same fingerprint region is shown in Figure 1-7 at three different resolutions to demonstrate the level of detail.

Figure 1-6: Example of off-line ink (top) and on-line live-scan (bottom) slap prints from the same hand.

(a) (b) (c)

Figure 1-7: Same fingertip scanned at (a) 250 dpi, (b) 500 dpi, and (c) 1000 dpi (images from [4]).

An example of an optical fingerprint device, digID mini from Identification International Inc. (i3) is shown in Figure 1-8 (a). This device can acquire FBI Type-4 and Type-14 [16] impressions at 500 ppi and is powered by a computer through a USB connection [17]. The low power requirements (1.9W max and 500 mA) allow the unit to be highly portable for field applications [18]. The i3 digID mini is a Frustrated Total Internal Reflection (FTIR) based sensor, the oldest and most commonly used live-scan technology.

In an FTIR live-scan device, a light source is used to illuminate a glass prism in contact with the finger. The ridges in the fingerprint pattern make contact with the prism surface, whereas the valleys allow an air gap. The contact from the ridges causes the light to be scattered or absorbed while the gaps from the valleys cause the light to be reflected. A Charged Coupled Device (CCD) or Complementary Metal-Oxide Semiconductor (CMOS) image sensor is placed at the other side of the prism to capture the reflected light. A higher intensity of light is measured by the sensor from the reflected light than the scattered/absorbed light. This contrast in light intensity is represented with ridges and valleys as low and high grayscale intensities, respectively. A diagram of the FTIR technology is shown in Figure 1-8 (b).

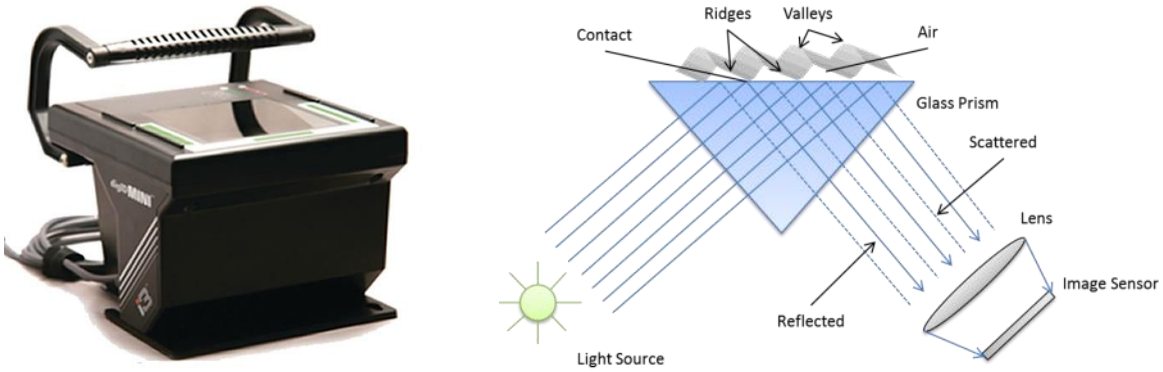

(a) (b)

Figure 1-8: (a) The i3 digID mini optical live-scan device (reproduced from [1]) and (b) diagram of FTIR-based acquisition technology.

1.3.2 Latent Prints

The term “Latent” is used to define a chance or accidental friction ridge impression left by the natural sweat of the skin or from any other kind of contaminant such as oil, blood, ink, or paint. In comparison to exemplar prints, the quality of latent print samples cannot be controlled. A visible friction ridge skin impression, referred to as a patent print, can be photographed for processing. However, latent prints are not visible and need to be made such by chemical or physical means. According to the Virginia Department of Forensic Science, the following can be used for detecting and acquiring, or “lifting”, latent prints: inherent luminescence, ninhydrin, cyanoacrylate ester, powder, and adhesive surfaces [19]. All of these methods apply a substance that will react with one of the chemicals found in the latent print residue to make it visible for photographing.

Due to the luminescence of substances found in friction ridge residue, alternate light sources have proven to be effective methods in visualizing latent impressions. One common method is through the use of lasers as proposed by Menzel and Duff [20]. Ninhydrin is used as an indicator from a chemical reaction with amino acids and proteins, which are commonly found in the oils left by the friction ridge surface. The process requires the indicator to be applied to the sample, either through soaking or brushing, and then exposing the sample to heat to reveal the impression. This method is outlined by Lee and Gaensslen [21]. Cyanoacrylate esters, commonly found in bonding adhesives, can be applied to the invisible impression inside a vacuum chamber as a fume. The fume reacts with moisture in the air and proteins in the fingerprint residue to form a visible white substance on the ridges of the impression. This method was documented by Lee and Gaensslen [22]. Powders can be applied to the surface that will adhere to the residue left behind by the fingerprint; the free powder is brushed away. Finally, fingerprint impressions can be physical lifted off a surface using adhesive material, such as tape. Of these methods mentioned, laser scanning is the most widely used as it is a non-reactive technique; providing the benefit over chemical techniques of not disturbing the authenticity of the latent print.

Figure 1-9 shows examples of some of the latent fingerprint acquisition techniques previously mentioned. In (a), an orange powder has been dusted onto the fingerprint surface. To enhance the color of the powder, a blue cut-off filter is used when photographing the fingerprint to block the blue visible light band. In (b), a fingerprint lifted from an object is transferred using an adhesive tape method. Figure 1-10 shows simulations of latent fingerprints visible on various objects. The prints were left by placing the fingers in ink and transferring the prints to the objects by grasping them in various ways. An adhesive tape method was used to simulate lifting the latent prints.

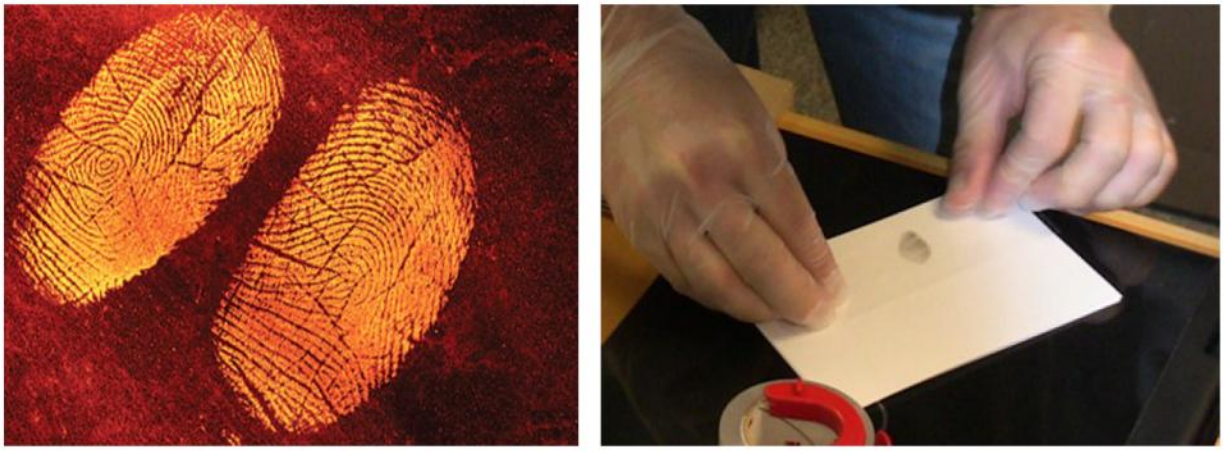

(a) (b)

Figure 1-9: Examples of (a) fingerprint dusted with orange powder and photographed with blue cut-off filter (reproduced from [2]) and (b) latent print being transferred with adhesive method.

Figure 1-10: Examples of visible fingerprints left on various objects.

1.4 Features

Once a fingerprint has been acquired, it is not simply compared pixel-by-pixel with a collection of known prints, due to the sensitivity of individual pixels to noise. A more robust subset of features representing the fingerprint image is found for the purpose of matching. There are three common feature type levels, which are determined by the available detail level, dependent on the resolution of the image. These levels are described in Figure 1-11 with the resolution required to extract features in each level shown in Table 1-2.

The first level of detail contains the ridge pattern information, which describes the flow of the ridges and valleys in a given region of the image. These features can be used for fingerprint classification (pattern type) and exclusion (non-match), but not for identification itself, as outlined in Table 1-3. The six classes of fingerprints are, as shown in Figure 1-11 (top), double loop, whorl, left loop, right loop, arch, and tented arch [4]. All fingerprints fall into one of these classes. This low level of detail can be used to filter, or exclude, gallery prints that do not belong to the same class as the probe template. As indicated in Table 1-2, the minimum resolution required to determine class type is 250 ppi.

The second detail level contains a set of feature points that can be used for matching fingerprints; these points are referred to as minutiae and are the discriminating features unique to each finger [3]. The presence or absence of a minutia type does not determine the similarity of two prints, but rather the distribution, or patterns, exhibited by a set of minutiae present in the fingerprint image. The features in this level mark the discontinuities of the ridges throughout the image. Examples of these features are shown in Figure 1-11 (middle) and include terminations, bifurcations, spurs, lakes, islands, and short ridges. This level of detail requires a scan resolution of 500 ppi for extraction.

The final level of detail, requiring 1000 ppi resolution, also can be used for identification. Due to the high resolution of the fingerprint images at this level, more detail can be extracted. The added detail allows for additional sets of features to be extracted, adding to the discriminatory power of the fingerprint features. Examples from the extended feature sets found in the level 3 details are shown in Figure 1-11 (bottom): pores, ridge shapes, incipients, creases, warts, and scars.

While Table 1-2 shows the minimum FBI standard resolution required for extracting the respective features, in theory it is possible to extract higher level features at lower levels of detail. For example, a ridge discontinuity can be seen at 250 ppi, but the type might not be known. Also, an incipient ridge or scar can be visible in a clear 500 dpi fingerprint image, but the accepted FBI standard for Level 3 details is 1000 ppi. The benefit of higher resolution is the reliability and precision of the extracted features. The drawback of higher resolution is the increased processing time and database storage costs.

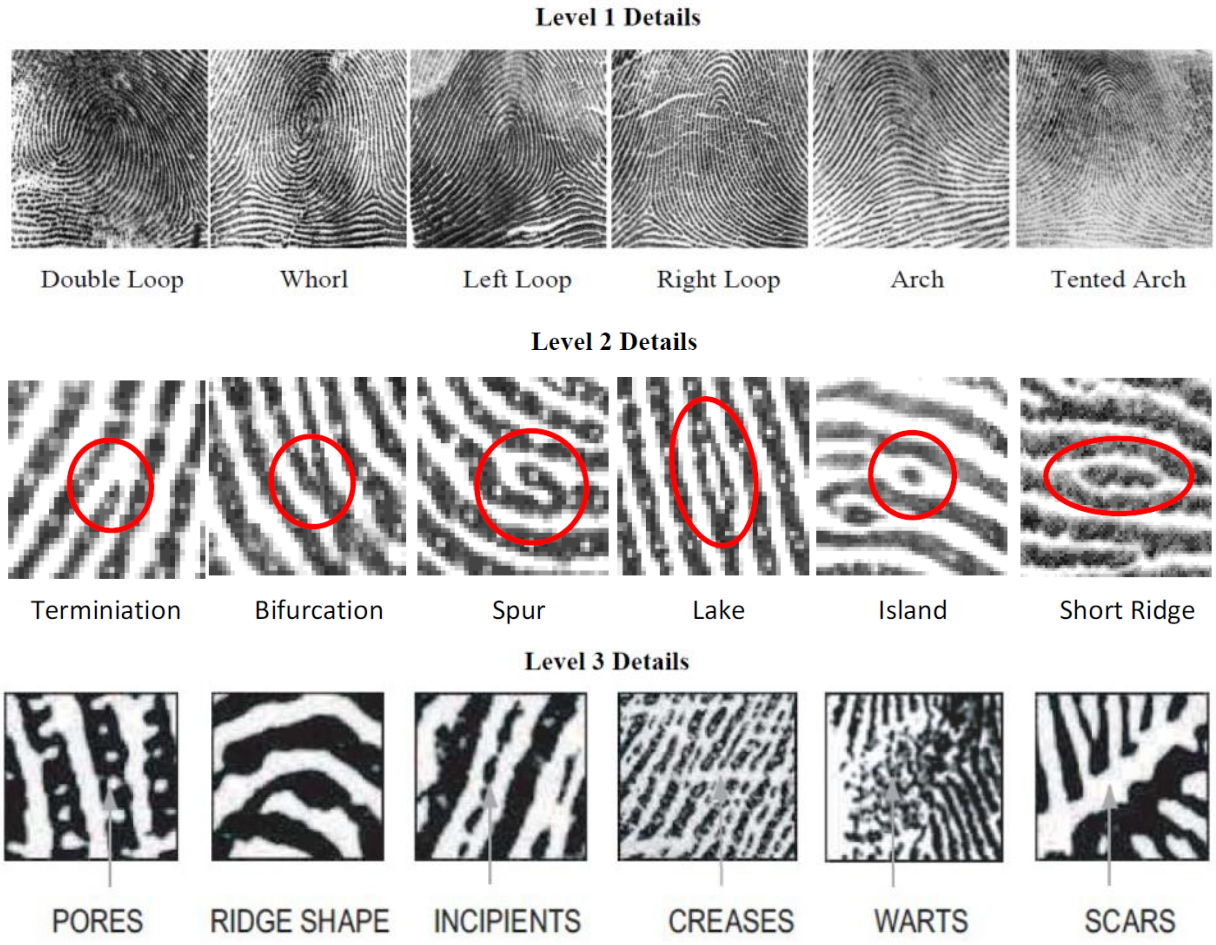

Figure 1-11: Level 1 (top), Level 2 (middle) and Level 3 (bottom) details for features used in fingerprint matching. (Level 3 details reproduced from [4])

Table 1-2: **Required minimum resolution for fingerprint feature classes**

	Minimum Resolution (ppi)
Level 1	250
Level 2	500
Level 3	1000

Table 1-3: Required minimum resolution for match determination.

	Minimum Resolution Required (ppi)
Classification	250
Exclusion	250
Identification	500

1.5 Analysis

After a fingerprint has been acquired, be it a plain, rolled, or latent print, the sample is examined and the identifying features are found for matching. These features create a template for the probe image and are compared to a database of gallery templates to determine feature correspondences. The similarity of a fingerprint is determined by the quality and quantity of matched features between the probe and gallery templates. There are three methods for processing fingerprints to extract and match features; manual, automatic, and semi-automatic. For each of the three types of examination, there is a tradeoff between processing time and accuracy.

1.5.1 Manual Examination

Manual examination has been a reliable means for feature detection since fingerprints were first used for identification purposes. Identifying features are manually marked by an experienced fingerprint examiner and compared to those from known prints. Initially, forensic latent examiners relied on a "point rule" to match fingerprints, which declared two fingerprints to be matching if at least 12 corresponding minutiae were found. This method has been abandoned for a more structured method, the ACE-V protocol [23]. The acronym ACE-V represents the four

stages involved in manual fingerprint examination: Analysis, Comparison, Evaluation, and Verification.

In the analysis phase, the fingerprint is examined and features are annotated manually. Latent examiners assess all three levels of detail to determine if there is sufficient quantity and quality of information to proceed to the comparison phase. The manner in which the impression was left (direction and pressure), on what surface, and a description and cause of any visible distortion is evaluated. In the comparison phase, the features found in the unknown print are compared to a set of exemplar prints. This process is known as a "back and forth" examination as it involves examining a subset of features in an unknown print and then looking for similar features and arrangements in the known prints. If the known print exhibits similar features, the unknown print is then examined again for another subset of the features for comparison. In this phase, knowing the Level 1 details of the unknown print can be used to easily eliminate prints of different class types from further, often more detailed, examination. The confidence in the judgment made and levels for acceptance are solely based on the experience and skill of the latent examiner. Once a sufficient number of features between two prints are in agreement, the methodology proceeds to the evaluation phase. In this step, the decision of identification, exclusion, or inconclusive is made based on the agreeing features.

The decision of inconclusive is made if there is insufficient quality or quantity of features to be able to determine a match or non-match. This also can occur if the amount of overlap between the two prints is not enough to obtain a sufficient number of features to make a decision. Exclusions can be made if a single indisputable genuine discrepancy in the features of the exemplar and latent print exists. However, to determine identification, a sufficient number of features with a high level of confidence must be in agreement between the two prints, such that the possibility of chance occurrence is miniscule. Finally, a verification phase is conducted where an independent examination of the ACE phases is repeated by second examiner. If the two conclusions are in agreement, the decision is accepted as final. For conclusions that are in disagreement, conflict resolution procedures must be followed which are outlined by individual agencies.

1.5.2 Automated Examination

Automated fingerprint matching begins with the automated process of template creation from extracted fingerprint features. The templates are used to compute match scores from two different fingerprint images through the use of computer algorithms. While manual fingerprint examination utilizes all levels of detail available in the image, automatic fingerprint matching relies heavily on the matching of points, namely minutiae. On a global level, automated fingerprint matching comprises three main steps: 1) minutiae extraction, 2) template alignment and determination of minutiae correspondences, and 3) computing match scores based on the similarity of the two templates.

Figure 1-12 demonstrates the steps involved in automatic fingerprint identification. In (a) and (b), minutiae are found and templates are created for probe and gallery images. In (c), the minutiae from both fingerprint templates are aligned using optimal transformation parameters. This step essentially transforms the minutiae set from the query image into the coordinate system of the minutiae for the gallery image. The minutiae in (a), (b), and (c) marked with green circles represent the reference point for which the optimal transformation parameters were found. The probe image is aligned with the gallery image based on the differences in position and angle of these matched reference points. In (d), the minutiae from both fingerprints are represented in the same coordinate system. The dashed black circles indicate corresponding minutiae pairs. Due to some nonlinear distortions in fingerprint ridge structure, minutiae do not always align perfectly, so some tolerance is allowed for determining corresponding minutiae.

When a sufficiently large number of sample minutiae are present in both fingerprint images, Automatic Fingerprint Identification Systems (AFIS) matching can be performed with a high degree of accuracy. When image quality is poor, resulting in few minutiae, the performance of minutia-based matching degrades. This is often the case when attempting to match latent prints to exemplars.

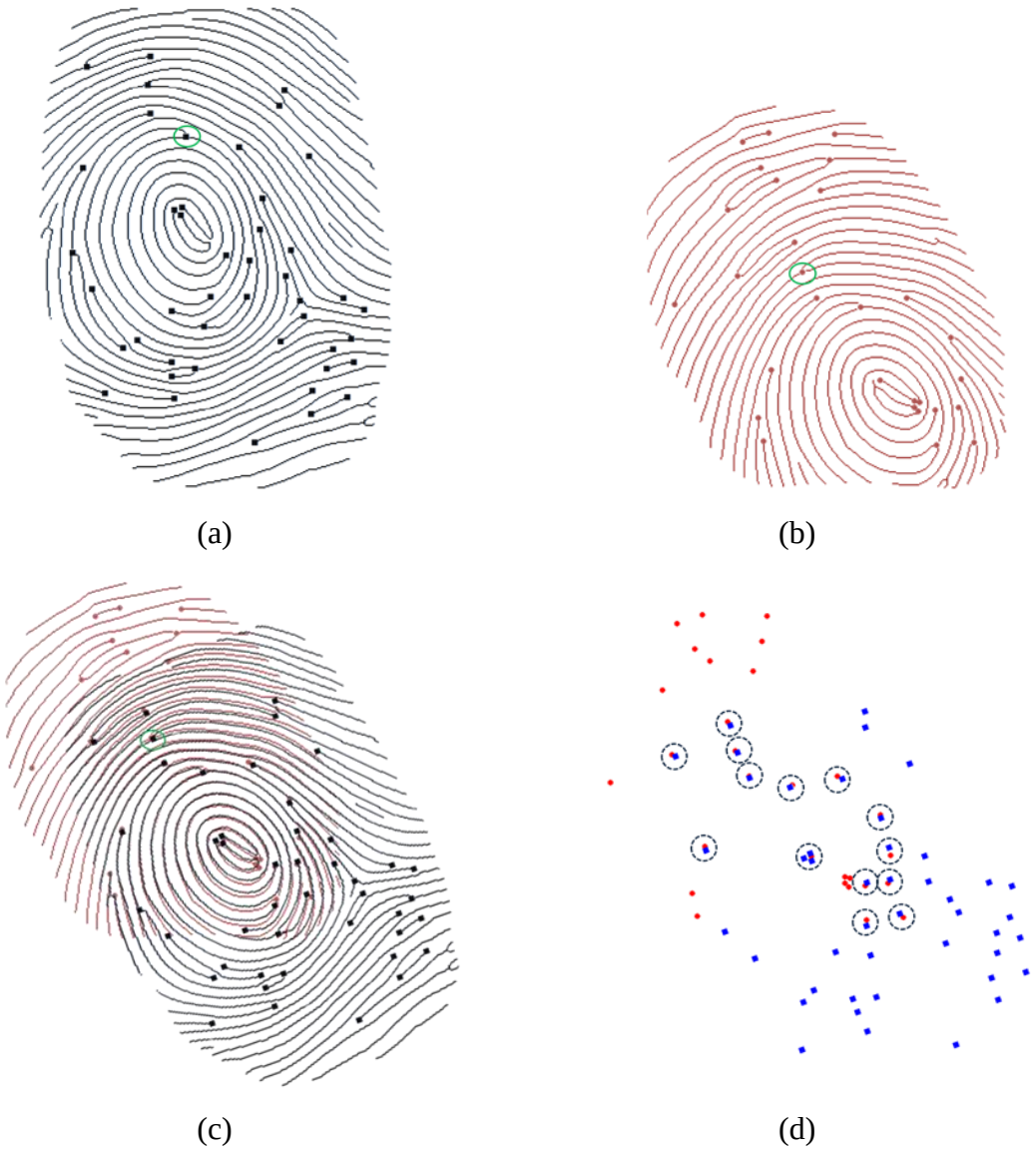

Figure 1-12: (a) A gallery fingerprint image and (b) a probe fingerprint image with minutiae marked. (c) Probe image is transformed into coordinates of the gallery image based on the optimal alignment parameters. In (a) – (c), the green circle indicates the reference minutia from which all points are transformed. (d) Minutiae points from both fingerprints are represented in the same coordinate system.

1.5.3 Semi-Automated Examination

The final method of identification combines the accuracy of manual examination with the speed of automated matching to improve latent fingerprint analysis. Typically, exemplar prints are of high quality and can benefit from the speed of AFIS without sacrificing much performance during feature extraction. However, AFIS feature extraction in latent prints is extremely unreliable, so the prints are manually examined and features are marked to create a template. In semi-automatic examination, the manually encoded latent print is matched with the automatically encoded exemplar print by means of an AFIS matcher. Tools exist for assisting in latent print encoding, such as the Universal Latent Workstation [24]. This software allows a user to annotate, classify, and mark a fingerprint's Level 1, 2 and 3 details. The generated template then can be submitted to a database to be identified.

Even with manual extraction and automated matching, latent print identification performance suffers in comparison to its exemplar print counterparts. matching of latent print only has been able to achieve a rank-one identification rate of 54%, using a database of more than 40 million, according to NIST [25]. Conversely, the Fingerprint Vendor Technology Evaluation (FpVTE) reports a state of the art AFIS can achieve a rank-one identification rate of more than 99.4% on a database of 10,000 plain fingerprint images [25]. Here, a rank-*n* identification rate measures the frequency in which a correct match is present in the top *n* match scores returned by the matching system.

1.6 Measuring Performance

To assess the usefulness of a biometric algorithm, in this case fingerprints, performance tests are executed on a database of known fingerprint images. Typically, the testing samples are composed of multiple impressions of the same fingerprint so that true match scores and false match scores can be determined. The algorithm produces a score that represents the similarity of the two templates; based on empirical thresholds or supervised learning methods [26-28], the score is determined to be a match or not.

1.6.1 False Accept and False Reject Rates

The set of scores is separated into an imposter distribution and a genuine distribution for the entire database. The imposter distribution is the set of scores belonging to matches between two fingerprints belonging to different fingertips. The genuine distribution is the set of scores belonging to the matches between two impressions of the same fingerprint. Examples of these two distributions are shown in Figure 1.13 (a). In the figure, the threshold *t* is set so as to minimize the False Accept Rate (FAR) and the False Reject Rate (FRR). These are the rates at which an imposter match score is accepted and a genuine score is rejected based on the threshold set, respectively.

1.6.2 Receiver Operator Characteristic Curve

A common way to show performance is to plot the FAR vs. the FRR at different scoring thresholds. This is called a Receiver Operator Characteristic (ROC) curve and indicates the number of false positives and false negatives. Depending on the application, a threshold can be chosen to allow for a lower FRR at the expense of the FAR or, for more secure applications, decreased FAR and increased FRR. Figure 1.13 (b) shows an ROC curve and the acceptable rates for various applications. The Equal Error Rate (EER) is shown, which indicates where the FAR equals the FRR, and is commonly used as a performance metric. In the examples, the shaded regions under the imposter and genuine distributions simply indicate the FRR and FAR given the decision threshold, *t*.

1.6.3 Cumulative Match Characteristic Curve

Another performance chart that can be used to indicate performance is a Cumulative Match Characteristic (CMC) curve. This plot measures the percentage of correct matches that are found at each rank-*n*. The rank number is the allowable number of images returned as a match.

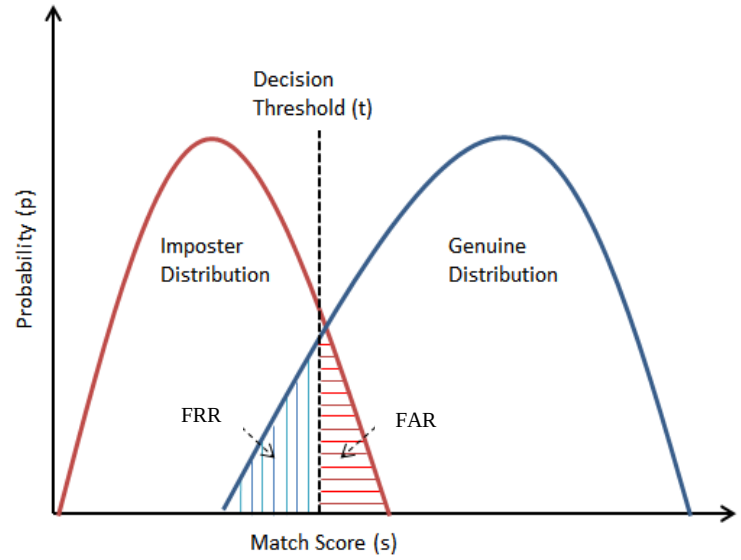

(a)

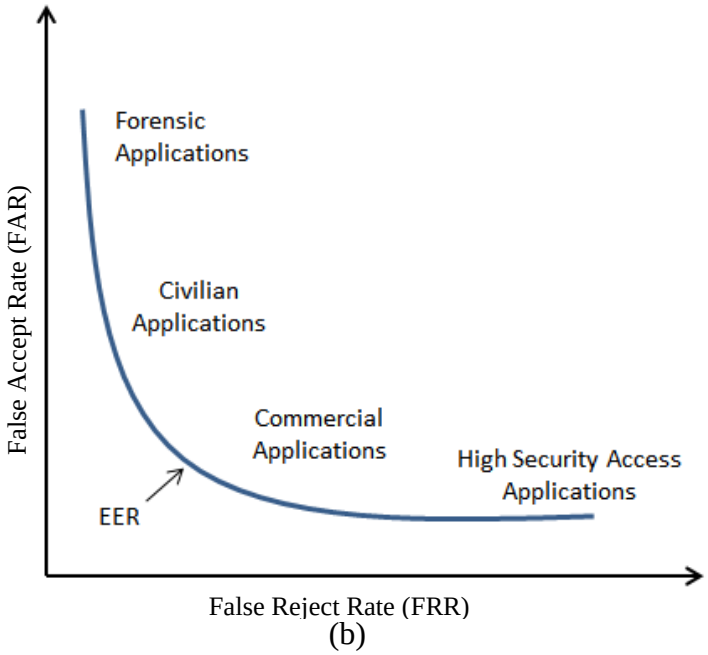

(b)

Figure 1-13: (a) Imposter and Genuine score distribution and (b) a ROC curve showing acceptable levels for various applications.

Typically, the chances of the correct match being included in the top *n* scores returned increases as the rank number increases. This is an important performance measurement for latent fingerprint matching as it is critical that the correct identity be returned within the top *n* matches.

1.7 Organization of Dissertation

The remainder of this dissertation is organized as follows. In Chapter 2, we introduce background details on the formation of fingerprints and the features contained within them. These features are broken down into three groups, each of which holds a certain level of detail that can be used to analyze the fingerprint. Chapter 3 discusses the features in the fingerprint that hold the most discriminatory power, the minutiae. Here, we describe a novel approach to extracting fingerprint ridges and minutiae from low quality regions [29, 30]. Also, we define a method to reduce the variance in minutia placement resulting from detection in different extraction routines [31, 32]. Both methods are aimed at robust feature extraction in low quality fingerprint regions.

In Chapter 4, the usage of extended features, namely ridges, for partial fingerprint matching is introduced [33]. We provide a scheme for extraction and representation of the interconnections formed between minutiae with respect to their adjacent ridges. Chapter 5 continues the discussion on extended features by looking at the sufficiency of ridge features for measuring similarity between partial and rolled prints [34]. In Chapter 6, a novel approach to analyzing fingerprints is proposed [35]. This approach addresses the variation in image quality during image capture by analyzing temporal data contained within a sequence of images taken during a fingerprint impression. Finally, Chapter 7 provides summary and key contributions of the dissertation followed by concluding remarks.

Chapter 2

The Fingerprint

2.1 Introduction

While it is possible to match fingerprints using image-to-image correlation techniques [36-40], more ordinarily a set of features is extracted that characterizes each print. Fingerprint features range from a general description of the friction ridge flow patterns to more discriminating features such as the locations of minutiae within the print. Currently, the FBI standard for AFIS is to reduce a fingerprint image to a "template" which contains these representative salient features, well known for their capability to classify and identify their corresponding fingerprint and for their permanence [41, 42]. Fingerprints can be accurately classified and identified using only these two levels of detail; however, an additional level of detail is commonly used in latent cases where there is a limited amount of level 1 and 2 details available. Level 3 details describe the group of features belonging to a ridge, such as sweat pore placement, edge contours, width, shape, breaks, and creases.

The inevitable tradeoff that comes with the rapid development of automated fingerprint recognition is that the algorithms for feature extraction, representation, and matching are proprietary. Commercial developers earn money by continually improving match performance and speed, all the while not revealing their trade secrets. This type of competition leads to interoperability of fingerprint systems among vendors. In other words, a vendor could only allow for the use of proprietary hardware and software for fingerprint authentication applications. This includes acquisition, extraction, and matching of fingerprints as an all-in-one solution. To the consumer's benefit, standards have been proposed for the exchange of

fingerprint data, allowing for a more adaptive environment where tools from multiple vendors can be used together to create a custom solution.

2.2 Feature Types

2.2.1 Level 1 – Class Type

The "Henry Classification System" [13] is typically used for classifying ridge flow patterns in a fingerprint. Six of the pattern classes — right/left loop, whorl/double whorl, and arch/tented arch — used in this system are shown in Figure 2-1 along with the singularity points used to derive the appropriate class. Red circles indicate core points, a point around which a group of ridges "loop" around in the fingerprint image. Cores are marked at the focus of the innermost recurving ridge, but not on the ridgeline itself. The direction of the core is marked as the ridge flow direction. Delta points are indicated by a green triangle and mark where a group of ridges diverge into three different directions, forming a triangle-like pattern. A delta is marked at the center of the delta formation with directional descriptors in the directions of each of the three ridge flows.

From Figure 2-1, it can be seen how the location and appearance of the singularity points are indicative of the class of fingerprint. For example, right loops always have exactly one delta point and one core point, in order from left to right, with the opposite being true for a left loop. A whorl always has two deltas and an arch has a delta with a core point directly above it. For a plain arch, no prominent core or delta points are present. This information is summarized in Table 2-1. While level 1 features are useful for classification and indexing purposes, they are not sufficient for making an identification or exclusion from within the same class. For the special case where a delta is not visible in the fingerprint image, however, a reasonable estimate to the location can be made, and a virtual delta is marked.

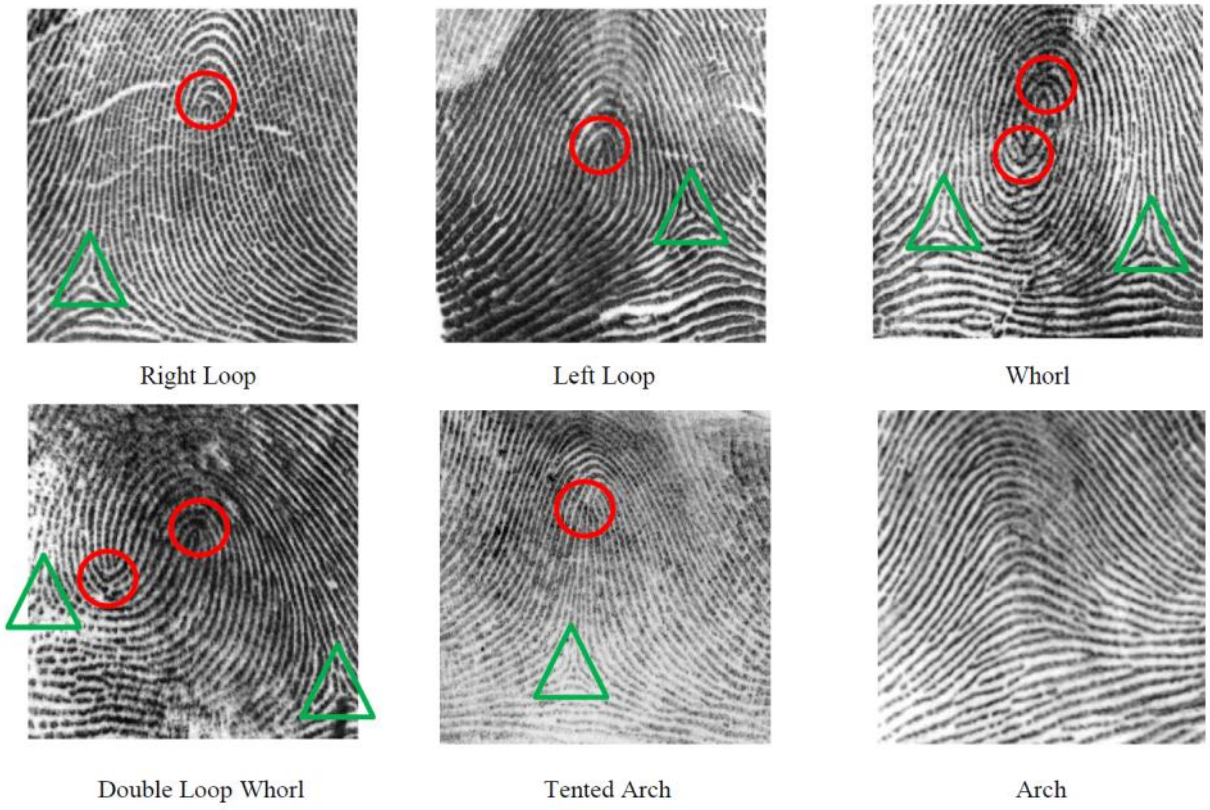

Figure 2-1: Singularity point location for six fingerprint class types. Red circles indicate core points and green triangles indicate deltas.

Table 2-1: Fingerprint pattern type and singularity point correspondence.

	Pattern Class	# Cores	# Deltas
Arches	Plain	0	0
	Tented	0 or 1	0 or 1
Whorls	Plain Whorl	1 or 2	2
	Central Pocket Loop	1 or 2	2
	Double Loop	2	2
	Accidental Whorl	N	N
Loops	Left and Right	1	1

The distribution of fingerprint class types is heavily skewed towards the left loops, right loops, and whorls, with each of these three classes being relatively equally represented within the population. From [43], the distribution of pattern class types found in 222 million rolled fingerprints are: 31.7% for right loops, 33.8% for left loop, 27.9% for whorls, 3.7% for arches, and 2.9% for tented arches.

2.2.2 Level 2: Individualizing Features

Since matching an entire fingerprint image to another would be extremely time intensive, the friction ridge surface is reduced to the places where the ridges terminate or merge. These features, known as Galton details [12], are shown in Figure 2-2 and include ridge endings, bifurcations, lakes, incipient ridges, islands, spurs, and crossovers. Terminations (ridge endings) and bifurcations (convergence/divergence points) are the two fundamental minutiae from which all other level 2 features can be inferred.

The spatial relationship of the set of features within the print has the discriminatory power to identify two fingerprints as matching or non-matching. The distribution of features within a fingerprint is accepted to be unique, even among twins, as well as permanent throughout one's lifetime. Champod et al. [44] report the occurrence of select features described in Figure 2-2; a reproduction of the results is shown in Figure 2-3. The results are representative of a database containing 977 rolled fingerprints and show that the most common minutiae types are termination and bifurcation.

For each minutia that is found, a set of additional descriptors can be found to be associated with the point. In addition to the *x*- and *y*- position of the minutia in the image, a directional angle, quality (reliability), and type are commonly found. A feature vector containing these descriptors is created for each minutia, and the set of vectors make up the fingerprint template. The direction is dictated by the ridge flow direction at the minutia and the quality is inferred from the clarity of the local region of the fingerprint image in which the point lies. Minutia type is simply labeled as being a termination, bifurcation, or unknown.

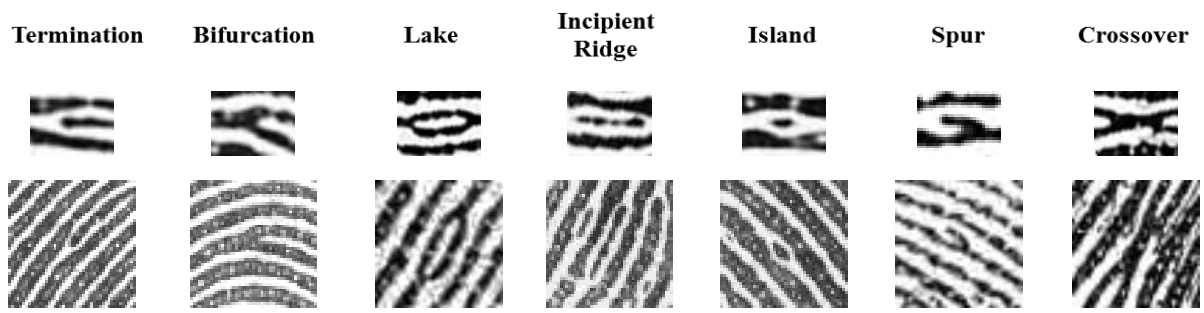

Figure 2-2: Seven of the most common minutiae types; all can be derived from the location of termination and bifurcations.

Typically, more than 100 minutiae can be found within a good quality rolled print; however, it is commonly accepted that the spatial and angular information from as few as 12-15 features is sufficient to determine a match with a high level of confidence. In addition, the number of minutiae found varies from one finger to another. For example, the thumb typically contains more surface area from which to detect minutiae than does the little finger. Figure 2-4 shows the typical minutia count distributions as a box and whisker plot for the thumb, index, middle, ring, and little finger for both the right and left hand. On average, the thumb has 27 more minutiae than the little finger, 151 and 124, respectively. The index, middle, and ring fingers have 135, 140, and 142 minutiae, respectively.

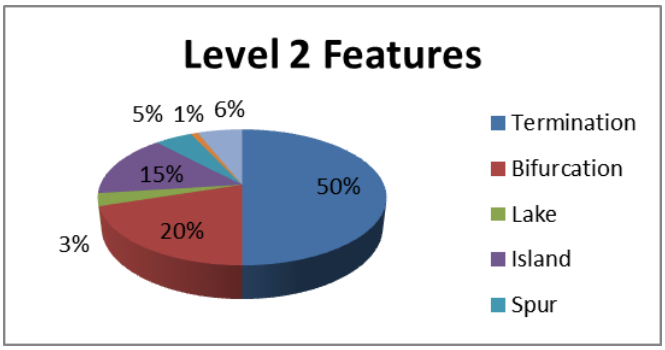

Figure 2-3: Percentage of minutia types found in 977 rolled fingerprint images [5].

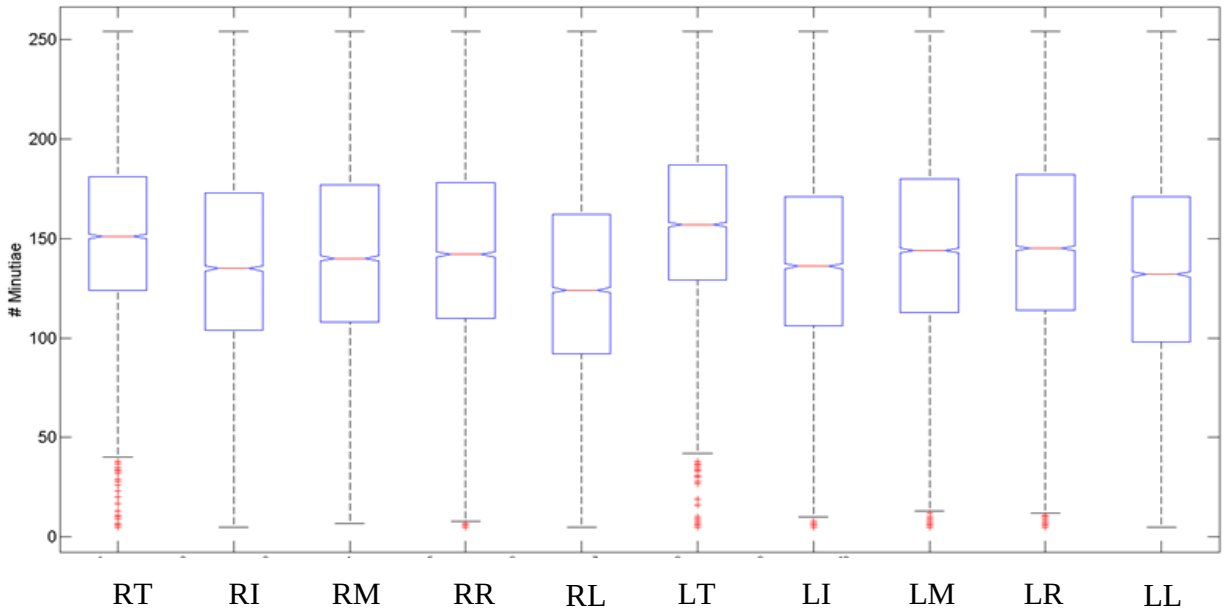

Figure 2-4: Minutiae distributions by finger type for 66,580 evenly distributed, Right Thumb (RT), Right Index (RI), Right Middle (RM), Right Ring (RR), and Right Little (RL). The same also is shown for the left hand (L).

2.2.3 Level 3 – Extended Feature*s*

At level 3, the most local features of the fingerprint are defined. At such a fine detail level, all dimensional attributes of the ridges are available including: width, shape, edge contour, pores, incipient ridges, breaks, creases, and scars. Pores are small openings in the epidermis (outer skin) along the ridges and serve the purpose of releasing sweat. These pores range in size from 60 to 250 μm and occur at a rate of 9 to 18 pores every centimeter. Incipient ridges form within the valleys of the fingerprint. During fetal development, the growth of the finger provides room for additional ridges to form on the skin. An incipient is a ridge that did not completely grow into a full ridge before the end of development.

It is thought that level 3 features have a high discriminatory power for matching fingerprints. However, quite often it is impossible to reproduce level 3 features as their visibility greatly depends on the quality of the obtained image. In the case of latent prints, it is highly unlikely that a great deal of level 3 details will be available, although it is not uncommon for

latent examiners to use the information if it is available and guidelines exist for marking extended feature sets in friction ridge images [3].

2.3 Interoperability

Since minutiae can be extracted using different methods, it is necessary to adopt a standard representation for template files to promote interoperability of matching algorithms. In short, the fingerprint templates created from feature extraction must fit a set standard in order to be used as input for fingerprint recognition software that did not generate the file. There are two such standards used in AFIS, the ANSI/NIST-CSL 1-2011 standard [3] and the FBI's Electronic Biometric Transmission Specification (EFTS) [45] standard representations. In the ANSI/NIST standard, four types of minutiae are defined: 1) ending, 2) bifurcation, 3) compound, or 4) undetermined. NIST has shown through the Minutiae Interoperability Exchange Test (MINEX) [41] and the Proprietary Fingerprint Template (PFT) Test [46] that using standard minutiae templates leads to better matching performance, reinforcing the efficacy of fingerprint standards.

NIST has defined a standard describing the content, format, and units of measurement for electronic exchange of various biometric modalities and descriptive information [47]. In this data format standard, Type-9, Type-13, and Type-14 are related to fingerprints. In the Type-9 record of a given transaction, the exchange of minutiae or other friction ridge feature data is listed. Type-13 records contain fixed and user-defined textual information fields relevant to the latent image, which also is included in the record. The scanning resolution for a latent contained in this record is required to be at least 1000 ppi. Type-14 image records contain fingerprint image data along with fixed and user-defined textual information fields relevant to the image. This record contains the exemplar rolled and plain prints and is recommended to be 1000 ppi with a minimum resolution of 500 ppi. Typically, a transaction includes ten rolled impressions of the fingers along with plain impressions of both thumbs and slap prints of the left and right four fingers.

Figure 2-5 shows an example of a termination and a bifurcation and their representations in both standards. This information would be found in the Type-9 record described above. In (a), a termination is shown and marks a point on the friction ridge surface where a ridge ends. In

(b), a bifurcation is shown and marks a point on the friction ridge surface where two ridges merge or diverge. The *x*- and *y*-coordinates are encoded differently for each standard as well as the orientation of the minutia. The ANSI/NIST position encoding is defined by:

$$x_{ANSI/NIST} = \frac{x}{r} \times 100, \tag{2.1}$$

$$y_{ANSI/NIST} = h \times r - (y \times r) \times 100 - 1 \tag{2.2}$$

and the FBI's EFTS encoding is defined by:

$$x_{FBI/IAFIS} = \frac{x}{r} \times 100, \tag{2.3}$$

$$y_{FBI/IAFIS} = \frac{y}{r} \times 100. \tag{2.4}$$

Here, *r* is the resolution in pixels per millimeter at which the image was scanned and *h* is the height in pixels of the image. The values of *x* and *y* correspond to the pixel coordinates within the image. The main difference between these two standards is that the ANSI/NIST standard measures the minutia location from the bottom left of the image while the FBI's EFTS is measured from the top left of the image.

In Figure 2-5, examples for standard minutia (red circle) direction are shown for a termination (a) and bifurcation (b) feature. The figure shows the direction for ANSI/NIST (yellow) and FBI's EFTS (green). For both standards, the angle is measured in degrees with 0 degrees pointing horizontally out from the minutia and directly to the right (white arrow). The angles are measured incrementally counter-clockwise from the x-axis.

For a termination minutia, the ANSI/NIST direction is found by the angle formed between the x-axis and the vector pointing out of the minutia and splitting the valley between the ending ridges neighbors. The FBI's EFTS standard is exactly 180 degrees out of phase and measures the angle between the x-axis and the vector pointing back from the minutiae and

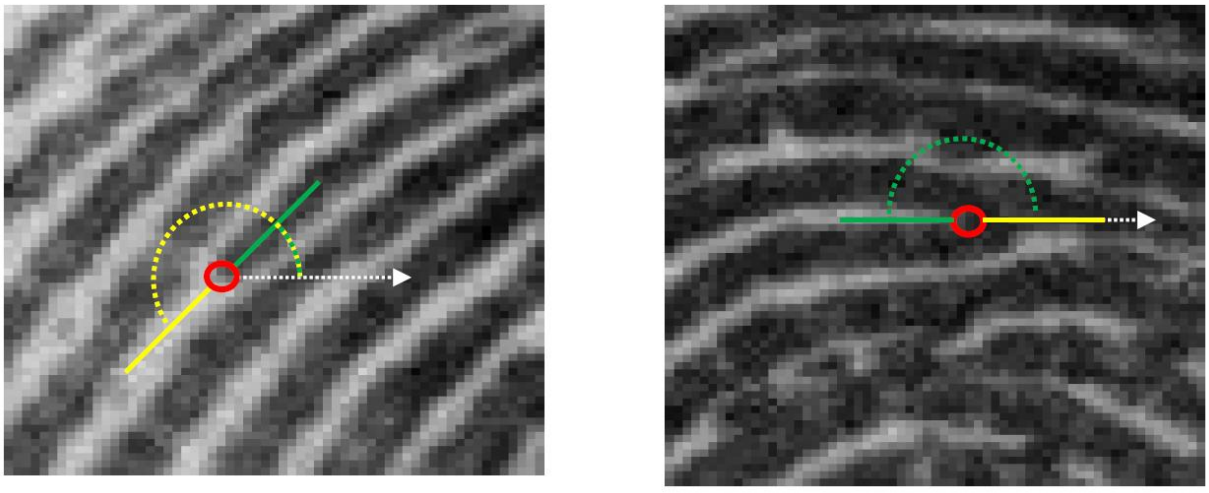

(a) (b)

Figure 2-5: ANSI/NIST (yellow) and FBI's EFTS (green) standard minutia direction for (a) termination and (b) bifurcation.

splitting the ending ridge. In the bifurcation case, the ANSI/NIST direction measures the angle between the x-axis and the vector pointing from the minutia, splitting the joined ridges. The FBI's EFTS standard measures the angle between the x-axis and the vector pointing out of the minutia, splitting the valley between the un-joined ridges.

In addition to standards for minutiae, the Committee to Define an Extended Fingerprint Feature Set (CEFFS) [47] was formed by the Scientific Working Group on Friction Ridge Analysis, Study, and Technology (SWGFAST) [48] to identify, define, and provide guidance on extended features. At the time, the ANSI/NIST ITL-2000 standard only contained definitions for minutiae such as ridge endings and bifurcations, which is only a small portion of the information contained in a fingerprint used by latent examiners during identification. CDEFFS is responsible for the original conception of the Extended Feature Set (EFS) specification which is included in the ANSI/NIST ITL-1 2011 data format interchange standard [3].

Table 2-2 shows the fields in the Type-9 record that are associated with Level 3 features. The table contains definitions and how each of the features is to be marked or represented in the template. The goal of the extended features standards is to promote a common interchange format between human examiners and also between AFISs. Recommended guidelines for

extracting EFSs are detailed in [3]. A workflow diagram is provided so that regions of the image can be classified with how much detail is available for extraction. This ridge quality/confidence map is found in field 9.308 of the Type-9 ANSI/NIST record. There are six levels of ridge quality in field 9.308:

0) Background, no ridge information is present;
1) Debatable ridge flow, continuity of ridge flow is not reliable;
2) Definitive ridge flow/debatable minutiae, not certain of presence, absence, and location of all minutiae;
3) Definitive minutiae/debatable ridge edge, ridge edge contours are not clear or ambiguous;
4) Definitive ridge edge, debatable pores, pores are not clear or ambiguous;
5) All data are clear, all features are visible and can be located precisely.

These levels are used to identify the reliability of the features detected within corresponding regions.

2.4 Summary

In this chapter, we described the essential features that can be found in a fingerprint. These features range from singularity points derivable from ridge flow patterns of the fingerprint that can be used for classification to discriminating minutiae that are used for identification. In addition, we see the level 3 features that are found within high resolution fingerprint images and can be used in conjunction with minutiae for increasing decision confidence or in the case of partial prints, allowing for a decision to be made. For all feature level data, standards exist for proper labeling to facilitate interoperability among commercial automated extraction methods and human examiners. In the case of minutiae, multiple standards exist for representation and the differences between these standards have been described.

The NIST Biometric Image Software (NBIS) [49] was developed for the FBI and Department of Homeland Security (DHS) and is freely available from NIST. The NBIS software offers a learning-based tool for classifying level 1 details of fingerprints, automated detection and encoding of fingerprint features, and a minutia-based matching algorithm to compute match

scores between fingerprints. While no known system is publicly available for extracting and matching level 3 details, standards have been developed to promote a consensus among human examiners and also in anticipation of future automation of level 3 feature extraction. In Chapter 3, we propose an algorithm focused minutiae and ridge extraction in low quality fingerprint regions. In Chapter 4, we propose a method for extracting ridge structure information as well as provide a method for obtaining relational information among minutiae. This additional information is used to strengthen match confidence in partial fingerprint images, where a low number of reliable minutiae are present.

Table 2-2: Extended features included in ANSI/NIST Type-9 [3] records.

	Field	Definition	Marking	Quality Needed
Dots	9.340	A single ridge unit shorter than the local ridge width.	Single point located at the center of the short ridge.	3
Incipient ridges	9.341	A ridge substantially thinner than the local ridge width. It is marked.	Line segment along the longest dimension. Series of thin dots should be marked as separate incipients.	3
Creases and Linear Discontinuities	9.342	Creases include permanent flexion creases (Distal Interphalangeal Crease). Minor non-permanent creases, cracks, cuts, and thin scars are marked as linear discontinuities.	Line segment along its length. Curved features should be marked as a series of line segments.	3
Ridge Edge Features	9.343	A sudden increase in ridge width that does not form a long enough ridge to be considered a bifurcation.	Center of the protruding area.	4
Pores	9.345	Openings in the outer skin along a ridge where sweat is released.	Center of pore.	5

Chapter 3

Feature Extraction

3.1 Introduction

Fingerprints continue to be one of the most common sources of information for human identification and verification. Friction ridges and their associated minutiae are detected and used for image-to-image comparison. Because of the importance of fingerprint-based recognition, automated systems have become readily available to perform on-line fingerprint matching. Automated systems depend heavily on features derived from minutiae, which are discontinuities of the friction ridges, and rely heavily on the availability of images that are of good quality. The two most widely used minutia types are ridge endings and bifurcations.

For some applications, including forensic analysis, it is not always possible to obtain high-quality image samples. As a consequence, image features may be difficult to extract with sufficient quantity and accuracy to support a decision. As an illustration, a typical rolled fingerprint is shown in Figure 3-1 (a). Because of the relatively high quality of the image, upwards of 100-120 minutiae can be extracted and used for matching. A much smaller number of reliable minutiae can be obtained from the prints shown in parts (b-d) of the figure. Images that are obtained in unfavorable conditions, such as dry or wet environments [4], or as latent prints from crime scenes, will often exhibit poor ridge and valley clarity, which leads to unreliable features for matching.

In addition, the Department of Homeland Security's (DHS) US-VISIT program processes about 130,000 fingerprints a day from international visitors entering the United States [50].

These prints are used to link biographic information so that an identity can be established. The goal of the US-VIST program is threefold: 1) checking a watch list for suspected terrorists, 2) determine if an alias is being used as fraudulent identification, and 3) ensuring the documents provided during the encounter belong to the person presenting them. While quality measures are employed to ensure a good sample is acquired, it is not always possible to obtain optimal prints with such a high throughput.

In Afghanistan, a push is being made to collect biometric data from all passengers traveling through the country, regardless of their residency. The Afghan Automated Biometric Identification System (AABIS), supported by the FBI, is working to enroll 8 million of its citizens as a national identification program. Originally, the program was started to catch criminals and Taliban insurgents from infiltrating the military and police forces. However, it has also led to the identification of many unsolved FBI cases involving latent prints captured from IED fragments [51]. Many of the prints are captured during battlefield encounters, leading to more issues with quality due to environmental irregularities. It is important to collect accurate representations of the fingerprints, regardless of their quality, as these are used in some cases for counter-terrorism measures.

(a) **(b)** **(c)** **(d)**

Figure 3-1: Example fingerprint images. (a) A good quality fingerprint; (b) a dry fingerprint; (c) a wet fingerprint; and (d) a latent fingerprint. Images (a-c) are from [4] and (d) is from NIST SD27 [8].

3.2 Previous Work

Most of the current state of the art extraction methods are based on the pioneering work of Jain, Hong, and Bolle [52] and Maio and Maltoni [53], both from the late 90's. The former is more intuitive and leads to accurate matching for good quality fingerprints, whereas the latter is more complex and more robust to noise. The following outlines both of these methods.

In [52], fingerprint features are extracted from a binary representation of the fingerprint image. The binary image is found by either applying a threshold to the grayscale image directly or by detecting peaks in oriented cross sections of the grayscale image, where the orientation is taken orthogonal to the direction of the local ridge flow. From the binary image representation, the medial axis transformed image is found. This transform also is known as the skeleton of the binary image, which is a one pixel width representation of the original binary image [54]. This operation consists of iteratively thinning a binary image until no pixels have changed, maintaining the structural integrity of the binary image. Morphological thinning is the process of removing foreground boundary pixels that are connected by more than one neighboring foreground pixel, as long as the removal does not locally disconnect the foreground [54]. A boundary pixel is one that is connected to at least one background pixel.

Once the skeleton image is found, the minutiae are detected by looking for end points and branch points. These features are found by looking at the number of foreground neighbors of each pixel. An endpoint will have only one neighboring foreground pixel. A point along the ridge will have two neighboring foreground pixels and a branch point will have three neighboring foreground pixels. The accuracy of this approach relies heavily on the performance of the image enhancement routine used before binarization. The most common method of enhancement is to apply a set of oriented Gabor filters to make the ridges and valleys more prominent. There have been a number of adaptations and alternatives to this method; most of the literature deals with the binarization step and filter design for the fingerprint enhancement [4].

An alternative method proposed by Maio and Maltoni [53] traces along friction ridges in order to locate minutiae. The algorithm assumes that ridges are represented as a set of local gray level maxima in image I, where higher intensity values represent darker shades of gray. For a given point in I, the ridge direction is assumed to be perpendicular to the intensity gradient. For

efficiency of implementation, a directional flow map based on intensity gradients is computed in advance. The algorithm makes a sequence of steps along each ridge of interest, using the directional flow map and a user defined step size of several pixels. At each step, the center of the ridge is approximated by searching for a local maximum in the direction orthogonal to the current ridge.

The algorithm continues along the ridge line until a stop criterion is met. The authors define four criteria, three of which are used here. Using slightly different names than [52], the criteria are 1) termination, where no point above a given intensity threshold is found at the next step in the ridge direction; 2) bifurcation, where the next point lies on a previously traced ridge line; and 3) outside region of interest, where the next search region is external to a predefined region of interest for the entire image.

An extension to the previous work was introduced by Liu et al. [55]. As a ridge is traced, the two valleys that lie on either side of the ridge are tracked simultaneously. Because of the dual relationship between ridges and valleys, a ridge ending corresponds to a bifurcation of the valleys surrounding it. As each new ridge point is found, candidate left and right valley points are identified as local minima in the directions perpendicular to the ridge flow. The left (and right) valley is extended to the minima closest to the ridge point on either side of the ridge. A new stop criterion replaces the termination stop criterion described above: 1*) when both valleys extend to the same candidate valley point, indicating a valley bifurcation, then a ridge ending has been detected. Experimental results obtained using the method of [55] have shown improvement over that of [53], including less sensitivity to noise.

Another variant to this method was proposed by Jiang et al. [56], where the step size is adapted to the local ridge flow coherence. With a high coherence in ridge flow, the step size is large, and a low coherence produces a smaller step size. More recently, Arpit and Namboodiri [57] proposed the use of a narrow band-pass filter with adaptable parameters to trace ridges more robustly in noisy regions. This tracing method is claimed to be more robust to noise than the previous methods.

Both of the methods described above rely heavily on ridge direction information. In the binary-image approach, the Gabor filter enhancement performance is directly related to the

accuracy of the ridge flow approximation. In the grayscale tracing approach, the next ridge point in the sequence is found by use of the local ridge flow information. When the ridge flow direction map is unreliable, both of these methods can produce ridges that are unreliable, thus lowering the match performance when using the extracted features. Ma et al. [58] proposed a method for predicting ridge flow direction; however, no significant quantitative results were reported showing an improvement.

3.3 Proposed Approach

This section outlines a novel approach to fingerprint analysis from segmentation to minutia detection. A connected component analysis technique is proposed for maximizing the solidity of a foreground mask, reducing the background noise included in the fingerprint region. In addition, a ridge line tracing method is introduced for minutia detection that tracks the ridge peaks using a particle filtering approach. First, we describe how the foreground and background regions of the fingerprint image are segmented. Then, we describe how the problem of ridge tracing is modeled as a particle filtering problem to improve tracing in noisy and low ridge clarity regions. Background on recursive Bayesian estimation and particle filtering is given in Appendix A.

3.3.1 Segmentation

Mehtre et al. [59] proposed one of the first methods for fingerprint segmentation by looking for significant peaks in a local histogram of ridge flows. A sharp peak in the histogram indicates a large number of pixels in the region having similar direction. On the other hand, a flat histogram indicates a large variation in directions, which is common in a background region. Ratha et al. [60] proposed a method that considered intensity variances in local 16×16 pixel regions oriented orthogonal to the ridge flow direction.

Before computing the gradient image, the fingerprint image I is normalized using min-max normalization so that the intensity values have a range of [0, 1]:

$$\hat{I} = \frac{I - \min(I)}{\max(I) - \min(I)} \tag{3.1}$$

Horizontal and vertical gradient maps are found by determining the rate of pixel intensity change in the *x*- and *y*- directions of the normalized image. The first derivative of the normalized image can be approximated by convolving with a Sobel filter [54]:

$$G_x = \hat{I} * S_x \tag{3.2}$$

$$G_y = \hat{I} * S_y \tag{3.3}$$

where

$$S_x = \begin{bmatrix} +1 & 0 & -1 \\ +2 & 0 & -2 \\ +1 & 0 & -1 \end{bmatrix} \tag{3.4}$$

$$S_y = \begin{bmatrix} +1 & +2 & +1 \\ 0 & 0 & 0 \\ -1 & -2 & -1 \end{bmatrix} \tag{3.5}$$

Using the derivative approximations, the magnitude and direction of the gradient can be computed for each point in the normalized image. To handle noise in the image, these computations are taken over a local average $n \times n$ sized block, *B*. The magnitude is computed first to determine if the block is part of the foreground or background

$$\vec{\nabla}\hat{I} = \frac{1}{n^2} \sum_{i,j \in B} \sqrt{G_{x_{i,j}}^2 + G_{y_{i,j}}^2} \tag{3.6}$$

$$I_m = \begin{cases} 1 & if\ \vec{\nabla}\hat{I} \geq t \\ 0 & otherwise \end{cases}. \tag{3.7}$$

Here, I_M is a binary mask image where foreground pixels are set to "on" (1) and background pixels are set to "off" (0). This determination is made by comparing the gradient magnitude of each block, $\vec{\nabla}\hat{I}$, to a set minimum threshold, *t*. The values $(G_{x_{i,j}}, G_{y_{i,j}})$ are the gradient values at the row and column location $(i,\ j)$ within the block in the horizontal and vertical directions, respectively. To remove small amounts of noise and to produce a smooth foreground mask, connected component analysis is used to remove small blocks and to fill in holes of the larger connected foreground blocks.

Since the gradient direction indicates the change in intensity, it follows that the ridge flow direction is found as the direction orthogonal to the gradient. The ridge flow direction, θ, is found using the gradient maps from Eqn. 3.2 and Eqn. 3.3 by:

$$\theta = \frac{1}{2} atan2\left(2G_{xy}, G_{xx} - G_{yy}\right) + \frac{\pi}{2} \tag{3.8}$$

Here, G_{xy}, G_{xx} and G_{yy} are the local block average maps for the element wise products $\left(G_x \times G_y\right), G_x^2$, and G_y^2, respectively. The result of the *atan2* operation produces the doubled angle, which is then halved and the angle orthogonal to the ridge flow direction is found by adding $\frac{\pi}{2}$ radians. An example of an input fingerprint image with its gradient direction indicated in red and ridge flow direction indicated in green is shown in Figure 3-2. The figure shows a 3-D representation of a fingerprint image with intensity values specifying height; large changes in z direction indicate high gradient magnitude.

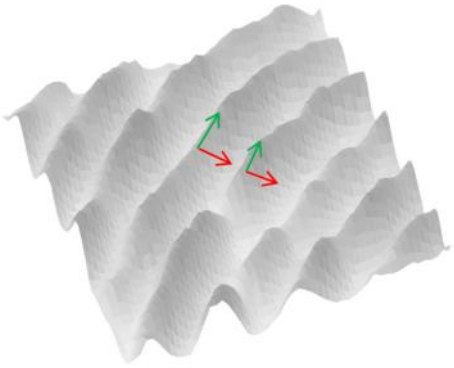

Figure 3-2: Fingerprint region showing ridge structure represented as a 3-D image. Here, the *z*-axis is the gray level of the neighborhood. The red line shows the gradient direction and the green line shows the ridge flow direction, which is orthogonal to the gradient direction.

A local quality map is generated by measuring the reliability of the directional map in the foreground of the fingerprint image. The level of direction uniformity within a block indicates the quality of the fingerprint within a given region. To compute the quality map, *Q*, the local coherence is found using the method described by Jain et al. [52]:

$$Q_B = coherence(\theta_B) = \frac{\left|\sum_{i,j \in B} \theta_{i,j}\right|}{\sum_{i,j \in B}\left|\theta_{i,j}\right|}. \qquad (3.9)$$

In Eqn. 3.9, higher coherence implies high uniformity and higher fingerprint region quality. Figure 3-3 shows an example input fingerprint image along with the pre-processing results of foreground segmentation, ridge flow direction computation, and region quality estimation. In (a), the original image is shown, while in (b), the segmented foreground region is shown with the background blacked out. In (c), the directional map is overlaid on top of the segmented fingerprint image. Finally in (d), the quality map is shown with green blocks indicating high quality and red blocks indicating low quality.

A global quality score for the entire fingerprint region can be found to help predict the potential quality of feature extraction. The global quality score, I_Q, is determined by

$$I_Q = \left(\frac{1}{N_B}\right)\sum_{B=1}^{N_B} Q_B, \tag{3.10}$$

where N_B is the total number of foreground blocks in the fingerprint image.

In the case of fingerprints with noisy backgrounds, or accidental impressions on an enrollment card, it is common for segmentation to result in a poorly defined foreground region. This leads to a large number of spurious minutiae being falsely detected in regions that are, in actuality, part of the background. Here we propose a segmentation method that uses connected component analysis and the region properties associated with the components. We want to maximize the convex hull representing the largest component in the segmented image while also maintaining a high S*olidity*. Solidity is a measure of the number of foreground pixels that are contained within the convex hull defining the region. A low solidity indicates that the convex hull outlining the foreground region contains large holes, or background elements. High solidity indicates that the convex hull is a good fit to the foreground region. A formal definition of solidity is:

$$Solidity = \frac{Component_{area}}{ConvexHull_{area}}. \tag{3.11}$$

Here, the areas are measured in number of pixels for both the component and the convex hull.

Using Eqn. 3.7 produces a binary image with foreground pixels labeled as 1s and background pixels as 0s. Connected component analysis is applied to the binary image to find the foreground regions in the image. The largest connected component is assumed to be the complete fingerprint region. Background noise, lines, and text resulting in high gradient magnitudes can be falsely detected as foreground regions in the segmented image. When these regions overlap with the true fingerprint surface, they are included in the connected component of the fingerprint. To avoid detecting spurious minutiae in these regions, we propose a method for removing these regions prior to feature extraction.

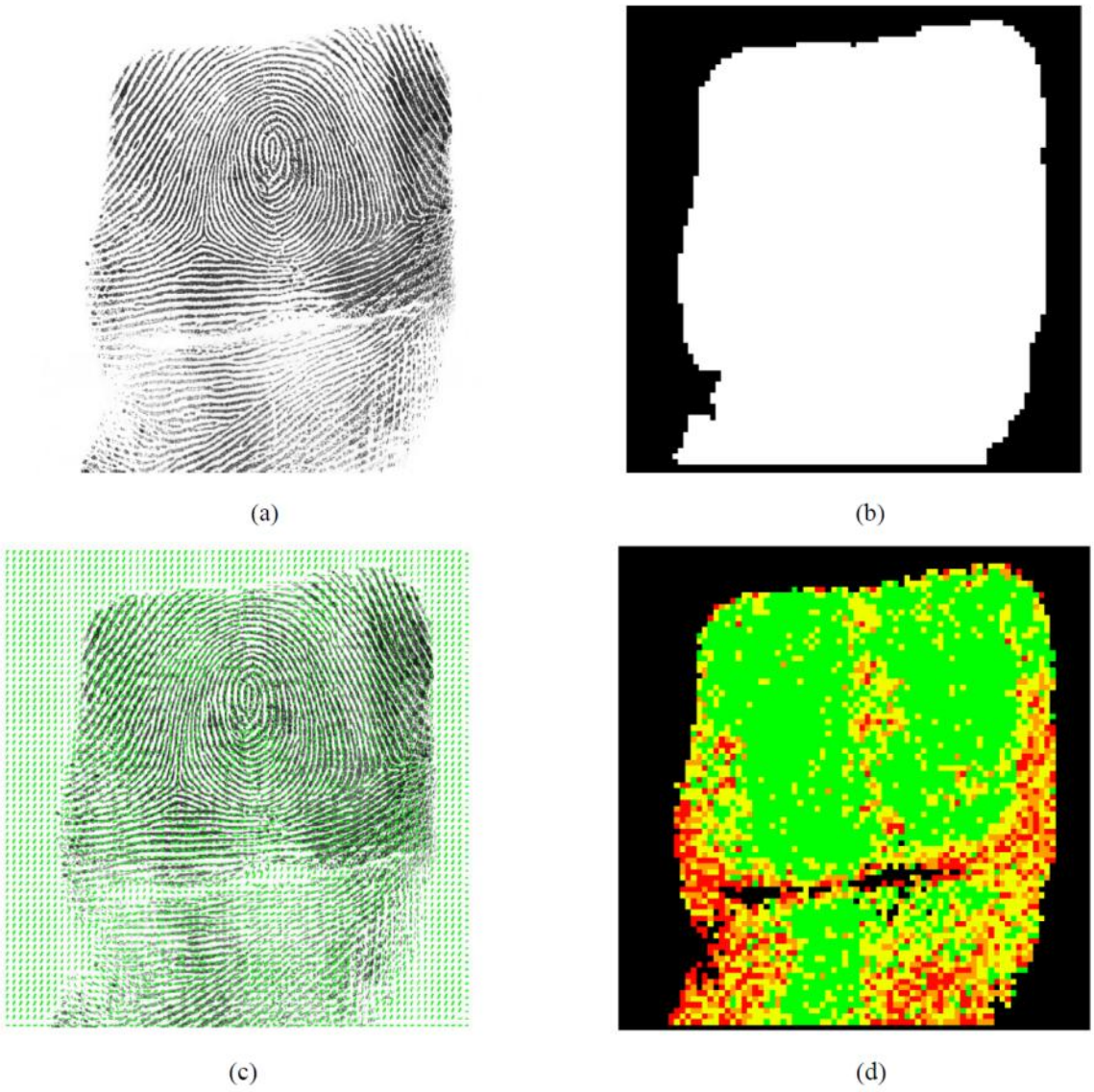

Figure 3-3: Example of (a) original fingerprint image, (b) fingerprint region mask, (c) directional flow map, and (d) quality map.

If the solidity of the component is less than a set threshold, we proceed to shrink the convex hull by moving the outlier hull points closer to the weighted centroid of the component. The weighted centroid is found as the center of mass of the component, using the gradient magnitude map as weights. By using the weighted centroid, we can reduce the effects of large regions of low quality on the position of the center of mass. The distances between the convex hull points and the weighted centroid are calculated; those points lying outside of a certain

percentile of the entire set of distances are pulled in closer to the centroid. The marked points are moved towards the centroid along a straight line. The distance moved along the line is equal to the distance required for the point to lie within the set percentile distance. The convex hull is now defined by the new set of points; all pixels lying outside of the new convex hull are set to 0. A new solidity value is calculated and this process is repeated until the solidity value is over a required threshold.

In Figure 3-4 (a-f), an example is shown for the segmentation process of a fingerprint image with a noisy background. Much of the background shows up in the foreground mask, leading to spurious minutiae being detected in those regions during feature extraction. In (a), the traditional fingerprint mask, calculated using Eqn. 3.7, is shown for the example image in (g). The image in (b) shows a red dashed line indicating the convex hull containing the original mask. The solidity threshold in this example is set to 0.9. In other words, 90% of the convex hull should be filled with the foreground region.

The convex hull for the original mask is only filled by 65% of foreground pixels. In (b), the green dashed line indicates a convex hull where all points are within the 60^{th} percentile of distances from the weighted centroid. All of the pixels outside of the region defined by the green convex hull are marked as background pixels. The solidity after the first iteration is increased to 78%. This process is repeated in steps (c) – (e) where the solidity rises to 84%, 88%, then finally above 90%. In (f), the final foreground region mask is shown, defined by the resulting convex hull. Figure 3-4 (h) shows the fingerprint region segmented from the background using the foreground mask from (f).

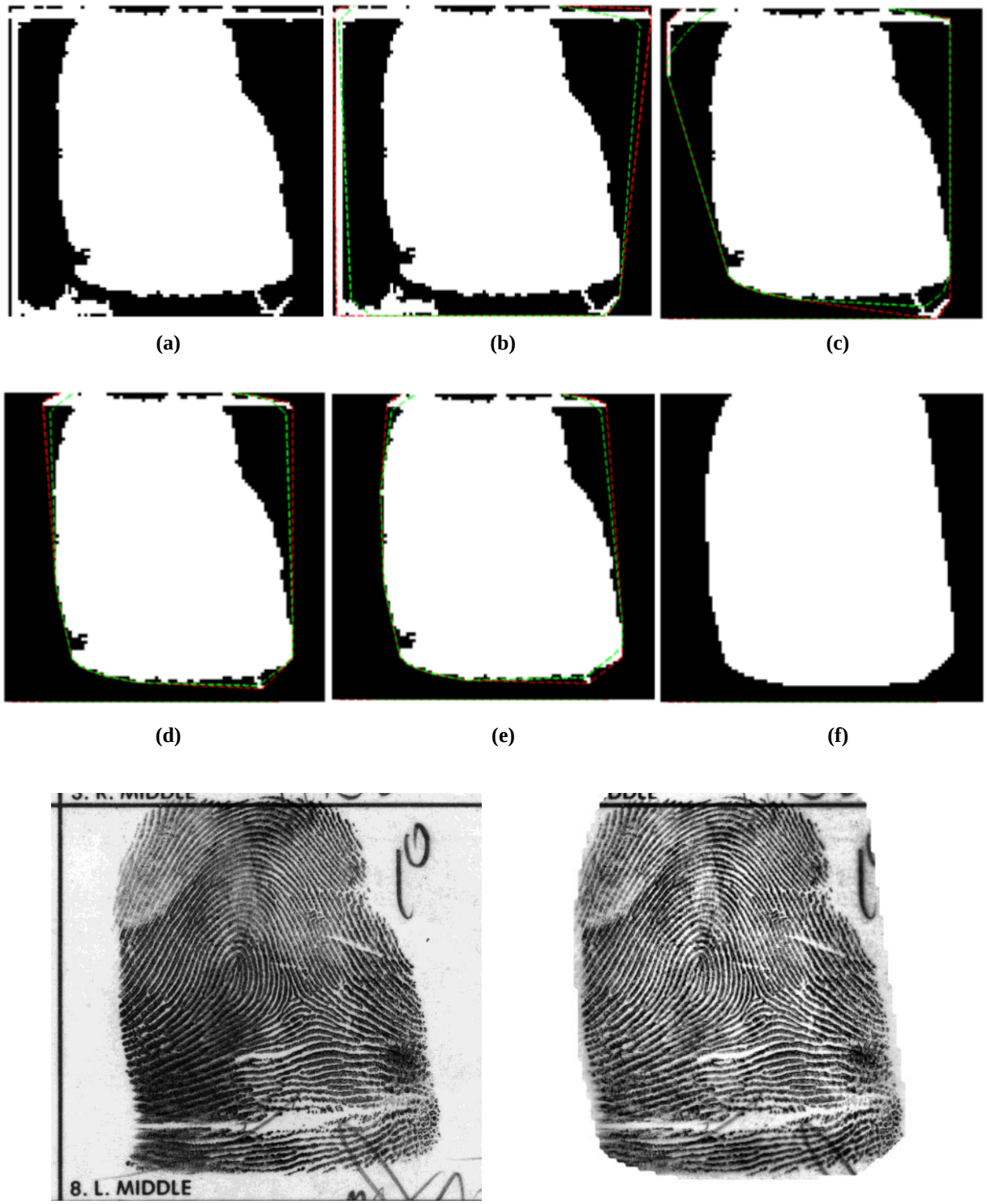

Figure 3-4: Example of proposed segmentation routine. (a-f) show a convex hull adapting to the fingerprint region in the image. (g) and (h) show the original and segmented fingerprint images, respectively.

3.3.2 Enhancement

Once the foreground is segmented, an enhancement routine is applied to accentuate the ridges and valleys of the fingerprint region. To do this, the image is convolved with a Gabor filter, which is a linear filter commonly used for edge detection. The filter was designed by Dennis Gabor to mimic the human visual system and is represented in the spatial domain by a 2-D Gaussian kernel modulated with a plane sinusoid wave [61],

$$G = e^{\left\{-\frac{1}{2}\left[\frac{\hat{x}^2}{\sigma_x^2}+\frac{\hat{y}^2}{\sigma_y^2}\right]\right\}} \times \cos(2\pi f \hat{x}) \tag{3.12}$$

where

$$\begin{bmatrix}\hat{x}\\ \hat{y}\end{bmatrix} = \begin{bmatrix}\cos(\theta_B) & \sin(\theta_B)\\ -\sin(\theta_B) & \cos(\theta_B)\end{bmatrix}\begin{bmatrix}x_B\\ y_B\end{bmatrix}. \tag{3.13}$$

Here, f is the frequency of the sine wave, (x_B, y_B) are the index values of the region of interest around the anchor pixel, θ_B is the direction and σ_X/σ_y are the horizontal/vertical standard deviations (skew) factors of the Gaussian envelope. We set the size of the kernel to the same size of the block, B, and the skew factors, σ_x, σ_y are empirically set to 4. The tradeoff with the selection of σ_x and σ_y is the higher the values, the more robust the Gabor filter is to noise, but the better the chance that false ridges and valleys will be artificially created. With lower values, the lower the effectiveness of reducing noise as well as the lower the chance of creating false ridges and valleys.

In Figure 3-5, an example is shown where an input fingerprint image is enhanced using a Gabor filter generated from Eqn. 3.12. The parameters for the filter are $\mathrm{f} = 0.0909, \sigma_\mathrm{x} = \sigma_\mathrm{y} = 4.0$, and $\theta = \pi$. Here, the value for the frequency is chosen empirically and works well for regions of the fingerprint that have a ridge spacing of 11 pixels; however, the enhancement step can degrade the ridge structure of regions where the frequency deviates.

Due to the elasticity of the skin, distortion in the fingerprint ridges is present towards the outer regions of the print, causing a decrease in the frequency of the ridges. Determining the local ridge frequency a priori can produce a Gabor filter that is capable of improving the quality

of fingerprint regions of varying frequency ranges. A frequency map can be generated by taking intensity profiles oriented orthogonal to the ridge flow direction at an anchor pixel [62]. The ridge frequency is taken as the average pixel distance between peaks in the profile, or x-signature, as shown in Figure 3-6.

(a) (b) (c)

Figure 3-5: Example of fingerprint image enhancement using Gabor filter: (a) a Gabor filter with $f = 0.0909, \sigma_x = \sigma_y = 4.0$, and $\theta = \pi$, (b) original fingerprint image, and (c) enhanced fingerprint image.

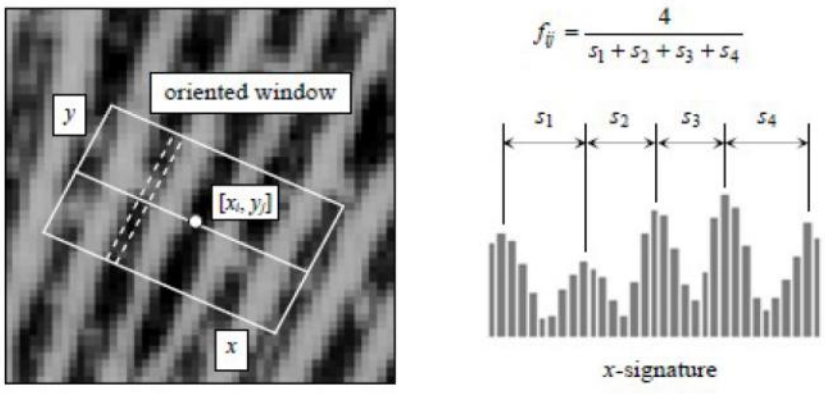

(a) **(b)**

Figure 3-6: Method for finding ridge frequency map of a fingerprint image. (a) Fingerprint image with oriented window. (b) Cross section profile taken from oriented window showing the gray level peaks and resulting ridge frequency. (Images from [4])

3.3.3 Ridge Line Tracking

The method for feature extraction using ridge line tracking outlined in this section assumes prior knowledge of Recursive Bayesian Estimation Theory, namely the Particle Filter. An overview of Particle Filtering, also known as the CONDENSATION algorithm in computer vision, is provided in Appendix A.

Ridge Tracking Model

To model the fingerprint ridge line tracing as a filtering problem, let the system state be the current ridge direction, such that $x_t = \theta_t$. The current ridge point, $\boldsymbol{r}_t$, is given by

$$\boldsymbol{r}_t = u \begin{bmatrix} \cos(\theta_t) \\ \sin(\theta_t) \end{bmatrix} + \boldsymbol{r}_{t-1} \,. \tag{3.14}$$

where $\boldsymbol{r}_{t-1}$ is the previous ridge point, direction θ_t is estimated using the expected value approximation in Eqn. A.2, and u is a predefined step size.

The observation function, $y_t = \gamma_t$, is given by similarity measurements taken from the region of interest around the current filter position; specifically, this is the cross-correlation score of an ideal ridge profile with a sampled intensity cross section that is orthogonal to the current direction [32]. The ideal ridge profile is defined by

$$T_{i,j} = \sin\left(2\pi f d_{i,j} - \frac{\pi}{2}\right) = -\cos\left(2\pi f d_{i,j}\right). \tag{3.15}$$

Here, f is the local ridge frequency and $d_{i,j}$ is the Euclidean distance from pixel (i, j) to the ideal ridge peak. At each time step, we have a set of particles, weights, and inferred points, $\{\theta_t^{(i)}, \omega_t^{(i)}, \boldsymbol{r}_t^{(i)}\}$. The ridge tracking algorithm, including particle sampling and importance weight determination, is described in the next three sections.

Initialization

The tracking process is started by generating a set of initial points from within the fingerprint region of interest. For each potential starting point, a ridge profile is taken orthogonal to the local ridge flow direction and correlated with an ideal ridge template generated using Eqn. 3.15. The location corresponding to the highest cross-correlation score is assumed to be a ridge peak, and is chosen as the starting point for tracking.

After the starting point has been determined, samples and weights for the Bayesian filter are initialized as follows:

$$\theta_0^{(i)} \sim N(D_{ROI}, \sigma^2), \qquad i = 1,2,..K \tag{3.16}$$

$$\omega_0^{(i)} = \frac{1}{K}, \qquad i = 1,2,..K, \tag{3.17}$$

where D_{ROI} is the local ridge flow direction of the region surrounding the starting point and σ^2 is an empirically chosen variance. The weights are initially identical, but will evolve as the ridge is tracked.

Estimation

For each tracking step, the filter is updated by first drawing new samples for θ_t from a normal distribution with mean equal to the direction of the same particle at the previous step:

$$\theta_t^{(i)} \sim N\left(\theta_{t-1}^{(i)}, \sigma^2\right). \tag{3.18}$$

From this set of samples, importance weights are assigned using the following method:

1) Compute the naïve filter location by moving in the direction of $E[\theta_{t-1}]$ by a pre-defined step size.

2) Let A_t be the line passing through the naïve prediction point in the direction $E[\theta_{t-1}] + \frac{\pi}{2}$.

3) Find importance function $g(\cdot)$ by first computing cross-correlation score, s_t, of the ideal ridge template with the ridge profile in the direction of A. The scores are normalized so that the range is $[0, 1]$. Here, we define $g(\cdot)$ as

$$g(s_t) = e^{\lambda(s_t - 1)}, \tag{3.19}$$

where λ is chosen empirically.

4) Let $D_t^{(i)}$ be the line that passes through the previous ridge point in the direction $\theta_t^{(i)}$, and update the importance weight for samples by the following,

$$\omega_t^{(i)} = \omega_{t-1}^{(i)} g\left(s(\tau_t^{(i)})\right), \tag{3.20}$$

where $\tau_t^{(i)}$ is the intersection of the two lines A_t and $D_t^{(i)}$

From Eqns. 3.18 and 3.20, a set of samples and importance weights are found that approximate our state density, $p(\theta_t|\gamma_t)$. The set of samples and associated weights, $\{\theta_t^{(i)}, \omega_t^{(i)}\}$, are used to compute the expected direction, $E[\theta_t]$, as a weighted sum. Using Eqn. 3.14 with the expected direction, the next point in the ridge model tracing is calculated.

Steps 1-4 described for drawing samples and calculating importance weights are represented visually in Figure 3-7. Part (a) of the figure represents the filter at time t. In the top left image, a fingerprint region is shown with a blue point on the ridge being tracked. The current ridge direction is toward the lower left of the image. The blue point represents the

previous ridge point, the red points represent random samples (particles), and the green point represents the current sample. The top right image shows line A_t, perpendicular to the ridge direction, and line $D_t^{(i)}$, which is used to determine the intersecting point $\tau_t^{(i)}$ (marked in green) at step (4). The middle image shows the ridge profile that is extracted along the line A_t with the intersection point highlighted. The bottom graph illustrates the importance weight function determined by Eqn. 3.19. In (b), the posterior distribution, $p(\theta_t \,|\gamma_t)$, is shown as approximated by the particles and associated normalized importance weights.

The previous example could have been reasonably approximated by a normal distribution, because the distribution in Figure 3-7 (b) is unimodal. Figure 3-8, however, illustrates a tracking step near a ridge bifurcation. In such a case the posterior distribution is nonlinear and multimodal. These cases are much better approximated with particle filtering, and are critically important in the extraction of minutiae.

In order to avoid the problem of degeneracy, which is the inevitable increase in variance of particles over time [63], the proposed tracking method invokes a Sampling Importance Resampling (SIR) [64] approach to handle degeneracy of the particles. As the variance increases after a few iterations, all of the samples will have negligible weight except for one. Instead of wasting a significant amount of computation time on updating particles whose impact on approximating the posterior is small, the SIR method suppresses particles with low weights and replaces them with particles of larger weights at each time step. In other words, the particles are resampled using the importance weight density so as to concentrate on particles with significant weights.

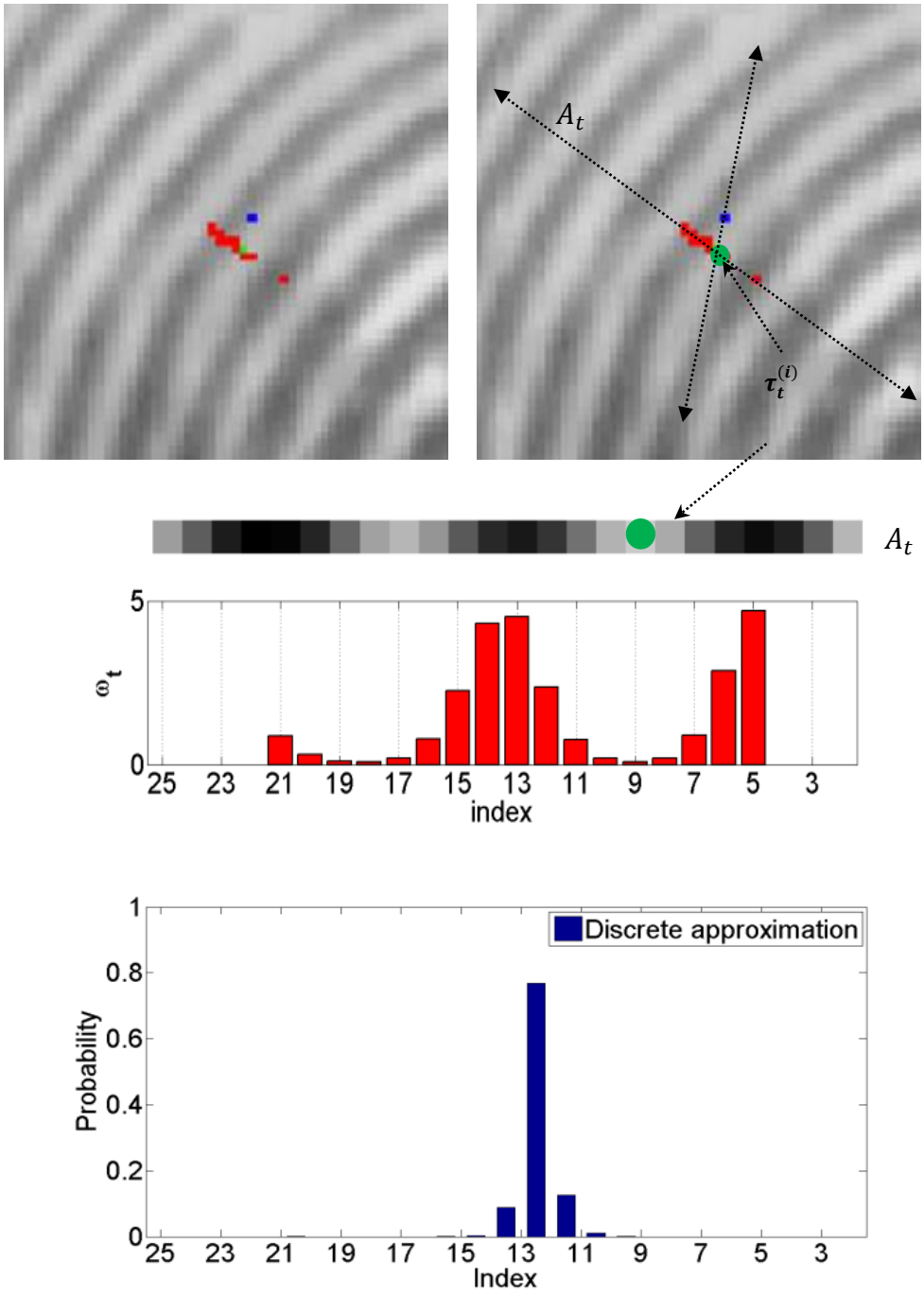

Figure 3-7: Filtering example demonstrating (a) the steps taken at time t of the filtering process and (b) the approximated posterior distribution from the set of samples and importance weights.

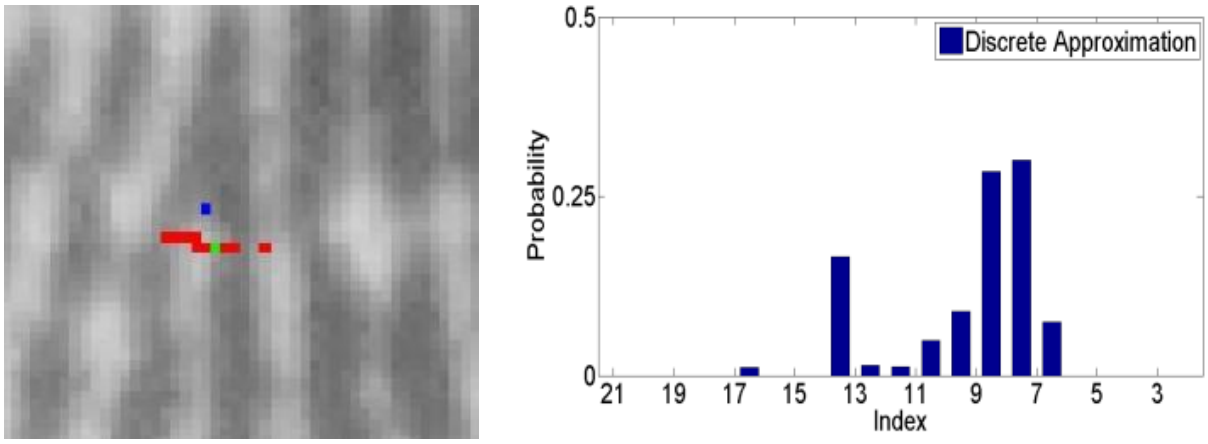

(a) (b)

Figure 3-8: Non-linear filtering example demonstrating (a) the step taken at time t of the filtering process and (b) the approximated posterior distribution from the set of samples and importance weights.

Termination

To prevent the tracking method from continuing to infinity or jumping from ridge to ridge, a set of rules are invoked to terminate the filtering process. The first criterion is when the tracking process produces an updated point that lies outside of the region of interest of the image. This region is pre-computed using a gradient-based segmentation approach [52]. The second is when the updated ridge point encounters a previously tracked ridge, indicating a bifurcation minutia. The third criterion is when the filter location changes direction abruptly, in comparison with the past estimates. This event produces a termination minutia. The same heuristics proposed by [52] and [53] are used for removing spurious minutiae.

3.4 Spurious Minutiae and Localization

3.4.1 *Spurious Minutiae*

Once the minutiae have been extracted, a post-processing routine is applied to remove spurious minutiae caused by noise. Without removing the false minutiae, matching performance will suffer. In the top of Figure 3-9, eight of the most common false minutiae encountered are shown and their resulting ridge structure as proposed by [65]. The method results in the connection of facing endpoints (a) and (b), removes bifurcations with neighboring terminations (c), or with other bifurcations (d); and removes spurs (e), bridges (f), triangles (g), and ladder structures (h). At the bottom of the figure, the restructuring of the ridges in the skeleton image to remove these minutiae is shown. The methods for removing spurious minutiae can be applied to either the binary-based or ridge trace-based method.

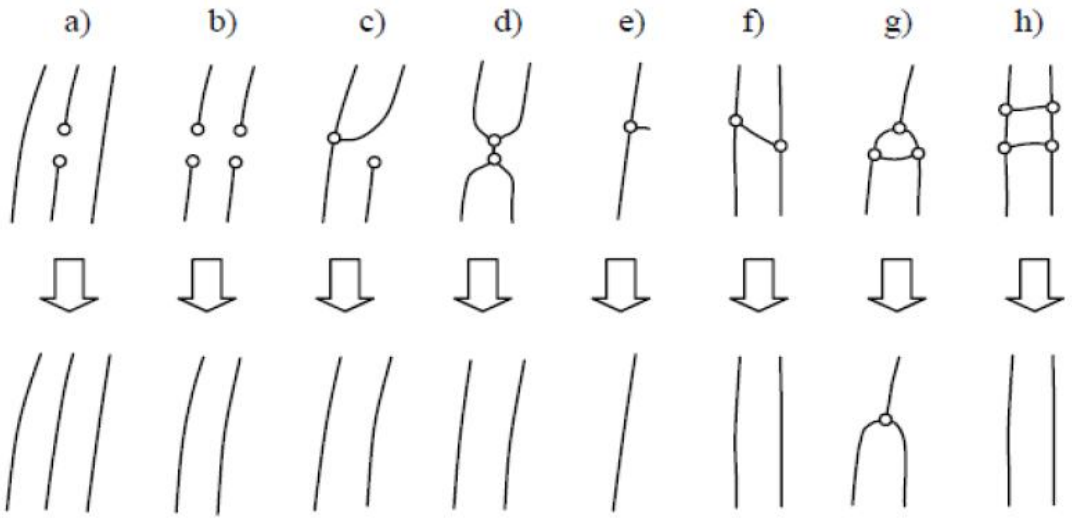

Figure 3-9: Eight common false ridge structures that result in spurious minutiae (top) and the changes to the ridge structure applied to remove them. (Reproduced from [4])

3.4.2 *Minutiae Localization*

When only a small number of features are available for matching, the quality and accuracy of those features become particularly important. Here, we refer to minutia error as the deviation of extracted minutia attributes, such as position in the image, from ground truth. In Figure 3-10 (a), a fingerprint region is shown with ground truth minutiae marked (asterisks) and minutiae locations resulting from introducing error from normal distributions with variances of 1 (filled diamonds), 2 (filled squares), 3 (open circles), 4 (open squares), and 5 (open diamonds). In Figure 3-10 (b), a Cumulative Match Characteristic (CMC) curve is shown to compare matching performance for these different cases. Images and ground-truth data are from National Institute of Standards and Technology's (NIST) Special Database 27 [8].

An identification rate of *r* in the CMC plots for rank-*n* indicates that the correct match was among the top n matches for r of all attempts. The plots show the effects of location noise on the CMC performance metric when a limited number of features are available. In this case, even with a variance of 1 on a small dataset of 258 fingerprints, the rank-10 identification rate has decreased by 3.5%. As the number of fingerprints in the database increases, it can be expected

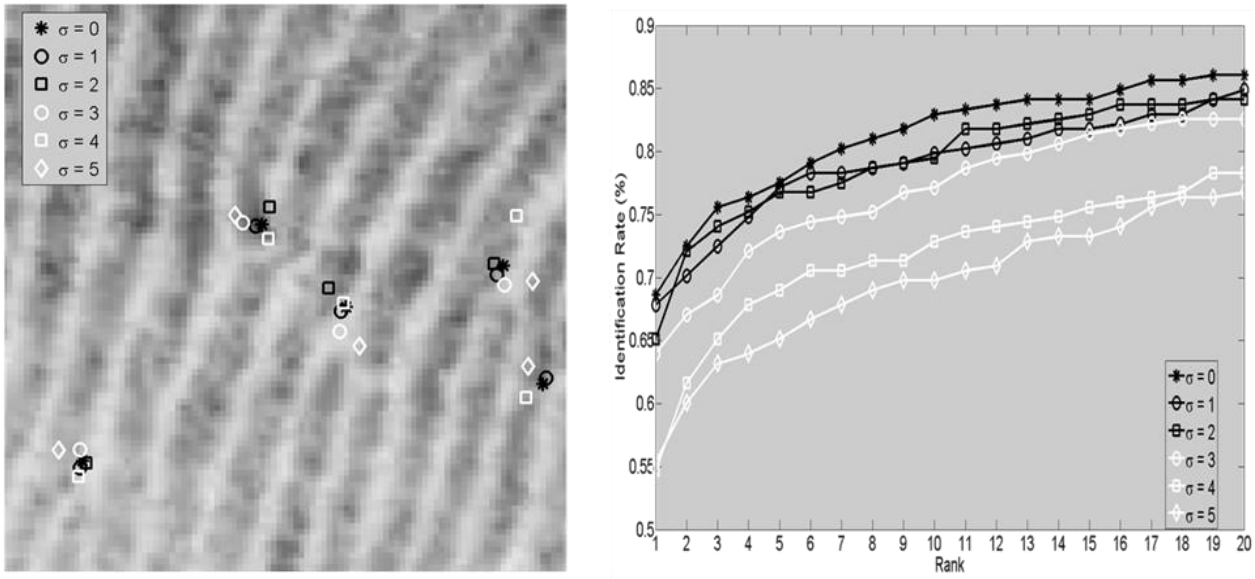

(a) **(b)**

Figure 3-10: Examples of (a) fingerprint minutiae location error with $\sigma = 0, 1, 2, 3, 4, \text{and } 5$ and (b) the resulting CMC curves. As might be expected, minutiae that are more accurately located result in better identification performance.

that variability will have an even greater effect on match performance.

In addition to removing spurious minutiae, we also refine the location and direction descriptors of the true minutiae by using a Bayesian filtering approach. To model the refinement as a particle filtering problem, we let the state of the system at each step be the pixel row and column in the image, (r_t, c_t), together with the angular direction of the minutia, so that $x_t = [r_t, c_t, \theta_t]$. The observational measurement is defined as the normalized cross correlation score of a region of interest around a given point, $(r_t^{(i)}, c_t^{(i)})$, and oriented to a given direction, $\theta_t^{(i)}$. Three-dimensional representations of the templates used to find potential terminations and bifurcations are shown in Figure 5. To refine the location and direction, we seek to approximate the posterior iteratively,

$$p(r_t, c_t, \theta_t|\alpha_t) \propto p(\alpha_t|r_t, c_t, \theta_t)p(r_t, c_t, \theta_t|\alpha_{t-1}) \qquad (3.21)$$

from which to find the expected location and direction of an initial minutia:

$$E[r_t, c_t, \theta_t|\alpha_t] = \iiint \theta_t c_t r_t p\,(r_t, c_t, \theta_t|\alpha_t) dr_t dc_t d\theta_t \qquad (3.22)$$

The posterior distribution in Eqn. 3.21 is approximated for each time step, t. We use the system dynamics transition prior, $p(r_t, c_t, \theta_t|r_{t-1}, c_{t-1}, \theta_{t-1})$, as the proposal distribution. To approximate the posterior state distribution through filtering, we need to generate a set of properly weighted samples, $\{r_t, c_t, \theta_t|r_{t-1}, c_{t-1}, \theta_{t-1}\}$, from the system dynamics transition prior. The observation is found by the normalized cross correlation measurement of an ideal minutia template oriented by $\theta_t^{(i)}$ at a point $(r_t^{(i)}, c_t^{(i)})$ in the region of interest. The steps for sampling and weighting are described below.

Initialization

Particles are initialized by drawing K samples from distributions centered on the initial minutia location, (r_0, c_0), and direction, θ_0, found by the minutia detection routine.

$$c_0^{(i)} \sim U(-s_c, +s_c), \qquad i = 1,2,..K \tag{3.23}$$

$$r_0^{(i)} \sim U(r_0 - s_r, r_0 + s_r), \qquad i = 1,2,..K \tag{3.24}$$

$$\theta_0^{(i)} = U(\theta - s_\theta, \theta + s_\theta), \qquad i = 1,2,..K \tag{3.25}$$

Here, s_r, s_c, and s_θ are used to define the range from which to draw values for the respective distributions. The weights, $\omega_0^{(i)}$, are initialized to $\frac{1}{\mathrm{K}}$ for all $\mathrm{i} = 1,..\mathrm{K}$.

Sampling

Using the assumption that θ_t and (r_t, c_t) are independent, we separately generate samples from $p\left(r_t^{(i)}, c_t^{(i)} \middle| r_{t-1}^{(i)}, c_t^{(i)}\right)$ and $p(\theta_t^{(i)} | \theta_{t-1}^{(i)})$ by

$$\begin{bmatrix} r_t^{(i)} \\ c_t^{(i)} \end{bmatrix} \sim N\left(\begin{bmatrix} r_{t-1}^{(i)} \\ c_{t-1}^{(i)} \end{bmatrix}, \Sigma\right) \tag{3.26}$$

and

$$\theta_t^{(i)} \sim N\left(\theta_{t-1}^{(i)}, \sigma^2\right), \tag{3.27}$$

where Σ and σ^2 are empirically covariance matrix and variance values, respectively.

Weighting

The likelihood function from Eqn. 3.21 is given by $p\left(\alpha_t \middle| r_t^{(i)}, c_t^{(i)}, \theta_t^{(i)}\right)$ in the minutia refinement problem and approximated by the importance weight function, g(·). We choose the importance weight function as

$$g(s_t) = e^{\lambda(s_t - 1)}, \tag{3.28}$$

where s_t is the cross correlation score of the ideal minutia template oriented at $\theta_t^{(i)}$ and centered at $(r_t^{(i)}, c_t^{(i)})$ within the region of interest. The importance weights are updated and normalized at each time step. Using Eqn. 3.22, we can compute the expected values for r_t, c_t, and θ_t. The sampling and weighting steps are repeated until the variance is below an empirically defined threshold.

A quality score is determined, as in [32], by the "goodness of fit" of the localized minutia neighborhood and the ideal template used in refinement. The template is oriented and positioned using the final state approximation from the filtering process. The minutia type also can be found by performing the filtering process using both the termination and bifurcation ideal template and selecting the model that produced the best goodness of fit score.

3.5 Experimental Results

3.5.1 Segmentation

To test the performance of the proposed segmentation method, a database of 59,693 rolled fingerprint images was used (Appendix C). The samples are a collection of digital fingerprints scanned from fingerprint cards or from live-scan systems. The minutia-based Neurotechnology VeriFinger 4.2 SDK [66] was used to detect minutiae in the foreground regions defined using the traditional approach to fingerprint segmentation. The same method was used to detect minutiae from the same set of rolled prints, but using the proposed segmentation method.

The statistics that were used to assess performance were the average number of minutiae detected in the set and the average quality of the set. The hypothesis is that the proposed method will reduce the number of unreliable minutiae, leading to lower minutiae counts and higher reliability scores. The results for this test are reported in Figure 3-11 and show the number of

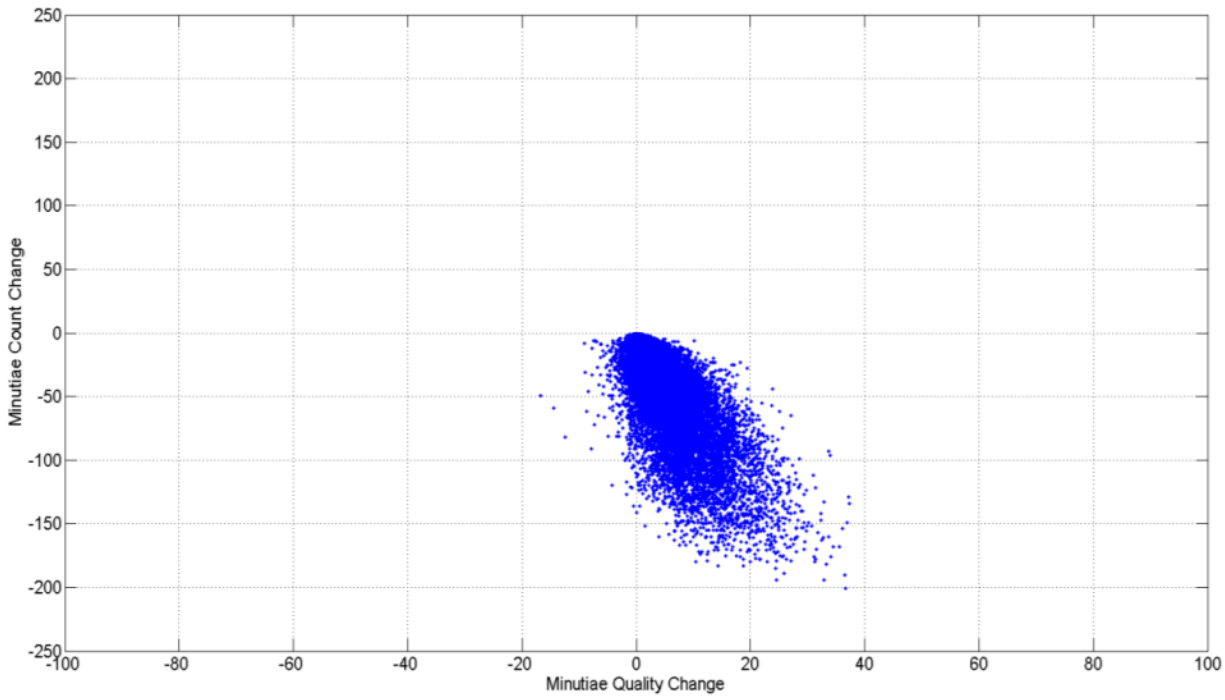

Figure 3-11: Scatter plot indicating minutiae set quality vs. count for 59,693 rolled digital fingerprints. The plot shows the change in minutiae count and average quality between the traditional segmentation approach and the proposed approach. A positive quality indicates an improvement in minutiae set reliability and a decrease in minutiae count indicates a reduction of the minutiae set size.

minutiae detected in a print vs. the average quality of the minutiae. The red samples are from the traditional segmentation approach and the blue samples are from the proposed approach. From the data, we can conclude that unreliable minutiae were removed as spurious minutiae, due to the fact that the average number of minutiae was reduced while also increasing the average reliability of the set. In this experiment, we were able to decrease the number of detected minutiae by an average of 15, resulting in an increase to the average minutiae set reliability.

3.5.2 Ridge Line Tracking

The fingerprint images used in our experiments are from Fingerprint Verification Competition 2000 Database 1, consisting of 8 impressions of 110 fingers for a total of 880 fingerprint images. The images are 300 × 300 pixels in size, and were scanned at 500 dpi. To compare the performance of the proposed method with the binary and direct grayscale methods outlined in Section 2, we independently extracted minutia features from the fingerprint images using all 3 algorithms. This section will refer to the previous methods as Binary and Tracing, and to the proposed method as Tracking. The minutia-based NBIS [49] and Neurotechnology VeriFinger 4.2 SDK [66] were used separately to compute an exhaustive set of match scores for the minutiae that were obtained by each of the 3 extraction methods.

In addition to overall comparison, the performance was compared by quality breakdown, where the fingerprint images were separated into three quality groups using the Biometric Identity Management Agency's (BIMA) Fingerprint Image Quality Measurement (FIQM) toolset [6]. We partitioned the fingerprint images into groups labeled "Good" for quality scores between 80 and 100, "Bad" for scores between 60 and 80, and "Ugly" for scores lower than 60. The purpose of this test is to demonstrate the ability of the proposed method to extract reliable minutiae that lead to higher matching performance for not only the whole set of fingerprints, but for poor quality prints in particular. Example images from the FVC 2000 DB1 representing each of the classes are shown in Figure 3-12.

In Figures 3-13 through 3-16, results are reported for both (a) NBIS and (b) VeriFinger matchers. In Figure 3-13, the normalized score distributions for imposter and genuine matches are shown, to illustrate how well the two classes are separated. Because high match scores

correspond to high fingerprint similarity, it follows that the genuine and imposter distributions should have large peaks near the upper and lower ends of the horizontal axis, respectively. Figure 3-14 shows the False Accept Rate (FAR) and False Reject Rate (FRR) as functions of classification threshold. As the threshold for determining match vs. non-match moves from 0 to 1, the FAR decreases and the FRR increases. Plots in Figure 3-13 and 3-14 are for the proposed ridge tracking method only.

Figure 3-15 presents log-scale Receiver Operator Characteristic (ROC) curves indicating performance of the proposed ridge tracking method in comparison to the Binary and Tracing feature extraction routines. The 1% FAR, 0.1% FAR, and Equal Error Rate (EER) lines are shown indicating the respective performance levels. The values are listed in Table 3-1 below for all three algorithms and two matchers. From the table, we see that the proposed Track method has extracted minutiae that lead to matching performance that is better than both two traditional methods. The EER has been reduced by 2.1% over the Binary method and by 2.5% over the previous grayscale Trace method.

Finally, Figure 3-16 shows log-scale ROC curves for all three methods and for all three quality groups. The EER, 1.0% FAR, and 0.1% FRR values are listed in Table 3-2 below for each of the extraction methods and matchers. Our proposed Track method performs better in all

(a) (b) (c)

Figure 3-12: Example fingerprints from FVC 2000 DB1. As determined by [6], the quality is (a) Good, (b) Bad, and (c) Ugly .

cases. Significantly, when using the VeriFinger matcher, our proposed method using shows a reduction in EER of 5.5% and 7.4% over the previous binary and grayscale trace methods, respectively, for the worst quality case.

Table 3-1: Performance measurements at EER, 1.0% FAR, and 0.1% FAR for all feature extraction methods using (a) NBIS and (b) VeriFinger matchers.

(a)

Method	EER (%)	FRR (%) @ 1.0% FAR	FRR (%) @ 0.1% FAR
Track	8.9	19.7	32.6
Binary	10.9	27.9	41.9
Trace	12.9	28.5	51.5

(b)

Method	EER (%)	FRR (%) @ 1.0% FAR	FRR (%) @ 0.1% FAR
Track	7.3	10.9	11.9
Binary	9.4	15.4	16.1
Trace	9.8	14.2	14.9

Table 3-2: **Performance measurements at EER, 1.0% FAR, and 0.1% FAR for all feature extraction methods on subsets grouped by image quality. Scores are computed using (a) NBIS and (b) VeriFinger matchers.**

(a)

Quality	Method	EER (%)	FRR (%) @ 1.0% FAR	FRR (%) @ 0.1% FAR
Good	Track	8.1	16.7	27.3
	Binary	10.5	21.5	34.7
	Trace	12.5	26.2	37.7
Bad	Track	9.6	24.9	41.5
	Binary	11.1	39.0	63.7
	Trace	11.7	31.5	50.2
Ugly	Track	16.0	41.3	55.7
	Binary	17.2	48.3	66.7
	Trace	20.2	50.3	61.4

(b)

Quality	Method	EER (%)	FRR (%) @ 1.0% FAR	FRR (%) @ 0.1% FAR
Good	Track	4.9	6.0	6.3
	Binary	6.3	8.4	8.9
	Trace	6.1	7.8	8.1
Bad	Track	9.6	17.8	20.4
	Binary	12.2	24.4	26.4
	Trace	13.3	21.9	24.2
Ugly	Track	14.4	27.2	28.4
	Binary	19.9	38.3	41.1
	Trace	21.8	38.3	41.1

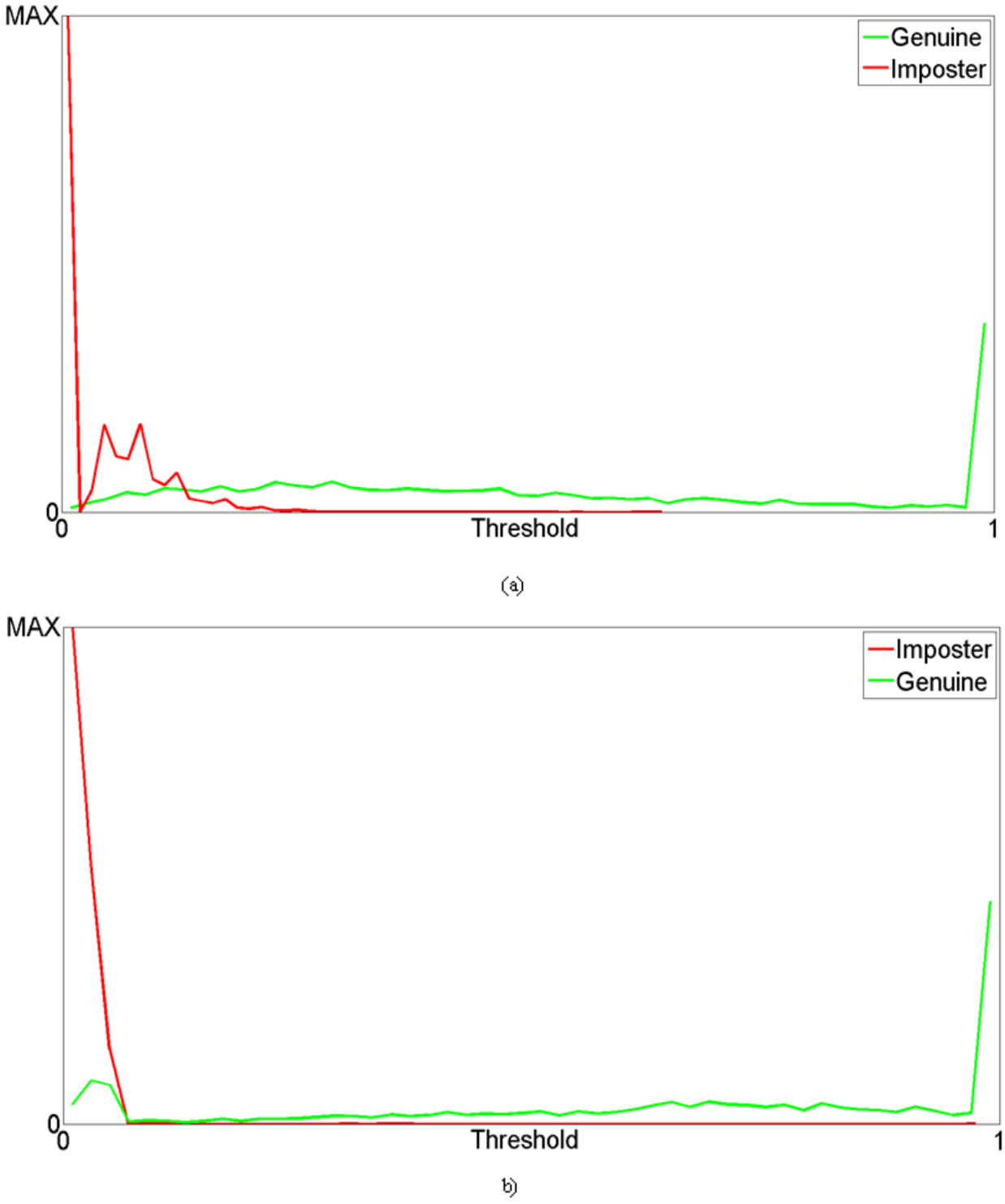

Figure 3-13: Performance plots of genuine and imposter normalized score distributions for (a) NBIS and (b) VeriFinger fingerprint matchers.

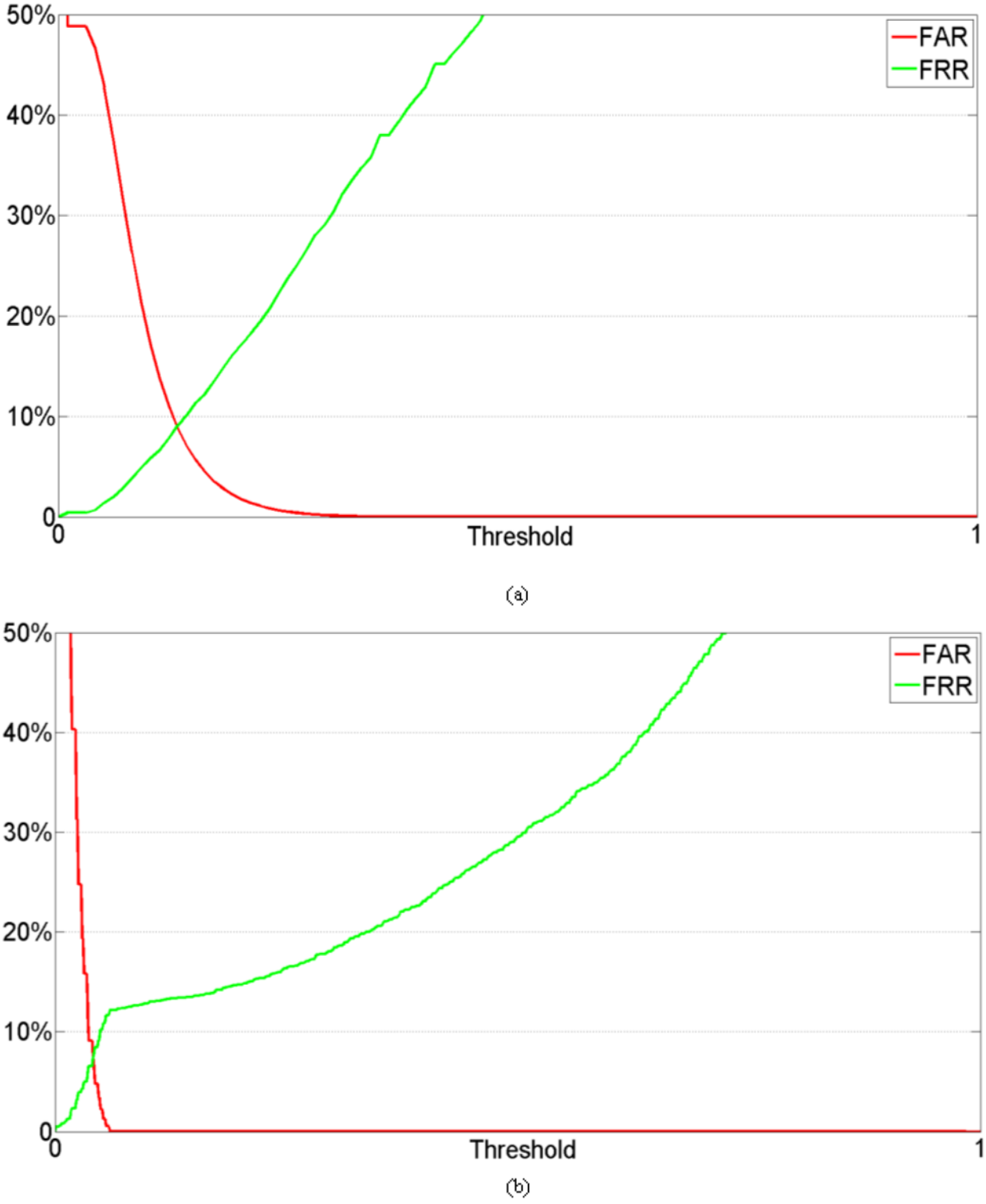

Figure 3-14: Performance plots of FAR and FRR scores for (a) NBIS and (b) VeriFinger matchers.

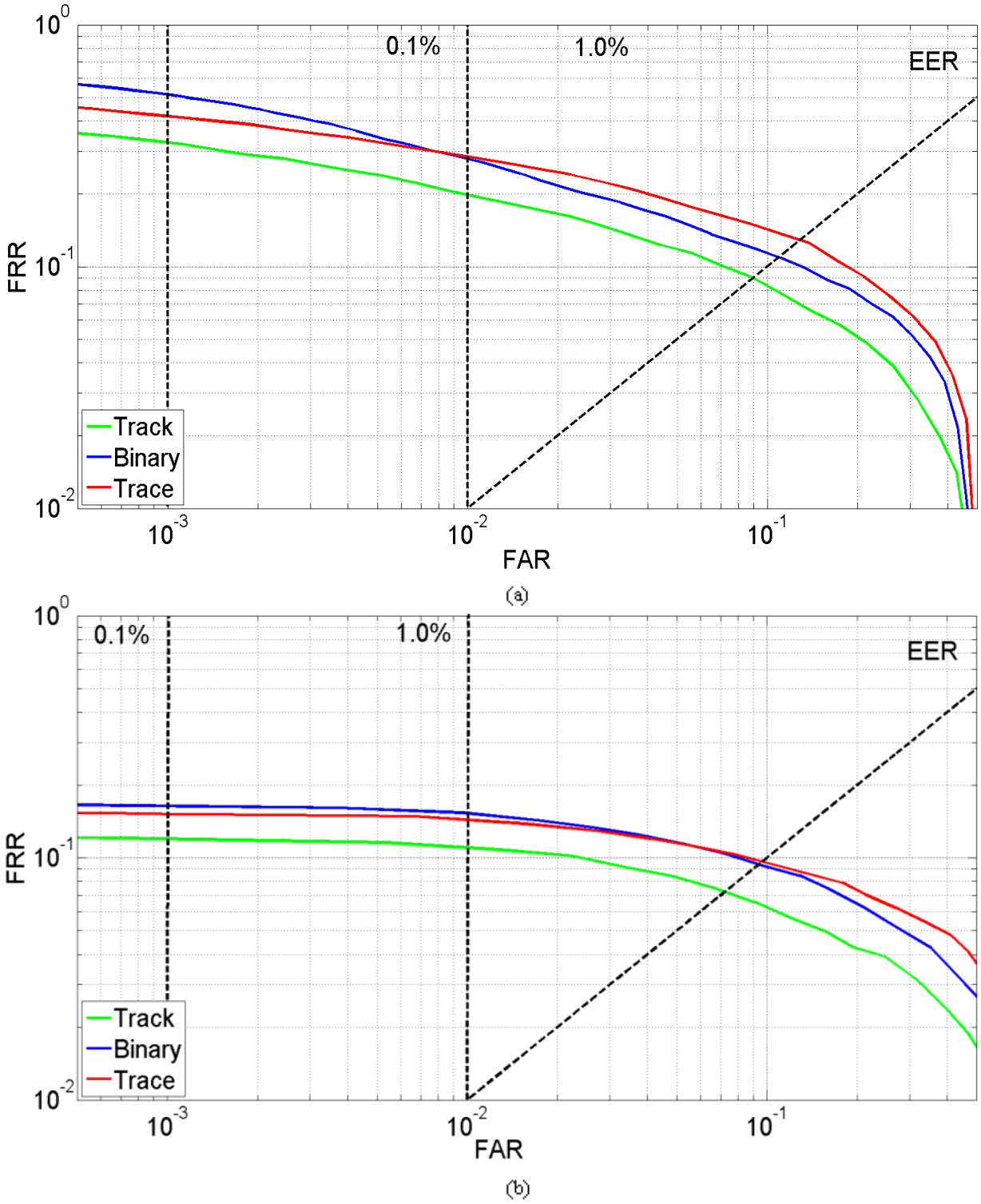

Figure 3-15: Performance plots of FAR and FRR scores for (a) NBIS and (b) VeriFinger matchers.

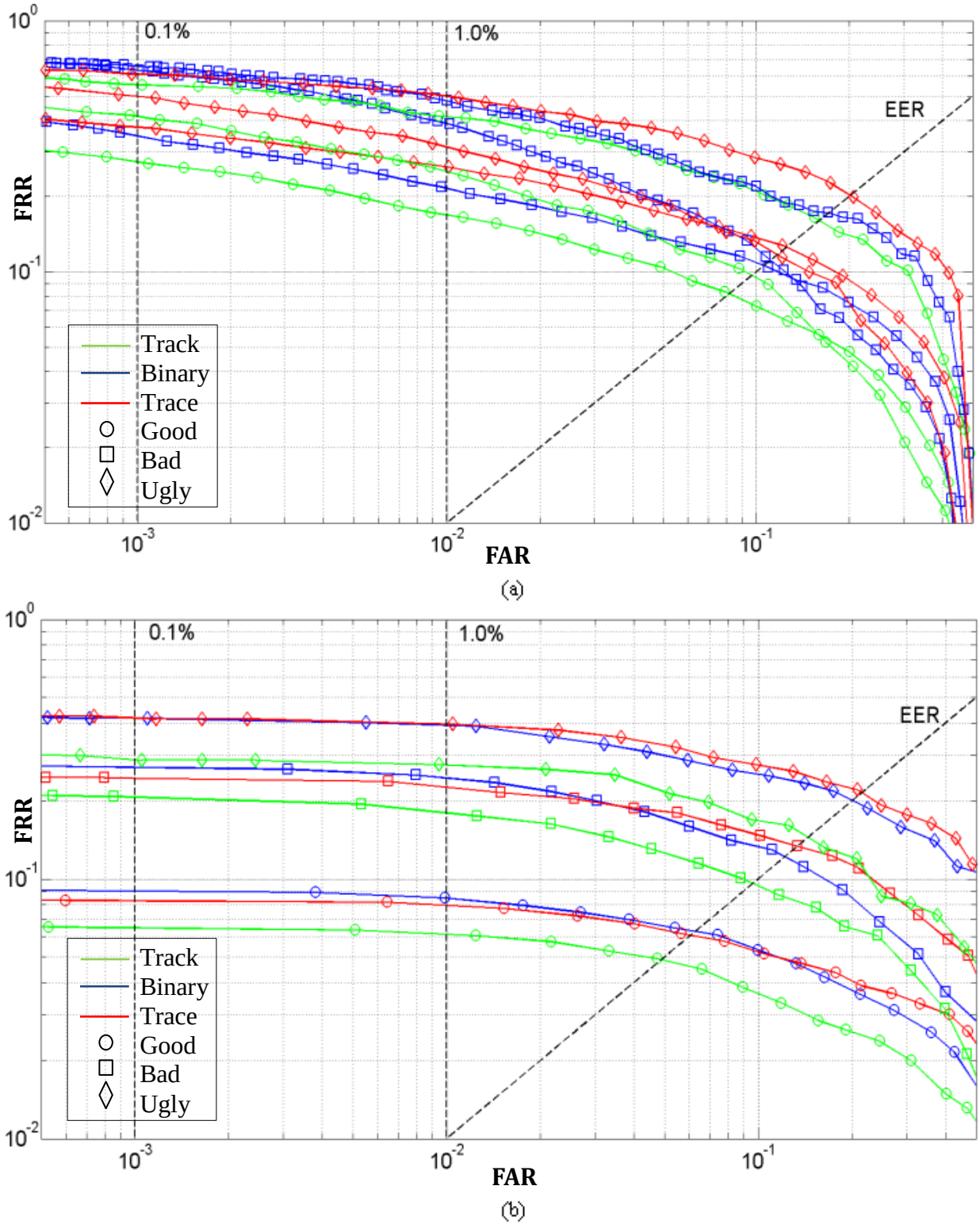

Figure 3-16: Performance plots of FAR and FRR scores for (a) NBIS and (b) VeriFinger matchers. Scores are shown as separate quality groups defined by the quality of the input fingerprint image.

Statistical Significance

Here we show statistical significance tests indicating the probability of observing the given result, or one more extreme. In this case, the result refers to the match scores obtained from the Tracking, Binary, and Tracking feature extraction routines outlined in the previous sections. Small *p*-values cast doubt on the validity of the null hypothesis. In this test, the null and alternative hypotheses are:

H_0: There is no significant difference in match scores.

H_α: There is a significant difference in match scores.

In Table 3-3, p-values for the match score distributions created by the VeriFinger matcher are reported using the Wilcoxon signed rank test [67]. The p-values are shown individually for the imposter (left) and genuine (right) score distributions. The significance test is indicated for confidence levels of 95%, 99%, and 99.9% and a vale of '1' indicates that the null hypothesis can be rejected at the respective level.

Table 3-3: **Statistical significance tests indicating the probability of observing the improved match score data. The significance tests are reported for the imposter (left) and genuine (right) match scores from the VeriFinger matcher.**

	P-Value	95%	99%	99.9%
Track vs. Binary	0	1	1	1
Track vs. Trace	4.39e-131	1	1	1

	P-Value	95%	99%	99.9%
Track vs. Binary	2.35e-016	1	1	1
Track vs. Trace	4.75e-008	1	1	1

3.5.3 Minutia Localization

The proposed method was tested using the NBIS 3.2 MINDTCT minutia detection algorithm to find initial minutia points. In order to demonstrate the importance of improved minutia localization, we performed image-to-image fingerprint matching using the original MINDTCT minutiae as well as minutiae that have been refined using our proposed method. The NIST SD27 dataset was used to demonstrate the improvement in minutia location from the proposed method, due to the available ground truth minutia sets. The database provides a set of 258 plain fingerprint images and 258 latent fingerprint images with minutia sets determined manually by latent print examiners.

To demonstrate improved quality assessment, we have created three groups based on the mean minutia quality: Good quality minutia sets ($50 \leq \overline{Q_m} \leq 100$), Bad ($25 \leq \overline{Q_m} < 50$), and Ugly ($\overline{Q_m} < 25$). The minutia points from NBIS MINDTCT are sorted using the quality score from NBIS and then separately using the proposed quality score. An improvement in quality assessment would be indicated by higher matching scores in the good quality group and lower matching scores in the ugly quality group.

Localization Results

Tables 3-3 and 3-4 show results of localization accuracy with the ground truth data provided by NIST SD27. The distance of each minutia point from the NBIS and proposed method to the corresponding ground truth minutia (determined by the closest minutia point) was calculated for all of the latent and plain prints in SD27. The Mean distance to ground truth is the average distance between the extracted minutiae to the ground truth for all minutiae in the fingerprint database. The % improvement measures the improvement in minutia location, determined by the distance to the true minutia. Finally, the % hit measures the ratio of extracted minutia points which were exact location matches with the ground truth to the total number of minutia in the ground truth set. In this test, any minutia point with a distance less than two pixels from the corresponding ground truth was labeled as an exact match.

Table shows, on average, an improvement in accuracy of 4.67% for the plain print set and 6.44% for the latent print set when the proposed localization is performed. From the same table, we can see an improvement in exact matches from 8.92% to 15.5% for plain prints and 4.99% to

7.07% for latent prints when using the proposed method. From the plain database, 87.9% of the minutia sets improved in accuracy from the proposed localization method. The greatest individual improvement in accuracy of a minutia set (from a single fingerprint) was 14.1%. From the latent database, 88.4% of the minutia sets have shown an improvement in accuracy from the proposed localization method. The greatest individual improvement in accuracy of a minutia set (from a single fingerprint) was 24.29%.

Table 3-5 presents the same results for latent prints, but grouped by the pre-determined quality of fingerprint. These results show improvements in all categories when using the proposed method, with the largest improvement in the Ugly quality group. The improvement for the group of Ugly prints was 8.2% with an improvement for % hit from 4.65% to 7.9% after applying the proposed localization method. Since the quality groups were determined by the latent images, the results for the plain print set are not shown for the individual quality levels.

Example output from selected time steps during the proposed filtering of a minutia are shown in Figure 3-17 and Figure 3-18. In the first row, the initialization step, $t = 0$, is shown with the discrete approximation function, defined by the particles and importance weights,

Table 3-4: **Quality assessment accuracy using NIST SD27 latent prints with ground truth.**

Print Type	Method	Average Error (pixels)	% Improvement	% Hit
Plain	*NBIS*	4.28	4.67	8.92
	Proposed	4.08		15.5
Latent	*NBIS*	4.66	6.44	4.99
	Proposed	4.36		7.07

Table 3-5: **Quality breakdown of localization accuracy using NIST SD27 latent prints with ground truth.**

Print Type	Method	Average Error (pixels)	% Improvement	% Hit
Good	*NBIS*	4.48	4.70	6.81
	Proposed	4.27		9.44
Bad	*NBIS*	4.75	5.80	3.62
	Proposed	4.47		6.13
Ugly	*NBIS*	4.75	8.21	4.65
	Proposed	4.36		7.90

approximating the minutia direction and location, (a) and (b) respectively. Each bin having weight represents a sample, $[r_t^{(i)}, c_t^{(i)}, \theta_t^{(i)}]$. Because all samples have an equal weight in the initialization stage and samples are drawn uniformly, these two plots should be relatively uniform. In (c), the initial minutia location is shown in white and the expected minutia location is shown in black. Finally, in (d) the expected orientation of the minutia direction is indicated by the rotated ideal template. The second row shows $t = 1$, the third row shows $t = 2$, and finally the last row shows the converged state $t = 10$. In this experiment, the refined minutia state is displaced by $[\Delta r = -7, \Delta c = -1, \Delta\theta = 16^{\circ}]$, from an initial state inside the region of interest $[r_0 = 11, c_0 = 11, \theta_0 = 271^{\circ}]$ to the converged state $[r_{10} = 4, c_{10} = 10, \theta_{10} = 287]$.

To show improvement in location interoperability, we simulate the variance of different detection routines by generating a set of minutiae distributed around an initial minutia. The proposed refinement method is applied to the set of noisy data, and a standard minutia is found based on the grayscale information available in the local region. From each of 100 initial minutiae, found using NIST Biometric Identification Software (NBIS) feature extractor MINDTCT, we simulated 10 additional "error" points by adding Gaussian noise with $\sigma = 5$ and centered on the initial minutia. A total of 1000 data points were created from minutiae of fingerprints in the Fingerprint Verification Challenge (FVC) 2000 DB1. The results of adding the noise is similar to the output shown in Figure 3-10. After applying our refinement technique to the simulated noisy data, we were able to reduce the (r, c) location error from $\sigma_c^2 = 1.845$, $\sigma_r^2 = 1.984$ to $\sigma_c'^2 = 0.324$, $\sigma_r'^2 = 0.485$ or a reduction in error of 82.4% and 83.7%, respectively.

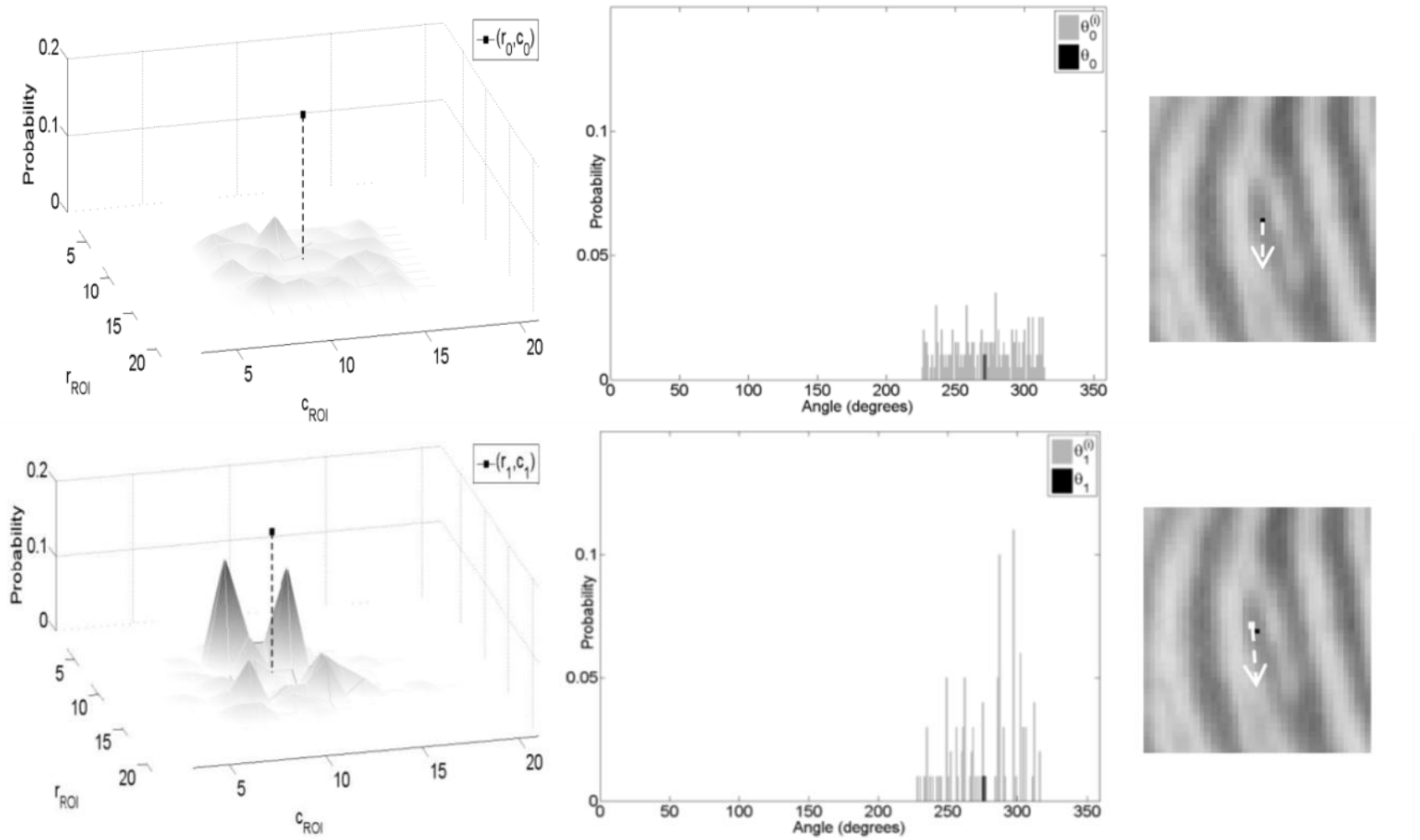

(a) (b) (c)

Figure 3-17: Proposed filtering method example showing time steps t = 0 (top) and 1 (bottom). For each of the iterations, (a) shows the distribution approximated by $\{r_t^{(i)}, c_t^{(i)}, \omega_t^{(i)}\}$ with the expected location indicated by the black square and dashed line, (b) shows the distribution approximated by $\{\theta_t^{(i)}, \widehat{\omega}_t^{(i)}\}$ with the expected direction indicated by a solid black bar for reference. In (c), the expected location is indicated by the white pixel and the initial minutia location is indicated by the black pixel. The white arrow indicates the expected direction of the minutia using the ANSI/NIST standard.

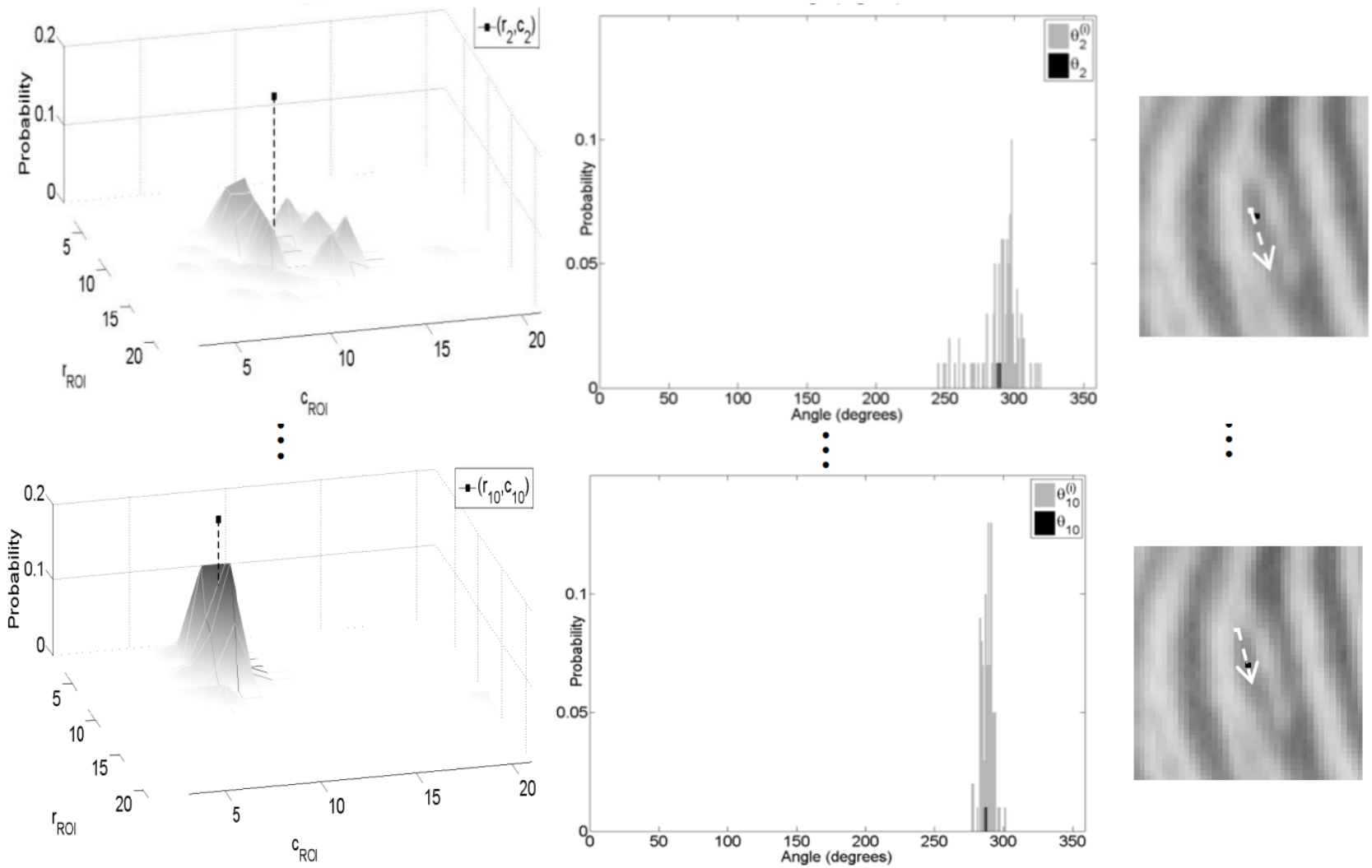

Figure 3-18: Continuation of proposed filtering method from Figure 3-17 for time steps $t = 2$ (top) and 10 (bottom). (a) Distribution representing expected minutia location. (b) Distribution representing expected minutia direction. (c) Expected minutiae location and direction (white) and initial position (black).

Statistical Significance

To guarantee that the improvements obtained from the localization method are not just due to random chance, significance tests have been conducted on the data. The manually extracted minutiae provided with the NIST SD 27 are used as ground truth, and the non-parametric Wilcoxon signed-ranks test [67] is applied to the location errors from NBIS and the proposed localized minutiae to select of these hypotheses:

$$H_0: \textit{There is no significant difference in location.}$$

$$H_\alpha: \textit{There is a significant difference in location.}$$

We use 95% and 99% confidence intervals, where the results are considered significant if the probability of occurrence is less than 0.05 and 0.01, respectively. In Figure 3-19, the cumulative density function (CDF) of the data is shown in (a) and the probability density function (PDF) in (b) with the 95% and 99% confidence intervals indicated by the dotted and dashed lines, respectively. The *z*-score shown indicates a value of -6.19 with a sample size of 2668 and critical *z*-values of -1.96 and -2.56 for the 95% and 99% confidence intervals, respectively. In this test, we reject the null hypothesis in favor of the alternative, concluding that the observed results are statistically significant. The *p*-value for the paired NBIS and proposed minutiae is $3.0\ X\ 10^{-10}$ or a $\frac{1}{333{,}333{,}333}$ chance of observing data at least as extreme.

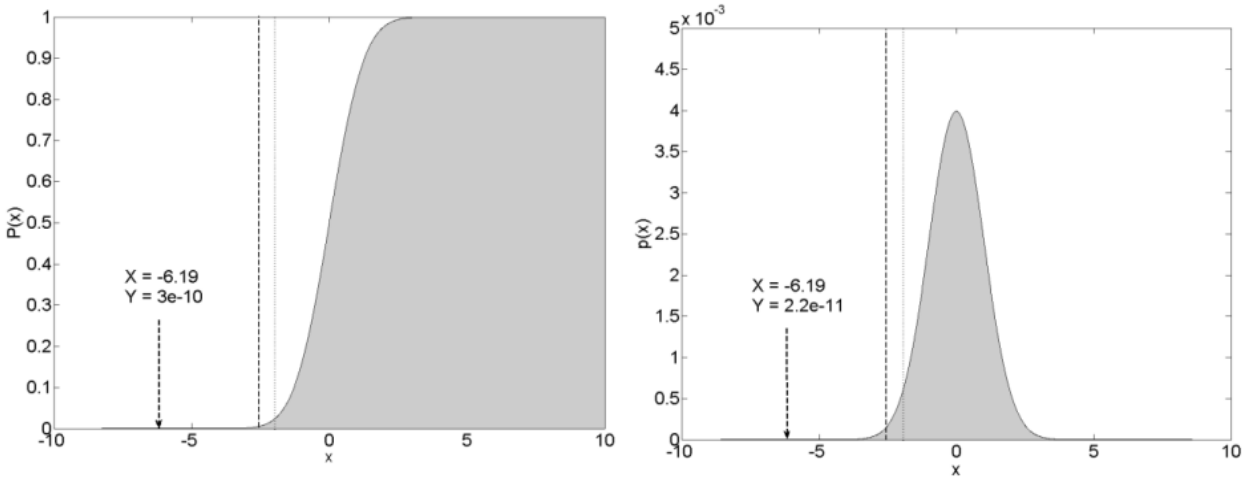

(a) (b)

Figure 3-19: (a) CDF and (b) PDF of standard normal distribution for Wilcoxon Signed-Ranks test. The dashed arrow marks the test statistic for the minutia pairs of all fingerprints. The dotted and dashed lines represent the 95% and 99% confidence intervals, respectively.

Quality Assessment Results

Quality assessment results are shown in Figure 3-20 and summarized in Table 3-6. The measurements from Table 3-6 come from the same test as Table 3-4 and Table 3-5. Here, the quality measures of minutia points that were found to correspond with ground truth minutia are shown for the NBIS quality measure and our proposed quality measure. The NBIS feature extractor finds many spurious minutiae and the belief is that higher quality measures should be found for those minutiae which have corresponding ground truth minutia. The results are shown for the three pre-determined quality groups and for the entire set. For the set of latent prints in SD27, the proposed method improved the average minutia quality for all 258 latent images by 14.62%. The group showing the most improvement was the Ugly group, with a 17.15% increase over the NBIS quality measure. From the plain fingerprint database, 98.8% of the prints have shown an improvement in quality assessment from the proposed method for minutiae that were successfully matched with the ground truth set, the largest individual improvement in quality assessment being 8.12%. From the latent database, 98.4% of the images have shown an improvement in quality assessment from the proposed method for minutiae that were

successfully matched with the ground truth set, the largest individual improvement in quality assessment being 8.12%.

Figure 3-20 (a) shows an example output indicating the NBIS (red) and localized minutiae (blue). In (b), a ROC curve is shown indicating improvement in quality assessment from the proposed method. In this experiment, the NBIS minutia set was used to generate matching scores for both test sets. However, the minutiae were automatically grouped based on the average minutia quality of the set using the NBIS quality measure and then again using the proposed method quality measure. The graph indicates an increase in matching performance of the Good

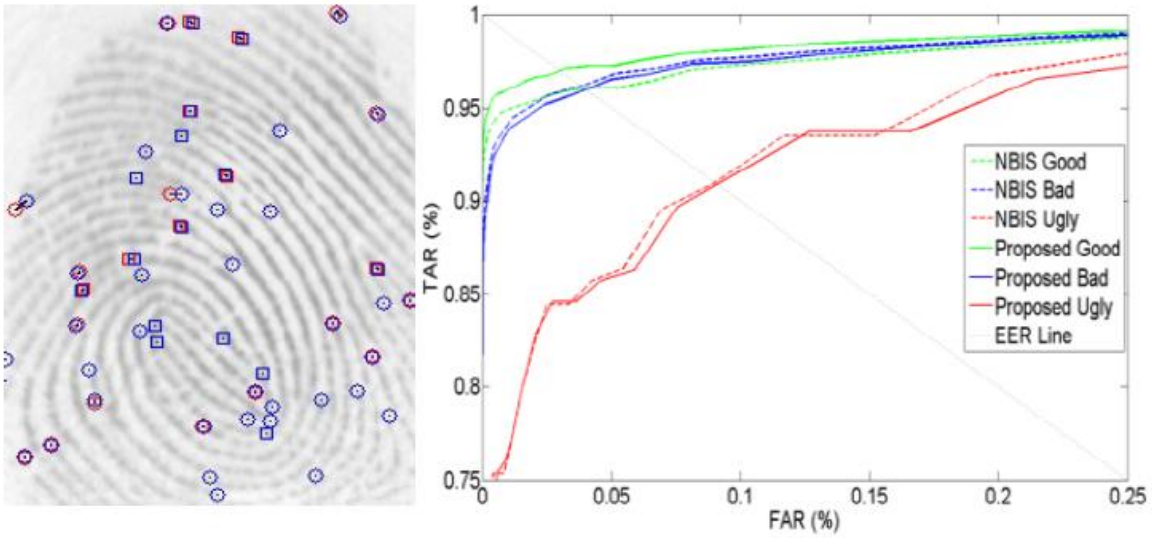

(a) (b)

Figure 3-20: (a) shows an example of localized minutiae from FVC 2000 DB1. The same database was used to measure quality assessment performance (b). A ROC curve with EER is shown to assess performance.

Table 3-6: **Quality assessment accuracy using NIST SD27 latent prints with ground truth.**

Print Type	Method	Quality	% Improvement
Good	*NBIS*	29.65	11.74
	Proposed	33.13	
Bad	*NBIS*	26.88	14.92
	Proposed	30.89	
Ugly	*NBIS*	30.50	17.15
	Proposed	35.73	
All	*NBIS*	29.01	14.62
	Proposed	33.25	

quality group generated by the proposed method and a decrease for the Bad and Ugly groups. Using the EER as a threshold, the Good quality group True Accept Rate (TAR), which is 1 0 FRR, increased from 95.9% to 97% and the FAR decreased from 4.1% to 3.0%, providing a net performance gain of 2.1% when grouping based on the proposed quality assessment measures.

3.6 Summary

In this chapter, we outlined the steps involved in feature extraction for fingerprint analysis, with an emphasis on low quality images, or images with noisy backgrounds. Automated systems are necessary for the high throughput required by enrollment programs such as the DHS's US-VISIT. With the large volume of digital fingerprint images obtained by these programs that need to be processed, the quality of the samples cannot always be controlled. While training is provided to border control agents and other personnel to obtain optimal samples, environmental conditions limit the effectiveness of such preparation.

Here, we proposed a new method for segmenting the fingerprint region from the background of the image, a method for detecting features and refining the descriptors of the same using a recursive Bayesian estimator. The results lead to better matching performance by revealing higher authentication rates than traditional feature extraction approaches, specifically in low quality images.

Chapter 4

Extended Features: Ridges

4.1 Introduction

Traditionally, fingerprints are reduced to a set of discriminating feature points that represent the overall friction ridge surface. These feature points, called minutiae, are used to compare a probe print to a known exemplar. As the surface area of the fingerprint decreases or the reliable friction ridge area decreases, such as in latent or other low quality prints, the number of minutiae also decreases, leading to lower identification performance. To overcome this problem, extended feature sets have been proposed to make up for the loss in minutiae. Extended features traditionally have been used by latent examiners for making identifications, however, recently a push is being made to automatically detect and extract this set of additional features.

There are costs associated with extended feature set extraction for both human examiners and AFIS vendors. In the case of human examiners, there is an additional amount of processing time needed to locate and annotate the fingerprint image with these additional features. Since extended features typically fall into the category of Level 3 features, it is necessary to acquire at least a 1000 ppi digital image of the fingerprint. This leads to a larger file size as well as additional processing time. While most AFIS vendors are willing to adjust optics to accommodate the increased resolution, they have not been motivated to develop algorithms for extracting the additional features. As reported earlier in Chapter 1, minutia-based matching AFIS technology is already 99.4% accurate. The additional benefit of using extended feature

sets has not been determined to be cost effective, given the support required for research and development. Currently, most of the work with extended feature sets has come from academia for use with improving latent fingerprint matching.

4.2 Previous Work

While the usefulness of extended feature sets has not been comprehensively studied, their usage has been proposed in the literature. Jain et al. [52] first proposed the use of ridges in fingerprint matching, utilizing the structure to determine parameters for optimal fingerprint alignment. An initial correspondence is determined between a pair of minutiae from a probe and gallery image. The x, y translation parameters are found by the difference in location of the minutiae. Sample points are chosen along the associated probe fingerprint ridge and gallery fingerprint ridge. The y- coordinates of the sample points are correlated and an alignment angle is found for the difference in rotation between the two prints. The ridge information is discarded after approximating the alignment parameters. Improvements to this method have been proposed by [68-70] for aligning the fingerprint images before performing minutia-based matching. Ross et al. [71] used ridges for aligning genuine matching fingerprint images in order to model deformation from skin elasticity. None of these methods incorporate the ridge structure similarity into the final fingerprint similarity score.

Feng et al. [72] proposed matching ridges and combining the similarity score with the minutia similarity score. After aligning the templates using the minutiae, sample points along the associated ridges are compared. The sample points are chosen along the ridge at a constant interval, as traced in the skeleton image representation. Each ridge is represented by the polygonal line connecting the sequence of points. The ridges are compared iteratively and a similarity score is computed based on the number of corresponding ridge sample points. Jain et al. [73] expanded on this method by extracting and matching all ridges in the skeleton image.

4.3 Proposed Approach

In this section, we focus on the extraction of extended features that are attainable from a 500 ppi image, the fingerprint ridges. Ridges either can be extracted from the ridge skeleton image or directly from the grayscale image during ridge tracing. Regardless of the image used for extraction, the ridges are represented as a set of pixels belonging to the component. A global representation of the ridge structure is formed as well as a local representation. In the global representation, a graph is created with the minutiae represented as nodes and the ridges as edges. This approach focuses on representing the interrelationships among the minutiae in the fingerprint. The local representation models the physical structure of the ridge itself, the contour, length, and associated minutiae. We propose a cubic spline representation of the ridges connecting the minutiae.

4.3.1 Graph Representation

Here, we introduce an additional feature called a ridge component. A ridge component is the segment formed by starting at a given minutia and tracing along the connected ridge until the adjacent minutia is reached. The extracted segment is a ridge component. Each minutia is assigned an additional set of descriptors indicating the ridge components that are directly connected to it. It follows that a termination will have exactly one ridge component descriptor and a bifurcation will have at least three. The new feature vector for a minutia becomes $\{x_i, y_i, \theta_i, q_i, t_i, r_{1i}, r_{2i}, r_{3i}\}$, where r_{1i}, r_{2i}, r_{3i} correspond to the ridge identification numbers adjacent to minutia i. For a termination, only r_1 is valid.

A ridge connection is a binary indicator between two minutiae describing if they share a common ridge component. These connections can be found by looking at the intersection of the minutiae ridge component descriptor sets. Using this notion of ridge connections, it is obvious to create a graph-based representation of the fingerprint, where each minutia represents a node in the graph and the ridge connection indicator determines if an edge exists between each node. From all sub-graphs defined by this representation, ridge clusters are defined by the set of nodes in which there exists a path from each node to every other node.

This set of definitions is illustrated in Figure 4-1 below. In the figure, the tracing of the ridge connecting minutiae "A" and "B" is an individual ridge component. Since the minutiae "A" and "B" are both adjacent to ridge "1", a ridge connection exists between the two minutiae. Since minutia "B" is a bifurcation, it has two other adjacent ridges, "4" and "5". A ridge connection between two minutiae is represented in the graph structure by an edge, creating a path from nodes "A" and "B." An example of a graph representation of the fingerprint ridge structure is shown in Figure 4-1 (c). A path between two nodes in a graph is the set of edges that connect the two nodes. A ridge connection exists in the graph if the edge is labeled as 1. The set of nodes for which a path exists between a node and any other node in the set is called a cluster. It follows that there is a cluster of connected minutiae and of ridges that are adjacent to the minutiae. The ridge components "1", "4", and "5" create a ridge cluster. The individual ridge clusters are color coded in the figure.

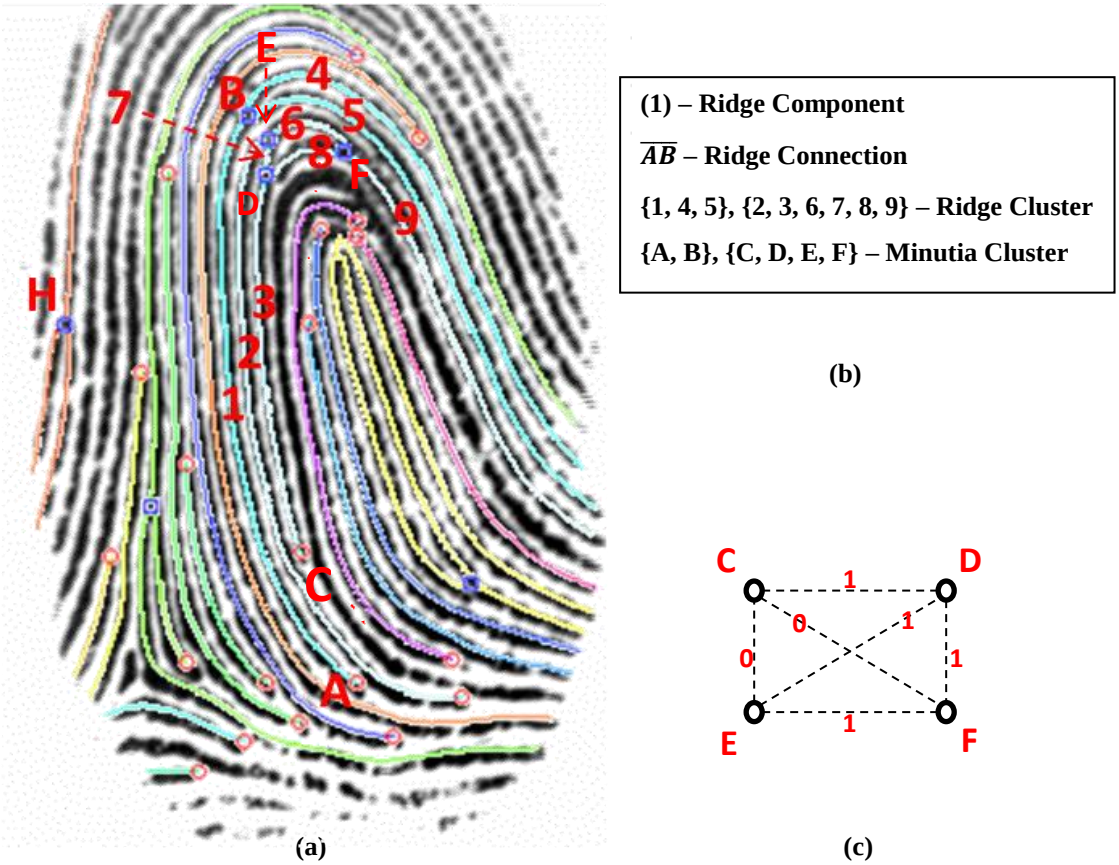

Figure 4-1: An example of (a) fingerprint image with extracted ridge components and minutiae overlain to illustrate definitions provided in (b). In (c), an example of a graph based representation for one of the minutia clusters in (a) is shown.

4.3.2 Ridge Structure Representation

Traditionally, the ridge structure of a fingerprint image is represented by a binary image or sometimes a skeleton of the binary image. The skeleton image is obtained from performing a medial axis transformation on the binary representation of the digital fingerprint image. A single ridge in the fingerprint can be thought of as a curve, represented by a series of connected (x, y) data points. Representing a curved line in space by a mathematical function which exactly fits a set of data points is known as curve fitting. An N- degree polynomial can be used to exactly fit at least $N + 1$ data points. A fingerprint ridge has, on average, 105 pixels making up its ridge component. If we were to exactly represent this ridge as a single function, we would need a 104 degree polynomial. An alternative approach is suggested by way of splines.

A popular method for representing curved lines in space is by spline interpolation. Splines were first used as models in shipbuilding and later in aircraft and automobile design. During World War II, British aircraft builders would construct templates for airplanes using thin wooden strips, referred to as "splines" [74]. These splines were used to model strain energy for a particular piece of aircraft design by bending them around weights laid out on the floor.

This same method is applied mathematically using degree *N* piecewise polynomial functions to create smooth curves. The range of values for which a section of a given polynomial function is valid is defined by a pair of *knot* points. The knot points, or *breaks*, are the data points through which the spline passes, like the weights in the practical example. Each segment between the knot points is called a *piece* of the spline. If there are K knot points, it follows that there are $K - 1$ pieces that make up the spline. The spline is smooth and continuous along the interval (x_0, x_M) where $x_0 < x_1 \ldots < x_M$.

One of the most popular splines is the cubic spline, where each piece has a set of coefficients corresponding to a third order polynomial equation:

$$f(x) = Ax^3 + Bx^2 + Cx + D \qquad (4.1)$$

Here, A, B, C, and D are the four coefficients that define the polynomial for each piece of the spline. Given a set of *K* knot points, the spline is defined as:

$$S(x) = s_i(x) \quad if\ x_i \leq x < x_{i+1} \tag{4.2}$$

where

$$s_i(x) = A_i(x - x_i)^3 + B_i(x - x_i)^2 + C_i(x - x_i) + D_i \tag{4.3}$$

and $i = 1, 2, \ldots K - 1$. In addition to the cubic spline being smooth and continuous, the first two derivatives also are guaranteed to be continuous:

$$S_i(x_{i+1}) = S_{i+1}(x_{i+1}) \quad for\ i = 1, 2, \ldots K - 1 \tag{4.4}$$

$$S_i'(x_{i+1}) = S_{i+1}'(x_{i+1}) \quad for\ i = 1, 2, \ldots K - 1 \tag{4.5}$$

$$S_i''(x_{i+1}) = S_{i+1}''(x_{i+1}) \quad for\ i = 1, 2, \ldots K - 1. \tag{4.6}$$

By modeling the fingerprint ridge as a spline and taking the second derivative of the piecewise cubic polynomial, we can easily approximate the curvature of the ridge at any given point. Since curvature is independent of orientation, we can use this information to match ridges without aligning the candidate ridges.

In Figure 4-2, a cubic spline approximation to a fingerprint ridge is shown in green along with a traditional polygon approximation in red where the sample points are shown as black circles. In this example, there are 16 knot points chosen in order from *0* to *K*, producing 15 cubic polynomial equations making up the pieces to the spline. Rather than fitting the spline to the grayscale fingerprint image, the spline is fit to the skeleton image representation of the ridge curve. In Figure 4-3, three graphs are shown indicating the y-displacement, rate of change, and curvature corresponding to the spline $S(x)$ and its first two derivatives, $S'(x)$ and $S''(x)$, respectively. The y- displacement values are shown with respect to the average y- value for the ridge segment of 300.

We have found through experimentation, there are tradeoffs between the cubic spline approach and the linear approximation. For example, Figure 4-4 shows a fingerprint region centered around a singularity point. The fingerprint is a binary representation of the grayscale image. A cubic spline and linear approximation are shown in green and red, respectively. Figure 4-5 (top) shows a graph plotting the y- displacement of a ridge within that same region, as a function of position along the ridge. Here, the y- displacement is simply the distance from the 0^{th} row in the image. The ground truth position data for the section of ridge around the core point are indicated by black points. The cubic spline and linear approximations for y-displacement also are shown in green and red, respectively. The graph in Figure 4-5 (bottom) shows the error in the two approximation methods. From this graph, we see the linear approximation produces a better fit when the ridge contour is flat and the cubic spline out performs it when fitting to curves in high curvature regions.

We propose a hybrid approach that utilizes the second derivative of the cubic spline fit. When the curvature is above a certain threshold, T_{curve}, the cubic spline is used for approximating y. In all other cases, a linear approximation is used, such that

$$\tilde{y} = \begin{cases} A_i x^3 + B_i x^2 + C_i x + D_i & if\ S''(x) \geq T_{curve} \\ m_i x + b_i & otherwise \end{cases} \quad (4.7)$$

where $i = 1,2,\ldots K-1$.

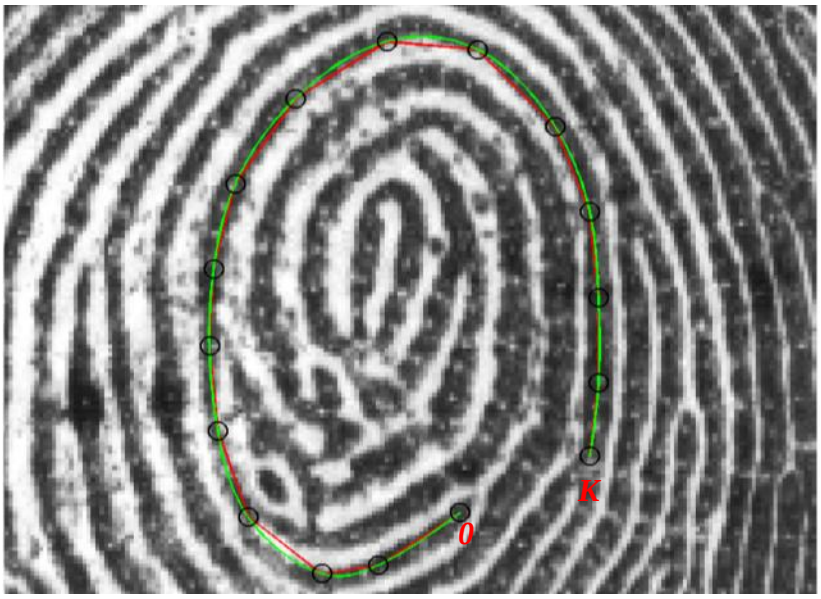

Figure 4-2: A region of a fingerprint with a spline fit approximation overlain in green. Traditional polygon approximation is shown in red and black circles represent the knot points chosen.

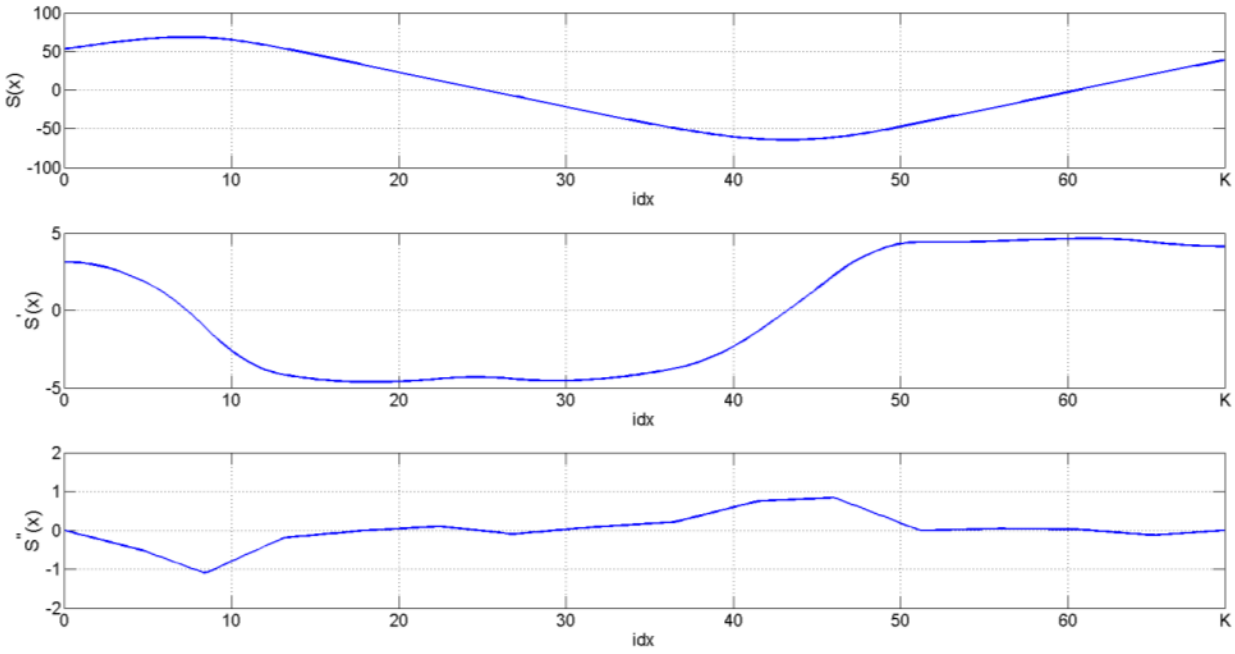

Figure 4-3: Graphs showing the *y*- displacement (top) and first and second derivatives (middle and bottom, respectively) as a function of the index along spline, *S(x)*, shown in Figure 4-2.

Figure 4-4: Region surrounding core point in a binary fingerprint image with cubic spline fit (green) and linear approximation (red) to ridges.

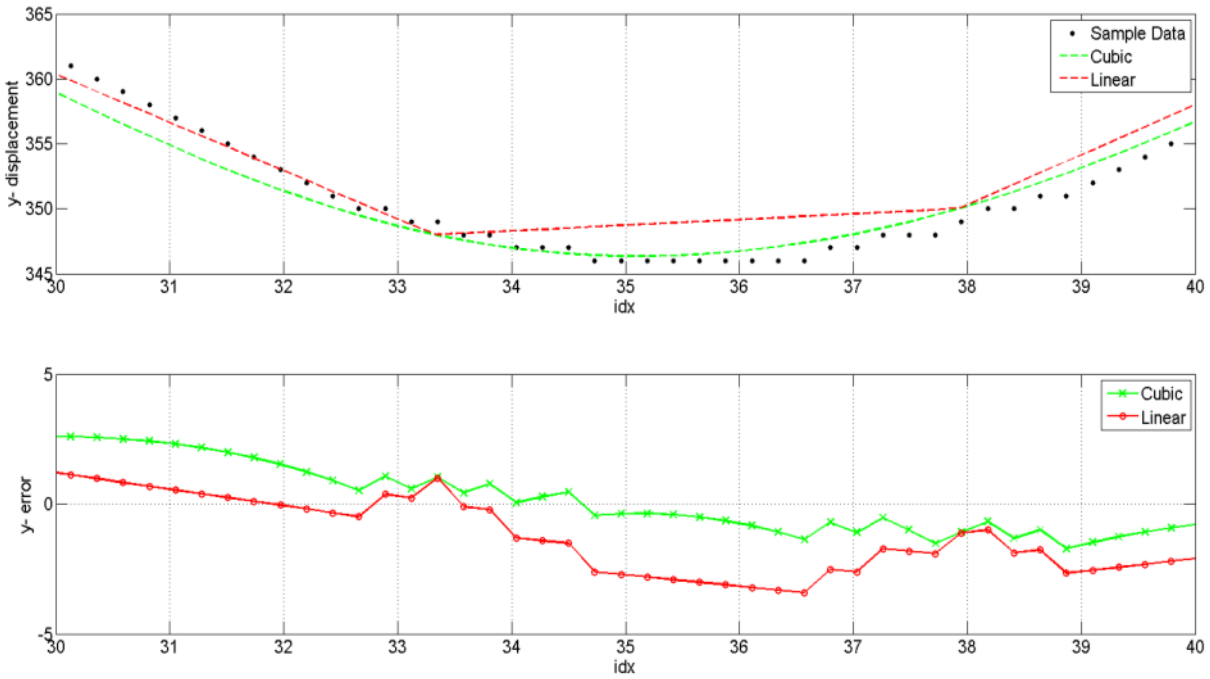

Figure 4-5: Region surrounding core point in a binary fingerprint image with cubic spline fit (green) and linear approximation (red) to ridges.

4.4 Experimental Results

The distribution of the expected number of minutiae in a fingerprint is well known. However, no study is known to have been conducted for ridges. Modeling the expected number of features in a set of sample fingerprints can help facilitate quality analysis. For example, a fingerprint that has a much larger or much smaller number of minutiae than is expected could indicate either a poor quality sample or a rare fingerprint. The same can be said for modeling ridges in the fingerprint. Using a database of 59,673 rolled good quality fingerprint images (Appendix C), we extracted all of the ridge components by tracing the ridges.

In Figure 4-7, the number of all ridges found in the sample database is shown in red and the number of complete ridges is shown in blue. The ridges not belonging to the complete ridge set are those that originate in the fingerprint region of interest and travel outside of the region of interest or a ridge that originates outside the region of interest and passes through the region of interest without terminating or merging with another ridge. In this example, the average number of complete ridge components in a fingerprint image is 80. We also extend this ridge modeling to ridge clusters.

Using the same database, the expected number of ridge clusters formed from a fingerprint and corresponding minutiae and ridge connections is shown in Figure 4-7 (top). The average number of clusters formed in a typical rolled fingerprint image is 53. If we only look at clusters where the size is two nodes or more, excluding clusters made up of a single minutiae point, we get a more reasonable average number of clusters at 19. Finally, we look at the maximum cluster size for a fingerprint represented by the proposed graph structure. From the data, we see that on average a fingerprint has a maximum of 10 nodes forming a cluster.

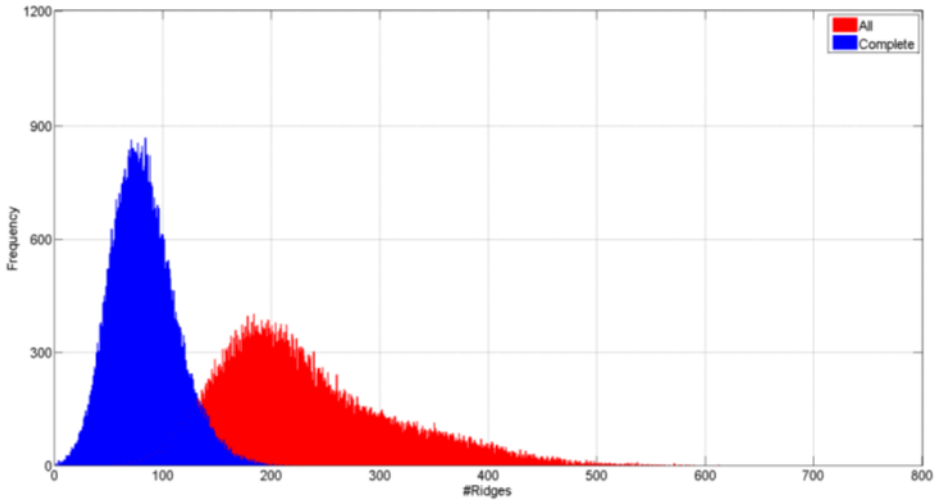

Figure 4-6: Ridge component counts for ridges wholly contained in the fingerprint region (Complete) and the entire set of ridge components (All). Distributions of ridge counts are modeled from a database of 59,673 rolled fingerprint images.

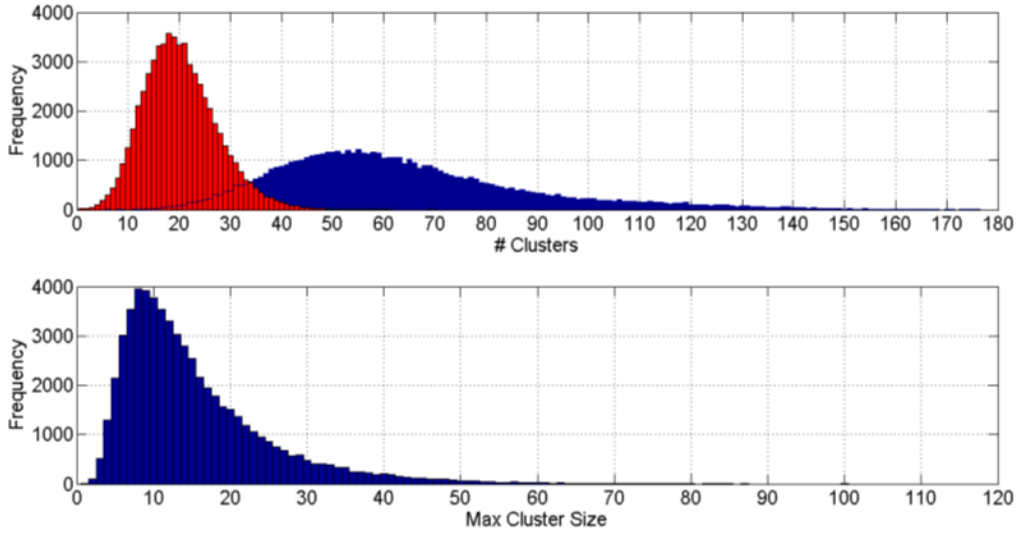

Figure 4-7: Distribution of the number of clusters (top) for all cluster sizes (blue) and those having two nodes or more (red) and maximum cluster size (bottom) within a given fingerprint. These distributions are modeled from a database of 59,673 rolled fingerprint images.

4.5 Summary

In this chapter, we have introduced the concept of extended features, namely the ridge connection feature. We have proposed a scheme for representing a fingerprint as a graph based structure, where the nodes of the graph are minutiae and edges represent the ridge components. Ridge clusters are proposed for grouping sets of minutiae and ridges where a path exists from one minutia to every other minutia. Experiments were conducted to quantify and validate the use of ridge components as well as the clusters they form.

In addition to representing how the minutiae are interconnected by their ridges, we have also proposed a method for representing the structure of the ridge components. We have found that a simple linear polygon approximation is insufficient for modeling the contours of a ridge, specifically in the singularity regions where the curvature is high. Cubic polynomial splines were found beneficial to accurately modeling a ridge component and offer a mathematical means for computing the curvature along the ridge. A fusion is proposed that incorporates both cubic polynomial and linear fits, where linear fits are chosen for intervals with low curvature and cubic polynomial fits are chosen for higher curvature intervals. The fused fit leads to lower residual error when compared to the ground truth data.

Chapter 5

Ridges and Sufficiency

5.1 Introduction

Law enforcement has been utilizing fingerprints to link suspects to a crime since before the early 1900s. Meanwhile, prosecutors have been using this physiological trait as an established form of evidence for prosecuting criminals in courts of law. Recently, this form of evidence has been receiving criticism from defense lawyers who have challenged the scientific backing of fingerprint identification in major cases such as Daubert v. Merrell Dow Pharmaceuticals in 1993 and Kumho Tire Company v. Carmichael in 1999. Ultimately, the Supreme Court delegated the responsibility to federal judges for determining the reliability of expert testimony before allowing it to be admissible [75].

To improve the usefulness of fingerprint evidence in court, the National Institute of Justice requested the help of researchers to develop standardized, statistically tested procedures for comparing fingerprints [76] and determining individuality of the same. Fingerprint individuality, which refers to the premise that a fingerprint is unique to a particular person [77, 78], has spawned the need for and validation of individuality models for fingerprints. While the uniqueness of a fingerprint is commonly accepted because of the lack in contradicting examples, it has never been scientifically proven.

Measuring individuality fundamentally refers to the distinctiveness of a given fingerprint with respect to the population, in other words, the intra- and inter-class variation. Here, intra-

class variation refers to the similarity of two genuine comparisons and inter-class variation refers to the similarity between two imposter comparisons. The main challenge here comes from the variation between two impressions of the same fingertip due to distortion and noise. This can cause two matching fingerprints to appear dissimilar to a degree and two non-matching fingerprints to appear more similar. Human examiners and AFIS alike determine that two prints originated from the same finger if they are sufficiently similar.

5.2 Previous Work

Pankanti et al. [77] offer estimates of probabilities of false correspondence, while developing conclusions that automated fingerprint match performance is not close to the theoretical limit. Chen and Moon [79] develop their own individuality model based on an assumption of uniform distribution of minutiae, and then in later work state that the distribution is not uniform and develop a stochastic model [79]. Zhu et al. developed models that better represent the clustering property of minutiae features and they compute the probability of random correspondence [80].

Recently, Su and Srihari [81] proposed a method for computing the rarity of a latent prints represented by their minutiae. A probability of random correspondence is found between the latent and a database in three steps: 1) registration of the latent print by core point detection and alignment, 2) measuring the probability of the evidence, or how likely it is for the sample to occur, and 3) the probability that a match exists for the evidence in a given database. So far, this is the first known scientific method for computing a rarity measure for a fingerprint.

These methods rely on the use of minutiae for determining individuality. The existence of this type of fingerprint feature is, however, less prominent in partial prints where the fingerprint foreground area is small. In this case, it becomes necessary to utilize additional features, such as ridge relationships and structures to make accurate and reliable conclusions about the similarity of two fingerprints.

5.3 Proposed Approach

According to Pankanti et al. [77], a fingerprint sample, with respect to individuality, is examined in three ways: 1) to determine if one or more fingerprints in a given population is sufficiently similar, 2) to determine the probability of finding a sufficiently similar fingerprint in a target population, and 3) the probability that two non-matching fingerprints are sufficiently similar. Here, we address the examination of partial prints with respect to 1) by measuring the similarity of a given partial print with matching and non-matching rolled prints. A similarity measure based on local minutia neighborhoods is reviewed and an extension to ridge cluster similarity is proposed.

5.3.1 Similarity Measure

In [73], Jain and Feng propose a three step approach to similarity score computation between latent and rolled fingerprints: 1) Local minutiae similarity, 2) global minutiae similarity, and 3) match score computation combining local and global minutiae similarity. These steps are outlined in more detail below.

Given a minutia p in a fingerprint, P, a minutia neighborhood is defined by all the minutiae in P within a R pixel radius around p. Here, R is adapted to the global ridge density of the fingerprint image. The same is also true for a minutia g in a fingerprint G. To measure the similarity between p and g, we examine g for neighboring minutiae with similar distance and direction to each neighbor n^P of p. The distance and direction for n^P and n^G are measured with p and g as reference, respectively. If a neighbor of q corresponds with a neighbor of p, they are considered to be matching. Each minutia n^P with no correspondence in n^G is penalized unless one of the following criteria is met: n^P is unreliable or n^p is outside the region of interest of G when transformed into $G's$ space.

The same method is applied separately to the minutiae in G and the similarity between two minutiae is computed as:

$$s^m = \frac{m_p + 1}{m_p + u_p + 3} \times \frac{m_g + 1}{m_g + u_g + 3}. \quad (5.1)$$

where m_p (m_g) represent the number of matching neighboring minutiae and u_p (u_g) is the number of penalized unmatched neighboring minutiae of p (g).

Finally, a normalized similarity measure is calculated for each pair of minutiae comparisons between P and G to accentuate the minutiae pairs that have high similarity to each other and low similarity to others

$$\hat{s}_{i,j}^m = \frac{(N_P + N_G - 1) \times s_{i,j}^m}{\sum_{k=1}^{N_G} s_{i,k}^m + \sum_{k=1}^{N_P} s_{k,j}^m - s_{i,j}^m}. \quad (5.2)$$

Here, N_p (N_G) is the number of minutiae in P (G) and $s_{x,y}$ is the similarity score between minutia x in P and y in G. Using the normalized scores, the top five most similar minutiae are used to align the fingerprint templates. The transformed minutiae are examined in decreasing order of similarity and points close in location and direction are marked as corresponding minutiae.

5.3.2 Extension to Ridges

In addition to the minutia similarity score based on neighborhoods, we compute a ridge structure similarity score based on the ridge connections between the minutiae. First, the adjacency matrices A^P and A^G are found for the ridge connections that exist among the minutiae sets P and G, respectively. Ridge clusters are formed from the adjacency matrices as described in Section 4.3.1. For each minutia p and g as found in the previous section, we compare the location and direction of its directly connected minutia neighbors.

Let the set of minutiae for which there exists a ridge connection between d_p and p be D_p, we measure the distance and direction between each minutia $d_p \in D_p$. Let C_g be the set of

minutiae within the same cluster as g. If a minutia $c_g \in C_g$ is found in a similar location and direction as d_p is to p, we examine its relationship to g and assign a score appropriately. There are three relational cases that can arise between g and c_g based on the ridge structure: 1) they share a common ridge and are directly connected, 2) they belong to the same cluster and are indirectly connected, and 3) they belong to different clusters, but c_g lies near a ridge that is connected to g.

For each directly connected neighbor d_p of p with corresponding neighbor c_g of g, a score is assigned based on which relationship occurs between g and c_g. The score for r is found by:

$$r = \begin{cases} 3 & if\ Case\ 1\ is\ true \\ 2 & if\ Case\ 2\ is\ true \\ 1 & if\ Case\ 3\ is\ true \\ 0 & otherwise \end{cases} . \tag{5.3}$$

These scores were chosen empirically to give higher scores to ridge clusters that match more closely than others. The total score for the ridge similarity of minutia p is

$$s^p = \frac{\sum_{i=1}^{N_D} r_i}{3N_D} \tag{5.4}$$

where N_D is the number of minutiae directly connected to p. We also handle the case where $D_p = \emptyset$ so that it is not penalized without having comparisons to make. The same process is applied to the minutiae in G and the ridge similarity score between a minutia in P and a minutia in G is finally computed as

$$s^r = s^p \times s^g. \tag{5.5}$$

Using Eqn. 5.2, we compute the normalized ridge similarity score, $\hat{s}^r$. The scores are combined to produce a final similarity score from the local minutiae neighborhood and the local minutiae ridge connection similarity:

$$s = \hat{s}^m \times \hat{s}^r. \tag{5.6}$$

The top N most similar minutiae are used to register the latent fingerprint with the rolled print. Correspondences between minutiae of the latent and rolled print are found by comparing the location and ridge flow direction of the transformed points. In addition to the number and correspondences of matched minutiae, we also return the number of matched minutiae that share similar topological structure.

Finally, a similarity score, S, between the latent and the exemplar is computed from a quantitative and a qualitative score:

$$S = S_{mn} \cdot S_{cn} \cdot S_{mq} \cdot S_{cq}. \tag{5.7}$$

Here, S_{mn} and S_{cn} are the quantitative scores for matched minutiae and ridge clusters, respectively. S_{mq} and S_{cq} are the qualitative scores for matched minutiae and ridge clusters, respectively.

$$S_{mn} = \frac{M_m}{M_m + 8}, \tag{5.8}$$

$$S_{cn} = \frac{M_c}{M_c + 3.5}, \tag{5.9}$$

$$S_{mq} = S_d \cdot \frac{M_m}{M_m + U_M^L} \cdot \frac{M_m}{M_m + U_M^R}, \tag{5.10}$$

and

$$S_{cq} = \frac{\sum_{i=1}^{M_m} \frac{M_i^L}{N_i^R}}{M_m}. \tag{5.11}$$

Here, M_m is the number of matched minutiae and M_c is the number of matched minutiae that also share similar ridge connections. The constants 8 and 3.5 represent the expected number of matched minutiae and similar ridge connections for a low quality latent. These values were derived from observations from a sample database of partial fingerprint images. S_d is the average similarity of the matched minutiae from Eqn. 5.6. U_M^L and U_M^R are the number of unmatched minutiae in the latent and rolled print, respectively. Finally, given a matched minutia in the latent, l_i, M^L is the number of minutiae belonging to the same cluster. N^R is the number of unique clusters that to which corresponding minutiae in the rolled print belong. This produces high scores for large clusters in a latent print that are matched with minutiae in the rolled print that also belong to the same cluster.

In Figure 5-1, a region of a fingerprint is shown that demonstrates minutia and ridge connection correspondences. In the figure, the minutiae belonging to the fingerprint image shown are overlaid as blue squares. The red circles correspond to minutiae positions from a genuine matching fingerprint before registration. The solid lines connecting the minutiae of the same template represent ridge connections, i.e., the minutiae share the same ridge. The dotted black lines indicate correspondences between the two templates. Corresponding minutiae that also share ridge connections with other corresponding minutiae receive high scores in our ridge similarity extension.

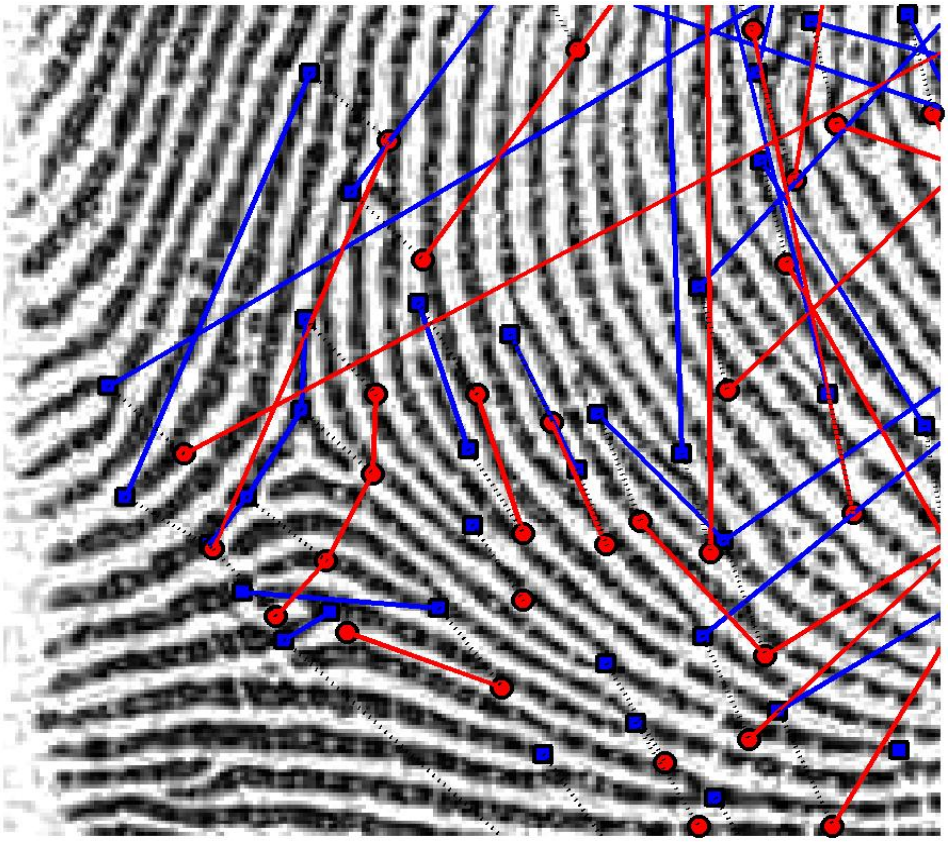

Figure 5-1: Region of a fingerprint image with minutiae marked in blue. Minutiae from genuine match template are marked in red. Solid lines connecting the minutiae indicate ridge connections and black dashed lines indicate corresponding minutiae between templates.

5.4 Experimental Results

Using 1000 rolled fingerprint images scanned at a resolution of 500 ppi, we conducted an experiment to determine the identification rate as a function of minutia count. First, we found a correspondence between the number of minutiae and fingerprint area size. We reduced the minutia set based on the density of each minutia; measured by its distance from the entire set of minutiae in the print. The minutia corresponding to the median density is chosen as the center of mass when shrinking the fingerprint region. The region is reduced to x percent of the original fingerprint, where $x = 90, 80, .., 10, 5$.

5.4.1 Partial Print Observations

In Figure 5-2 (a), a boxplot is shown indicating the expected area of a fingerprint region as a result of reducing the image by a percentage. The area is measured in pixels and is based on a 500 ppi fingerprint image. In Figure 5-2 (b), the result of reducing the area around a minutia with a given neighborhood density on the number of minutia is shown. The graph shows a boxplot indicating the range of data as well as a plot showing the average decline in minutia count as a function of reduction. We repeated this experiment for the lowest and highest density minutiae. These results are indicated in the graph as the red and green dashed plots.

According to [82], a fingerprint representing a region of $0.5'' \, x \, 0.7''$ is regarded as a partial print. In addition, the claim is made that any print with less than 12 minutiae is considered to be partial. This is close to the median minutia count we observed in the latent database SD27 from NIST, where the median count of 258 latent prints is 17 minutiae. Individually, we see from Figure 5-3 (a) median minutia counts of 27, 17, and 11 for the good, bad, and ugly quality latent prints. The quality groups for the fingerprints were decided by a group of latent print examiners.

Using the information reported in this figure, we can conclude that a given partial fingerprint, regardless of quality, will have approximately 17 minutiae. From (b), we can interpolate the percentage of fingerprint area a rolled print would be reduced to in order to be left with this number of minutiae. In this case, a latent having 17 minutiae implies that the sample has 85% less reliable friction ridge surface area than its rolled counterpart. Looking to (a), this

corresponds to a $4x10^4\ pixel^2$ region in the image or an $0.4\ x\ 0.4$ inch area of the finger. For the worst case ugly latent prints, a count of 9 minutiae corresponds to 92% of the original ten-print image or $0.28''\ x\ 0.28''$. A typical rolled fingerprint region is about $1.0''\ x\ 1.2''$ and has around 100 minutiae.

5.4.2 Feature Sufficiency

In this experiment, we compute the minutia similarity score between a set of 200 partial prints generated from the set of 1000 rolled prints. Each partial print has at least two genuine matches in the rolled database of 1000 prints; to be exact, there are 634 genuine and 199,366 imposter comparisons. Since we are creating latent prints by reducing a rolled print, the 200 latent to rolled comparisons from the same image are ignored. In Figure 5-3 (b), CMC curves are shown for reductions to 50% – 5% of the original fingerprint region. As is expected, the identification rate drops as the fingerprint region is reduced. A significant drop is measured from 20% to 10% and then again from 10% to 5% where the Rank-1 identification rate dropped from 84% to 63% and 43%, respectively.

Here, we use the simulated latent set corresponding to 10% of the original fingerprint image. This level corresponds with one of the most significant drops in identification rate. In addition, the minutia count for this reduction is reflective of what is seen in a realistic latent database. Similarity scores were computed for the latent to rolled comparisons using minutiae neighborhoods and the proposed ridge extension, individually. When using topological ridge information, the intra-class (genuine) similarity scores were increased by 12% and the inter-class (imposter) similarity scores were decreased by 7% in comparison to the minutia neighborhood similarity scores.

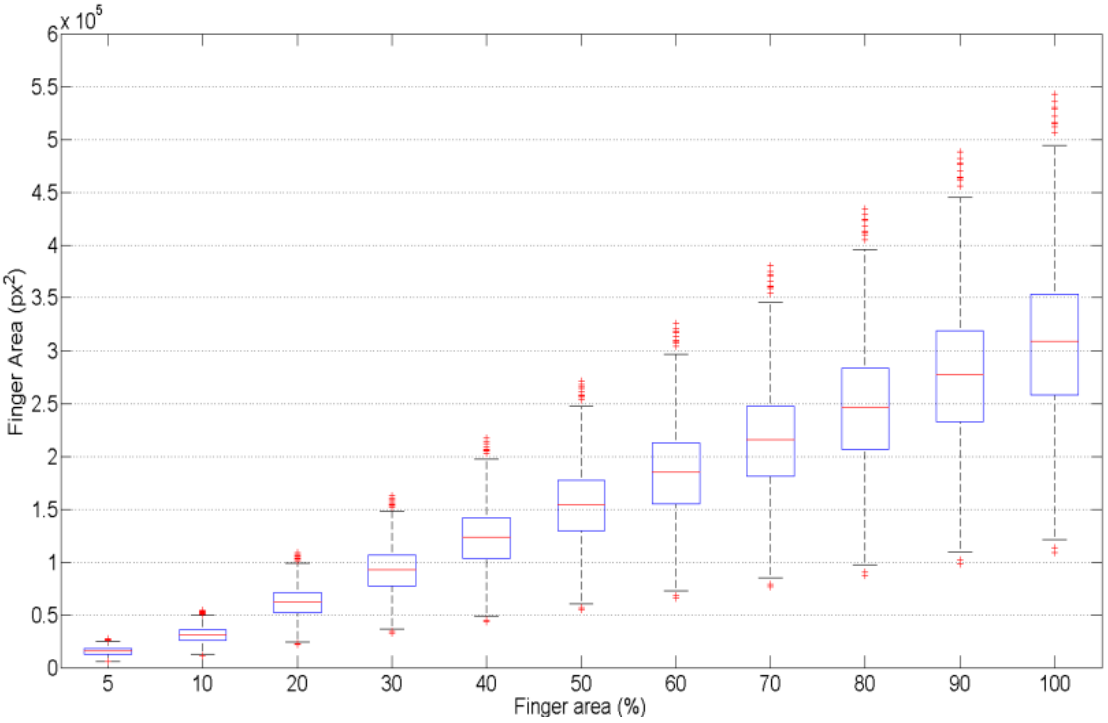

(a)

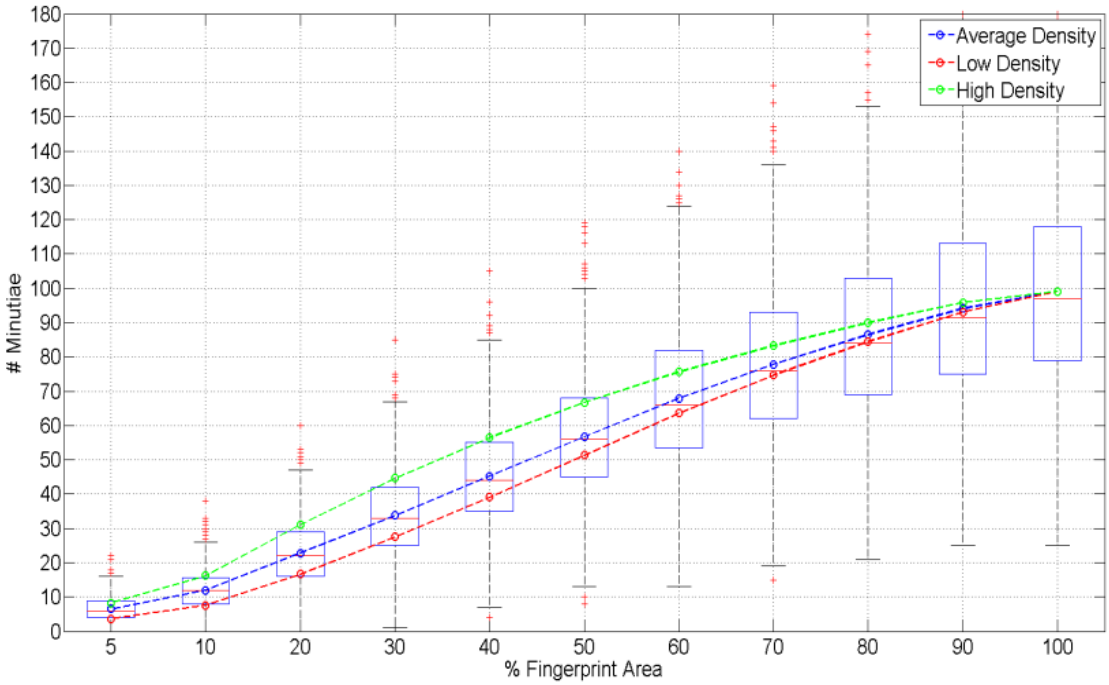

(b)

Figure 5-2: (a) Partial fingerprint area as a percentage of the original rolled print vs. partial print area in $pixels^2$. (b) Partial fingerprint area as a percentage of the original rolled print vs. minutia count.

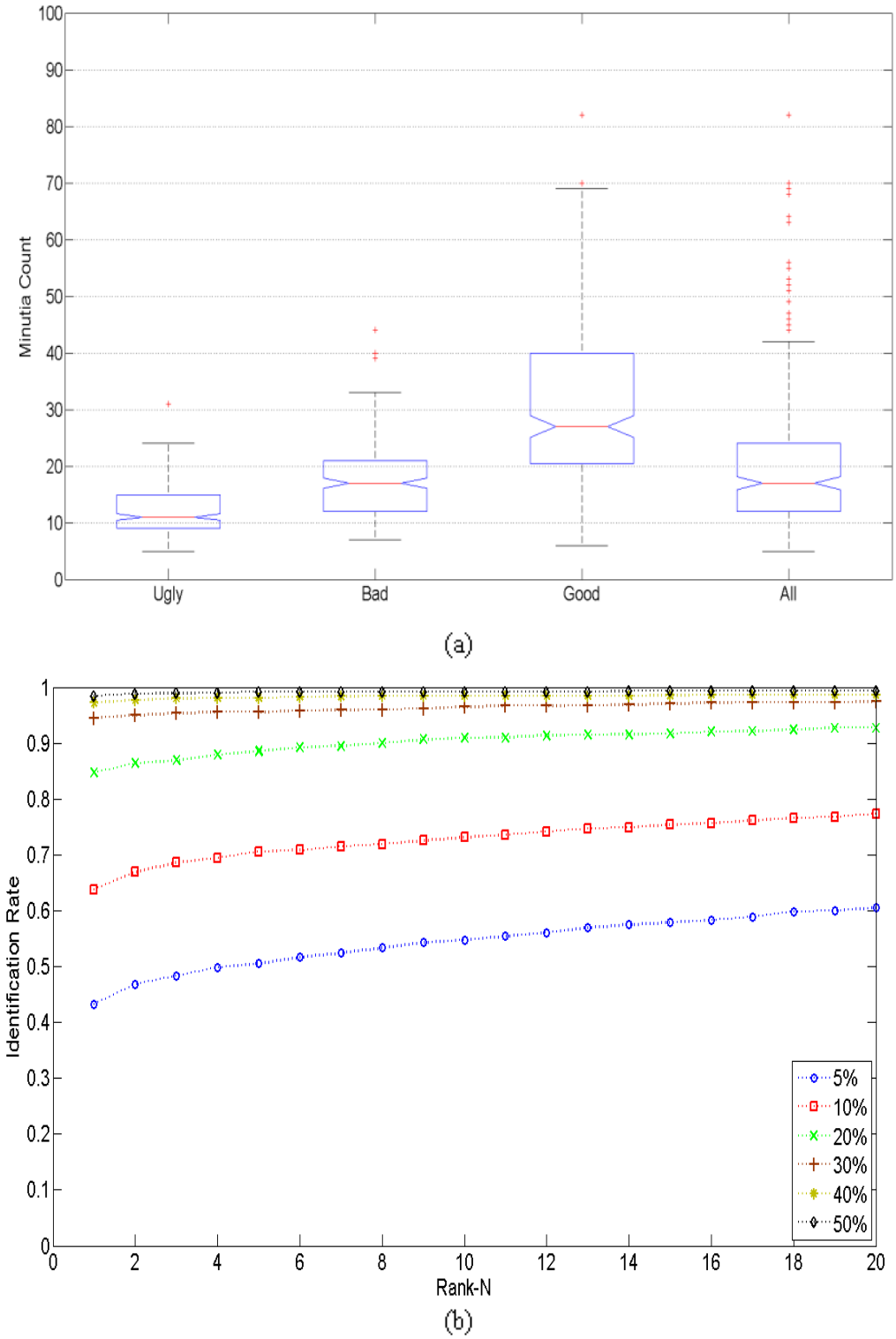

Figure 5-3: (a) Expected minutia counts for varying quality partial prints as measured from SD27. (b) CMC curves for 200 partial prints compared to 1000 rolled prints for foreground regions representing 50% - 5% of the original rolled print.

5.5 Summary

In this chapter, we have introduced the concept of sufficiency for identifying partial fingerprints. We have provided background on prior work involving minutia-based similarity scores for comparing partial to rolled prints. This method for measuring fingerprint similarity with partial prints is extended to include ridge information. A ridge similarity score is computed between two minutiae by utilizing the ridge connection information. This score is combined with the minutia neighborhood similarity score to produce a similarity score between two minutiae. A final similarity measure between two sets of minutiae and corresponding ridges is derived from these scores.

We reduce a set of full prints to create realistic partial fingerprints. Through experimentation, we show a significant drop in identification of partial prints when the fingerprint region drops below 20% of the full print. By including topological ridge information in the computation of similarity, we are able to achieve an increase in intra-class similarity (genuine scores) and a decrease in inter-class similarity (imposter scores) over a minutia-only based similarity measure. The imposter and genuine score distributions were spread further apart by almost 20%. The increase was observed for a group of partial prints that contain 10% overlap with their corresponding full print. To continue the study of sufficiency, more experiments should be conducted on the partial print sets under 20% of the original full fingerprint image. During our experiments with the 5% partial prints, only a slight improvement to the similarity scores was measured when topological ridge information was used.

We have concluded that using ridge connection information improves the level of sufficient detail that can be extracted from a partial print; however, a minimum friction ridge area must be found to improve upon a minutia-based identification of partial prints. A relation should be developed indicating the improvement to similarity score computation (increase in genuine scores and decrease in imposter scores) as a function of decreasing partial print size. In addition, a relationship between features and partial print size will indicate the smallest possible region that can deliver a sufficient set of features for identification. The features should include the number of minutiae, size of ridge cluster, and number of clusters.

Chapter 6

Temporal Analysis of Fingerprint Sequences

6.1 Introduction

Since the first use of fingerprints for human identification, the extraction of features has been confined essentially to a static representation of the fingerprint. Whether using traditional methods with inked cards, or newer techniques with live-scan systems, feature extraction and analysis have depended on examination of a single image. A consequence of single-image analysis is that some portions of the print may be missing or low in quality, due to the variation in image quality throughout an image capture.

It is well known that as a finger is applied to a solid, uniform surface, the skin undergoes change according to its elasticity, the ability of the skin to stretch and compress. The act of placing a fingertip against an imaging surface therefore causes small deformations that affect the resulting digital image representation. A number of distortions are caused by the elasticity of the skin in conjunction with changes in pressure during the impression, such as an increase (decrease) in ridge density due to compression (stretching) of the skin, as well as non-linear distortion of ridge flow from frictional forces during the lateral shifts in position of the center of mass.

Newer image-capture systems offer the capability to correct some of the effects of distortion. Noncontact sensors [83, 84], for example, avoid problems due to skin elasticity entirely, but these have not been widely adopted. Live-scan systems such as [17], however, are

very common, and offer the potential for improved analysis of friction-ridge patterns even in the presence of small deformations.

A typical live-scan system produces a sequence of images during the time that a finger is in contact with the imaging surface. These images are used to determine when the finger has become stationary. A final, single fingerprint image is retained at that time, disregarding data from the image sensor prior to the time of capture.

Figure 6-1 demonstrates the variation in feature descriptors throughout an enrollment sequence caused by ridge compression. Figure 6-1 (a) and (b) show a region of interest in the first image and last image from a sequence of 18 images taken from a live-scan system. In this example, all images in the sequence were marked as the highest quality by a commercial fingerprint-analysis system. During ridge compression, a termination may appear to change to a bifurcation as neighboring ridges are pressed closely together. This also can be a result of the fingerprint valley coming into contact with the imaging surface as the amount of pressure is increased. Figure 6-1 (c) shows a minutia and its neighboring ridges as they are detected throughout a sequence. The minutia was originally detected as a termination and then later as a bifurcation. Also notice the change in placement of the minutia; this is not only attributed to skin distortion, but is also affected to a degree by the change in type.

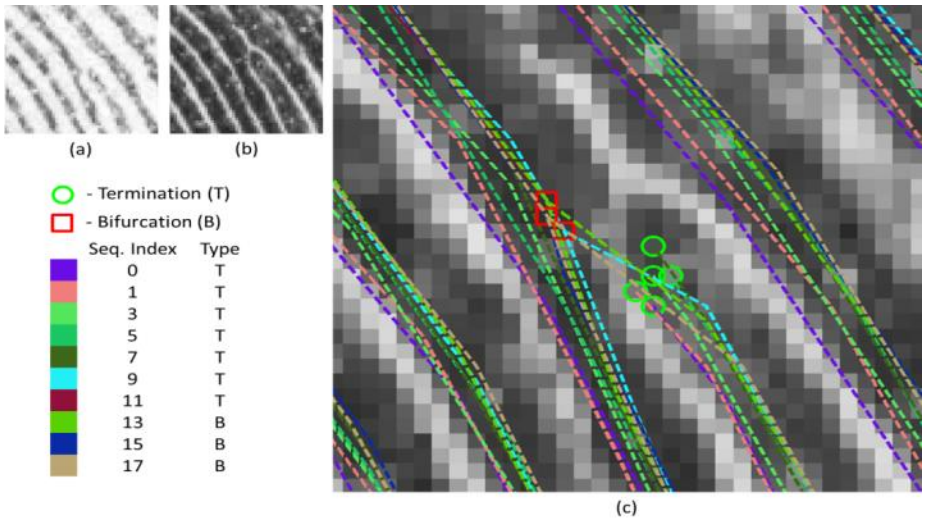

Figure 6-1: Single minutia tracked throughout an 18-image impression sequence. (a) First image from impression sequence and (b) final image from impression sequence, (c) final image from impression sequence with ridge structure and minutia type overlain for select images in the sequence. The minutia was considered reliable throughout the entire sequence.

Here, a novel method and system for fingerprint analysis using a sequence of fingerprint images is proposed. The approach uses the sequence of images to extract and track minutiae for temporal analysis during a single impression. The data obtained from the temporal analysis is then used to build a composite template. In a sense, we are concerned with the use of images that are discarded by live-scan imagers. Because the amount of pressure typically increases as the finger is applied to the sensor, and because the amount of distortion in the image is correlated with the amount of pressure, it follows that the discarded images should contain a great deal of information prior to the fingerprint being distorted.

The benefits of temporal analysis include the ability to improve the reliability of fingerprint features due to change in intensity and direction of pressure forces applied while the image sensor is capturing data. A dynamic analysis provides for the acquisition of more fingerprint surface area, the ability to recover lost data about low quality regions in the final image, and the potential to correct non-linear distortions due to skin elasticity.

In the method proposed here, minutiae are extracted and tracked throughout the sequence to create a composite feature set obtained from the entire set of images. The probability that a given minutia exists is estimated using data collected throughout the sequence, allowing for the detection of minutiae that may not be present in the final static image. There are at least two scenarios in which a minutia would not be detected in the final image, but could be detected from temporal analysis:

1) the fingerprint region in which the minutia exists is no longer making contact with the scanner;
2) the region in which the minutia exists is no longer of sufficient quality to allow for reliable detection.

Figure 6-2 shows an example that compares minutiae found from temporal analysis with those found from using just the final image, simulating a static capture.

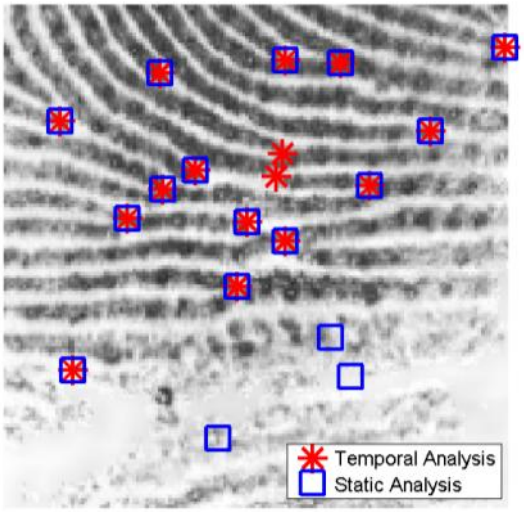

Figure 6-2: Part of final image from an impression sequence. Minutiae were detected separately from static image (blue squares) and temporal analysis (red asterisks). In this particular example, an additional five genuine minutiae were detected and three false minutiae rejected when using the temporal analysis.

Our approach is largely concerned with the increase and decrease in ridge densities and their effect on local region quality variance occurring throughout the image sequence. These changes result in undetected minutiae, unreliable minutiae, and errors in minutia type due to changes in appearance over the sequence. The two common types of minutiae, terminations (ridge endings) and bifurcations (ridge branchings), can be tracked and used during the matching process when comparing the similarity of two corresponding minutiae.

6.2 Previous Work

Combining multiple impressions of the same fingerprint has been proposed in the literature [85-88]. Fingerprint mosaicking combines multiple partial prints of the same finger into a larger composite image representing a larger portion of the fingerprint surface area. This allows for fusion of the minutia subsets extracted from each partial print into a more complete subset of the entire set of all possible minutiae that exist in the physical fingerprint. The proposed fusion also has been adopted at the feature level to combine two templates created during feature extraction of each image. The two methods were compared by Ross et al. [89], showing the superiority of feature-level mosaicking over image-level mosaicking.

All of these previous methods seek to combine information from static images that were obtained during separate enrollments of the same finger. In contrast, we propose the analysis of a tightly correlated image sequence that is obtained during a single enrollment. For a particular portion of an image, the quality of the sensed data can change over the sequence. Among other benefits of our proposed approach, temporal analysis allows the system to extract features from images when quality is optimum, or to perform fusion from the entire sequence. Figure 6-3 shows a work flow diagram outlining the key differences between image and feature mosaicking.

In Figure 6-4, a workflow diagram is shown outlining the temporal analysis of a sequence of fingerprint images from a single impression. The proposed temporal analysis is not intended to replace the mosaicking process, but seeks to analyze a sequence of images captured during a single enrollment and reduce the variance in detected features and their descriptors to create a single composite image representing the fingerprint.

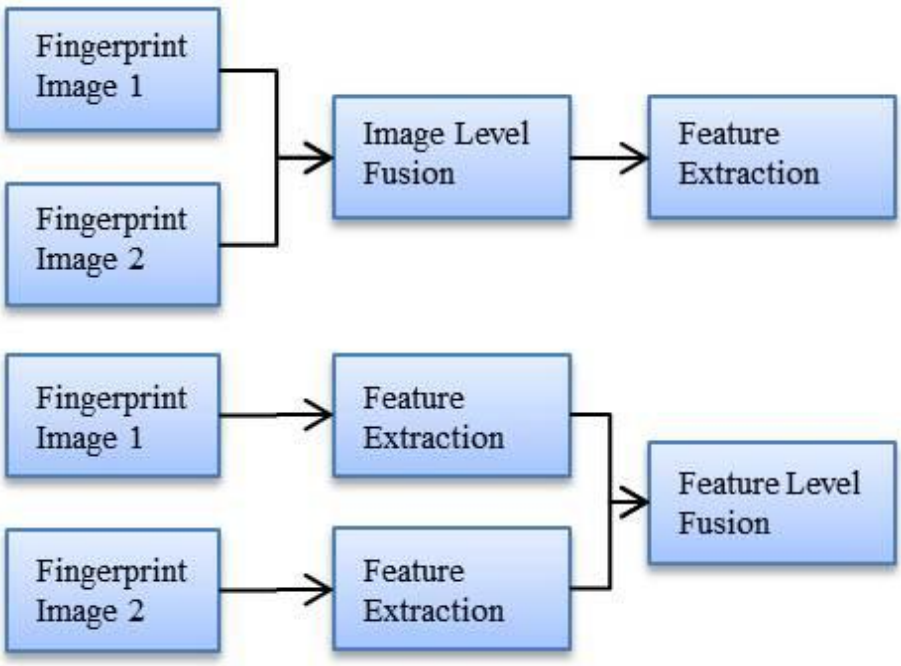

Figure 6-3: Workflow outlining the differences between image mosaicking (top) and feature mosaicking (bottom) methods.

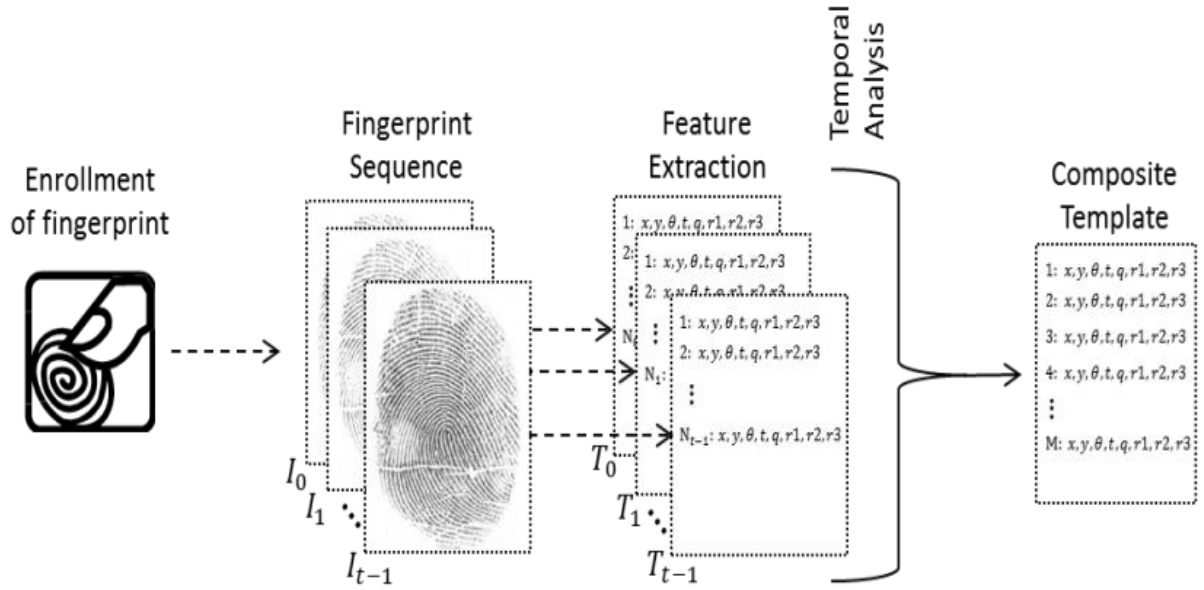

Figure 6-4: Workflow for proposed temporal analysis. The key difference from image and feature mosaicking is that temporal analysis combines data from a single impression rather than from multiple impressions of the same finger

6.3 Proposed Approach

In the method presented here, temporal analysis is performed on a sequence of fingerprint images that is collected during an entire impression. Minutiae are extracted and tracked throughout the sequence to measure the variance in feature descriptors. A single composite template is found by fusing the temporal data from the image sequence. This template is then used for matching.

6.3.1 Extraction and Tracking

The analysis begins by obtaining a sequence of images from a fingerprint scanner during enrollment. A frame is captured at a frame rate of k frames per second within a time interval of t seconds, producing N images of a single fingerprint enrollment. Each image is segmented to find the convex hull of the finger region, enhanced, and processed to extract minutiae and ridge skeletons. A template is created for each image containing minutiae information and ridge components represented as a set of cubic spline curves. Additionally, the images can be

processed in parallel to reduce the computation time. After all templates for each image in the sequence have been created, the analysis begins.

Let $\boldsymbol{I} = (I_1, \ldots, I_N)$ represent an image sequence obtained during a single impression of a fingertip, where the subscripts represent the order in time. Each image is enhanced using Contrast Limited Adaptive Histogram Equalization (CLAHE) [54], and minutiae are extracted from each image using a binarization approach similar to that proposed by [52]. A ridge skeleton is then created by binarizing the enhanced image and iteratively applying morphological thinning. Minutiae are extracted by searching for endings and branch points in the skeleton image. For every image I_t, each minutia has a set of descriptors associated with it, including quality and type. Quality is a measure of reliability determined by analyzing the distribution of grayscale intensities within a region surrounding the minutia. Type is determined simply by properties of the ridge skeleton. Post-processing is applied to remove spurious minutiae, and a template sequence $\boldsymbol{T} = (T_1, \ldots, T_N)$ is created. Each T_t represents the set of minutiae that were detected in image I_t.

Tracking of individual minutiae is conducted using Bayesian estimators. Our method uses a tracking procedure based on Kalman filtering [90] to find minutia correspondences throughout the sequence. Details on the Kalman filter can be found in Appendix B. A filter is initiated using the location of each minutia in the template, T_0. In this method, we choose the Kalman filter over the Particle Filtering approach used in Chapter 4 due to its simplicity and lower computational complexity. Since we are using individual filters to track each detected minutiae throughout the sequence, the choice of a filter with a simple updating scheme is ideal.

For low quality minutiae or minutiae in low quality regions, however, a particle filtering approach can be used which is more robust to background noise. The main difference between the Kalman and Particle filters is in the measurement model distribution and resulting posterior distribution. The Kalman filter assumes a normal distribution centered around the measured value, whereas a particle filter uses a set of discrete weights to model the measurement distribution. The resulting posterior distribution in the Kalman filter is a normal whereas the Particle filter posterior has no known form, but rather is an approximation from a set of samples and associated weights.

Using the models initiated for tracking, the location of the minutia, m_t^i, is predicted in the template T_{t+1}. A minutia m_{t+1}^i exists if a minutia m_{t+1}^j is found within the vicinity of the predicted location, $\widehat{m}_{t+1}^i$. The pair of minutiae are linked from T_t to T_{t+1}. If no minutia is found for the predicted minutia, then m_t^i is labeled as not existing in T_{t+1}. For every new minutia found in T_{t+1} that does not exist in the set, $m_t^i \, where \, i = 1,..N$, a new tracking model is initiated and minutia m_{t+1}^{N+l+1} is then tracked in subsequent images. Here, $l = 1,..M$, where M is the number of newly detected minutiae. The filters are updated for every minutia where a correspondence is found between subsequent images. If a previously detected minutia does not exist in the current image, its position is updated to the predicted location.

The position of each newly detected minutia is examined in preceding images; if the position lies within the convex hull in templates $T_{0:t}$, it is penalized. This handles the case where a minutia lies within the foreground region during a sequence but was not detected; it does not penalize minutiae that are newly detected because of additional surface area being presented to the scanning surface.

This process is repeated for each image in the sequence. An existence probability is found by examining the existence label of $m_{0:t}^i$ for each minutia in the final composite template. A type probability is found from the quality and type of the $m_{0:t}^i$. These probability models are used to predict the existence and type of a particular minutia appearing in the composite template. The existence and reliable type information of a minutia are used to correct the composite ridge data. The system outlined here is described in the flow chart found in Figure 6-5.

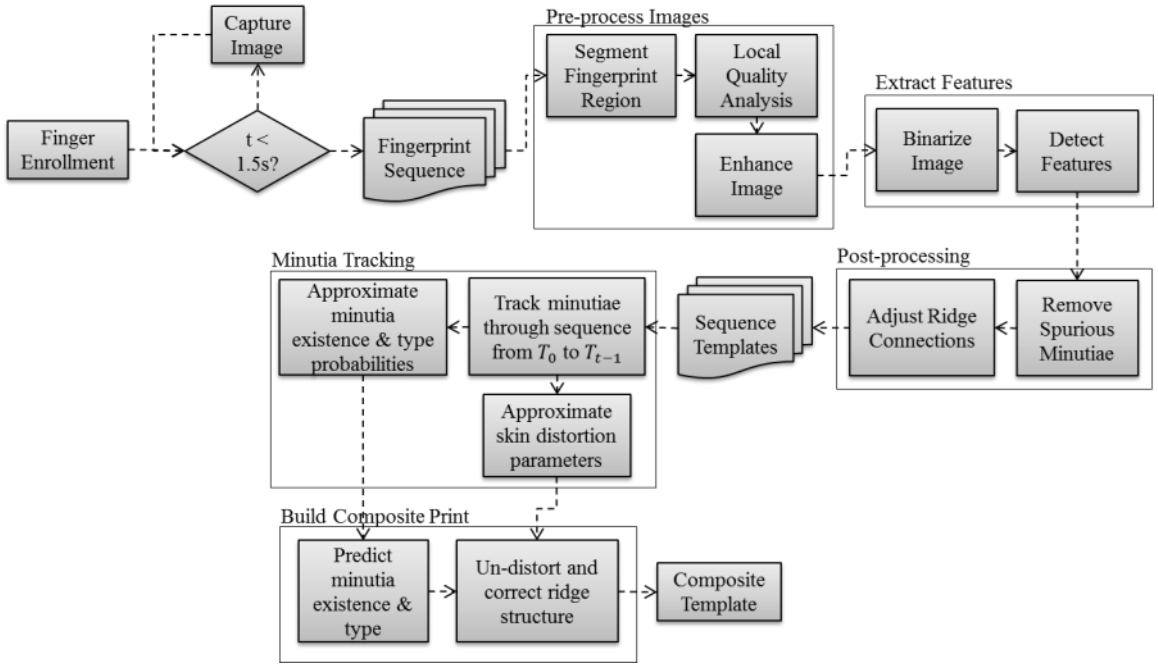

Figure 6-5: Flow chart detailing fusion and temporal analysis of a sequence of images from a single impression.

6.3.2 Template Fusion

Let $T_{i:j}$ represent the set of minutiae that are contained in templates T_i through T_j. This "temporal template" can be expressed as

$$T_{1:t} = \bigcup_{i=1}^{t} T_i. \tag{6.1}$$

In our approach, each minutia in $T_{i:j}$ can be assigned a composite type and an overall quality value. We base these attributes on the probability that a given minutia exists.

Let Q_{tk} represent the quality that has been assigned at time t to minutia m_k, using values [0,100] and $Q_{tk} = 0$ for the degenerate case that m_k has not been detected at time t. For a sequence of N images, we define the probability that m_k exists as

$$p(M) = \frac{\sum_{t=\mathrm{i}}^{N} Q_{tk}}{100(N - i + 1)}, \tag{6.2}$$

where the index i represents the first occurrence of m_k in the sequence. This choice avoids penalizing a minutia for not being visible to the scanner early in the sequence.

To represent the composite type for m_k, we assign a value in the range [0, 100]. We allow a minutia to have three different types, Termination, Bifurcation, and Unknown. The Unknown type is given to the set of minutiae where the type was not determined or the minutia was not detected in the image. Let $Q_{tk_T} \in [0,100]$ represent the quality that has been assigned at time t to a termination minutia m_k, using $Q_{tk_T} = 0$ for the degenerate case that m_k is not detected as a termination. Let Q_{tk_B} represent the same for the bifurcation case. We have

$$p(T) = \frac{\sum_{t=\mathrm{i}}^{N} Q_{tk_T}}{100(N - i + 1)}, \tag{6.3}$$

$$p(B) = \frac{\sum_{t=\mathrm{j}}^{N} Q_{tk_B}}{100(N - i + 1)}, \tag{6.4}$$

and

$$p(U) = 1 - (p(T) + p(B)). \tag{6.5}$$

We choose the minutia type for the composite template by comparing these probabilities, given that the minutia exists:

$$p(T|M) = \frac{p(T,M)}{P(M)}, \tag{6.6}$$

$$p(B|M) = \frac{p(B,M)}{P(M)}, \tag{6.7}$$

and

$$p(U|M) = p(M) - (p(T|M) + p(B|M)). \tag{6.8}$$

Since we know that T and B are wholly contained inside M, $p(T,M) = p(T \cap M) = p(T)$. Using this knowledge and substituting Eqn. 6.2 into Eqns. 6.6 and 6.7, we get:

$$p(T|M) = \frac{\sum_{t=i}^{N} Q_{tk_T}}{\sum_{t=i}^{N} Q_{tk}} \tag{6.9}$$

and

$$p(B|M) = \frac{\sum_{t=\mathrm{i}}^{N} Q_{tk_B}}{\sum_{t=\mathrm{i}}^{N} Q_{tk}}. \tag{6.10}$$

We determine minutia type by the highest probability of occurrence in the sequence:

$$P(T|M) \underset{B}{\overset{T}{\gtrless}} P(B|M). \tag{6.11}$$

Figure 6-6 shows an example of temporal data used to generate a composite template. The data represents the confidence levels of the minutiae along with their types traced through an entire sequence. Dark blue (-100) represents a high confidence bifurcation and dark red (100) represents a high quality termination. Green (0) represents a minutia that does not appear in subsequent templates after first being detected. The black area marks the time in the sequence before the minutia was first detected.

This figure describes the amount of variance in minutia reliability and type throughout an impression sequence. Each row indicates a single minutia as it is tracked throughout the sequence. A row with a single color indicates a minutia type that is constant throughout the sequence and can be considered reliable. Minutiae changing type will be indicated by a change in color along the row, for example, row six changes from red to blue as the type is guessed to be a termination and then later as a bifurcation. Lastly, a row can change in color from blue/red to green; this indicates a minutia that was detected previously in the sequence, but was not detected in the current frame. The variation in guessed type and existence of a minutia throughout a sequence is related to the change in quality of the fingerprint image as it is placed on the sensor during acquisition.

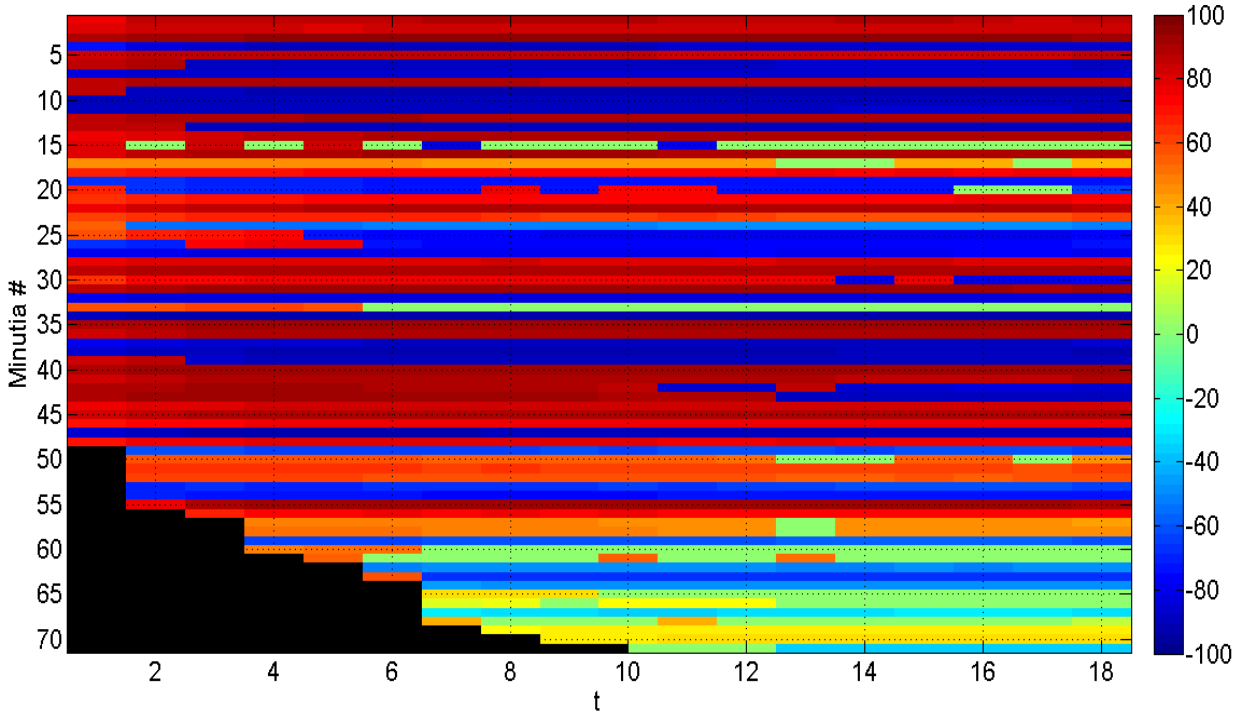

Figure 6-6: Minutiae tracked throughout an entire sequence. Color describes quality and type; -100 (blue) represents a good quality bifurcation and 100 (red) represents a good quality termination.

6.3.3 Ridge Skeleton Adjustments

After determining the true reliability of the minutiae in the fingerprint from temporal analysis, we correct the ridge skeleton map accordingly. For termination changed to a bifurcation, the ridge adjacent to the termination is connected to the closest neighboring ridge. The neighboring ridge is split into two ridge components at the point of connection and assigned new ridge IDs. The minutiae adjacent to this ridge have their ridge ID fields adjusted accordingly. This adjustment results in a new ridge being formed with three ridges in total being adjacent to the newly formed bifurcation.

In the case of a bifurcation turning into a termination, we connect two of the ridges that are adjacent to the bifurcation by a line in the skeleton image. The third ridge is labeled as the terminating ridge and the minutia adjacent to this ridge has its ridge ID adjusted. The two ridges chosen for connection are selected by measuring the angles formed between lines connecting each of the end points to one another, resulting in three angles. We choose the connection that reflects the local ridge flow direction for this region the best. In doing this, we maintain the integrity of the local ridge flow direction when connecting the two endpoints.

Figure 6-7 illustrates how the ridge structure is adjusted to reflect the change in minutia type. In (a), a termination minutia, m, has changed to a bifurcation, m'. The red dashed line indicates the ridge segment that is added to connect ridge 2 with the nearest neighboring ridge, ridge 1. The added segment bisects ridge 1, splitting it into two ridges. In (b), a bifurcation minutia, m, has changed to a termination minutia, m'. The red, blue, and green dashed lines show the ridge segments formed from connecting the endpoints in ridge segment 2 with 1, 3 with 1, and 3 with 2, respectively. In this case, the red segment is chosen as the angle it forms matches closely with the local ridge flow direction. As a result, ridges 1 and 2 are joined to form one ridge and the new termination minutia, m', is adjusted to only be adjacent to ridge 3. Any minutiae connected to ridges 1 or 2 are now marked as being directly connected.

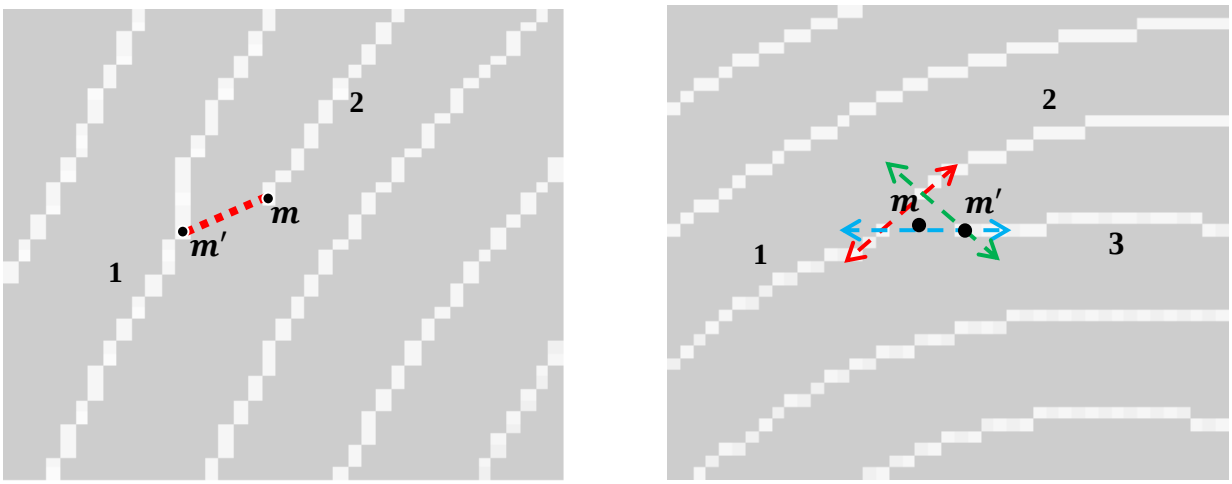

(a) (b)

Figure 6-7: Example of ridge skeleton adjustment for termination to bifurcation (a) and bifurcation to termination (b). In (a), the termination minutia m changes to a bifurcation, m'. As a result, ridge 1 is split into two ridges. In (b), the bifurcation minutia m changes to a termination, m'. The red arrow indicates the connection most similar to the ridge flow direction in the region. As a result, ridges 1 and 2 are connected to form one ridge.

6.4 Experimental Results

This section shows the ability of the temporal approach to capture more minutiae, and to store them in a composite image, than are present in a static image that is traditionally stored from the enrolled impression. We also show the ability of the proposed method to improve matching performance for both plain-to-plain matching and partial-to-plain matching.

We collected a database of fingerprint sequences to evaluate the proposed method. The scanner used was the Identification International digID mini [17]. Images (500 x 1000 pixels) were collected at a resolution of 500 pixels per inch at 10 frames per second. For each sequence, an image buffer was filled for 1.5 seconds while a finger pressed against the scanner. Acquisition began as soon as image intensity variance reached an empirically determined level; this provided roughly 15 images per impression. We collected 5 impressions each of 73 unique fingers for a total of 365 image sequences. Images were enhanced using CLAHE, and then minutiae were extracted using Neurotechnology's VeriFinger 4.2 SDK [66]. Currently, processing of a single enrollment sequence into a composite template is a one-time cost of about 20 seconds running in MATLAB. Also, it is important to note that 96% of the images collected in the impression sequences were considered to be maximum quality by the VeriFinger quality assessment metric. This percentage of maximum quality images indicates that almost all of the images that were collected would be individually acceptable for enrollment as a static image.

6.4.1 Fingerprint Region Reliability

First, we conducted an experiment to analyze the local change in quality of a fingerprint image sequence during an impression. A quality map for each image in the sequence was found using 11x11 pixel blocks. The change in quality of each block was measured throughout the sequence of images. A maximum quality map was created, indicating the maximum quality measured for each block of the image throughout the sequence. This can be thought of as the position in the sequence where each region was captured at its optimal quality. Each block was considered to be added to the final image if the maximum quality of the block was not measured from the final image in the sequence.

Figure 6-8 shows the result of this experiment, plotting the percent of blocks that were not of maximum quality in the final image versus the average increase in quality (reliability) of the blocks that were taken from images earlier in the sequence. Assuming the final image is the traditional static image selected during enrollment, we found that on average, 10% of the composite fingerprint data originated from images captured earlier in the enrollment sequence. In other words, 10% of the fingerprint region found in the traditional static enrollment image was found to be less reliable than at earlier stages of the image capture. Additionally, the average reliability of the blocks added to the composite image resulted in an increase of 13% on average over the corresponding blocks in the final image.

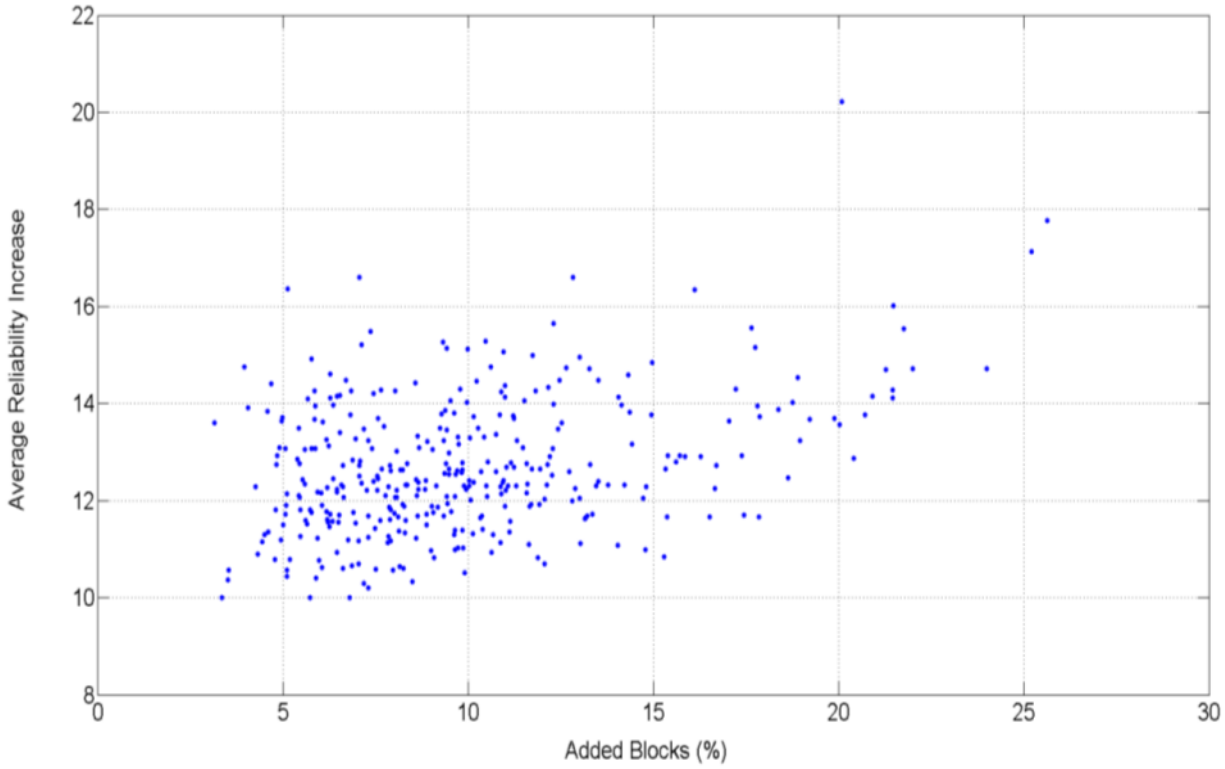

Figure 6-8: Scatter plot showing the percent of blocks that were not of maximum quality in the final image versus the average increase in quality (reliability) of the blocks that were taken from images earlier in the sequence. The data is derived from the 365 image sequences.

6.4.2 Minutia Reliability and Type

Figure 6-9 shows another scatter plot, this time indicating the percentage of minutiae that were detected from temporal analysis versus their average quality (reliability). The plot indicates that a large number of reliable minutiae were detected from temporal analysis over simple static analysis. On average, temporal analysis provided 25% more detected minutiae with an average reliability of 55. In Figure 6-10, minutia count distributions are shown for traditional static template generation and the temporal composite template. The histogram for the composite template is shifted to the right in comparison to the static template histogram, indicating an increase in minutia counts in the composite templates. From the experiments leading to these two figures, we can conclude that a significant number of reliable minutiae were detected at some point in the impression sequence that were no longer found in the final image.

We also conducted experiments analyzing the change in minutia type during a single

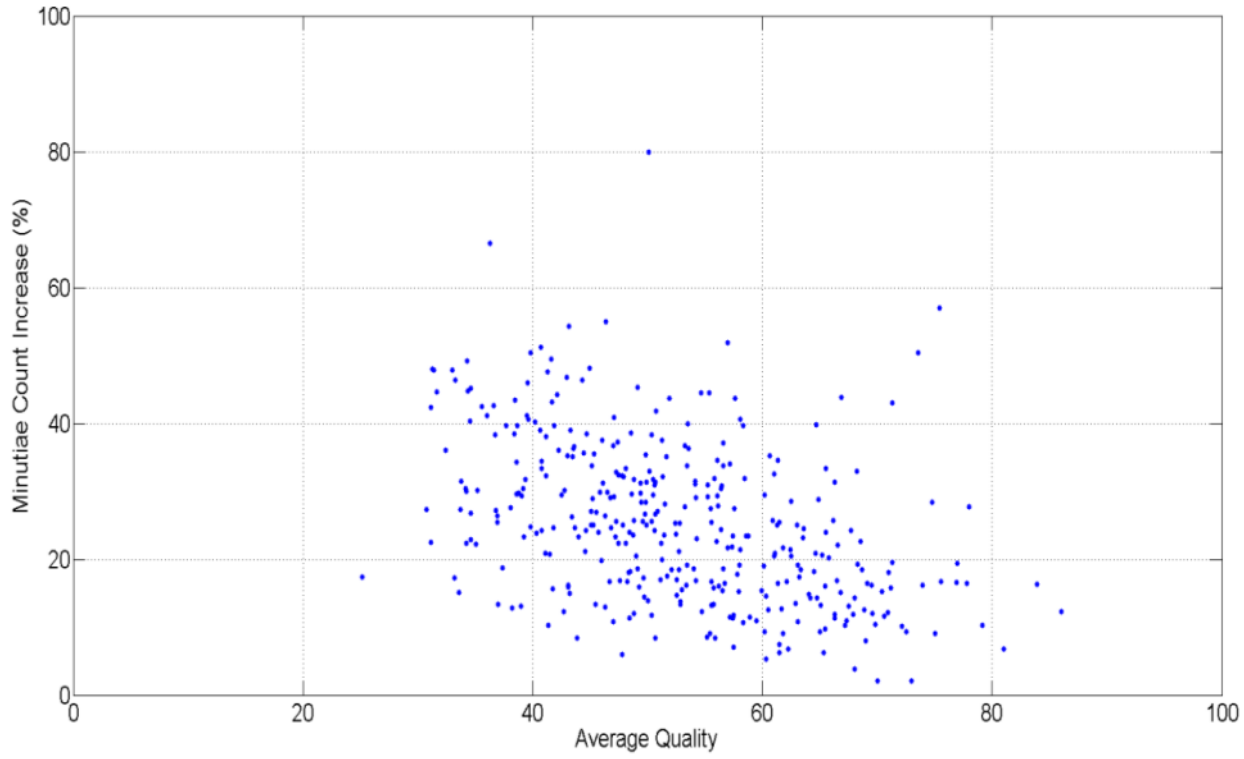

Figure 6-9: A scatter plot showing the number of additional minutiae detected from temporal analysis vs. their average quality (reliability) from the set of 365 sequences.

impression; it was found that variation in type (change between termination and bifurcation) throughout a sequence occurred in 18.2% of minutiae in the data set. Of the minutiae that changed at some point in the sequence, 9.7% changed from termination to bifurcation and 4.2% changed from bifurcation to termination. The remaining 4.3% were those that started and ended as the same type, but changed at some point during the sequence. Using the minutia types from the final template in the image sequence as the correct type, we observed the fraction of correct minutia types throughout each sequence. The results of this experiment are shown in Figure 6-10 as a boxplot and average percent correctness (dashed black line).

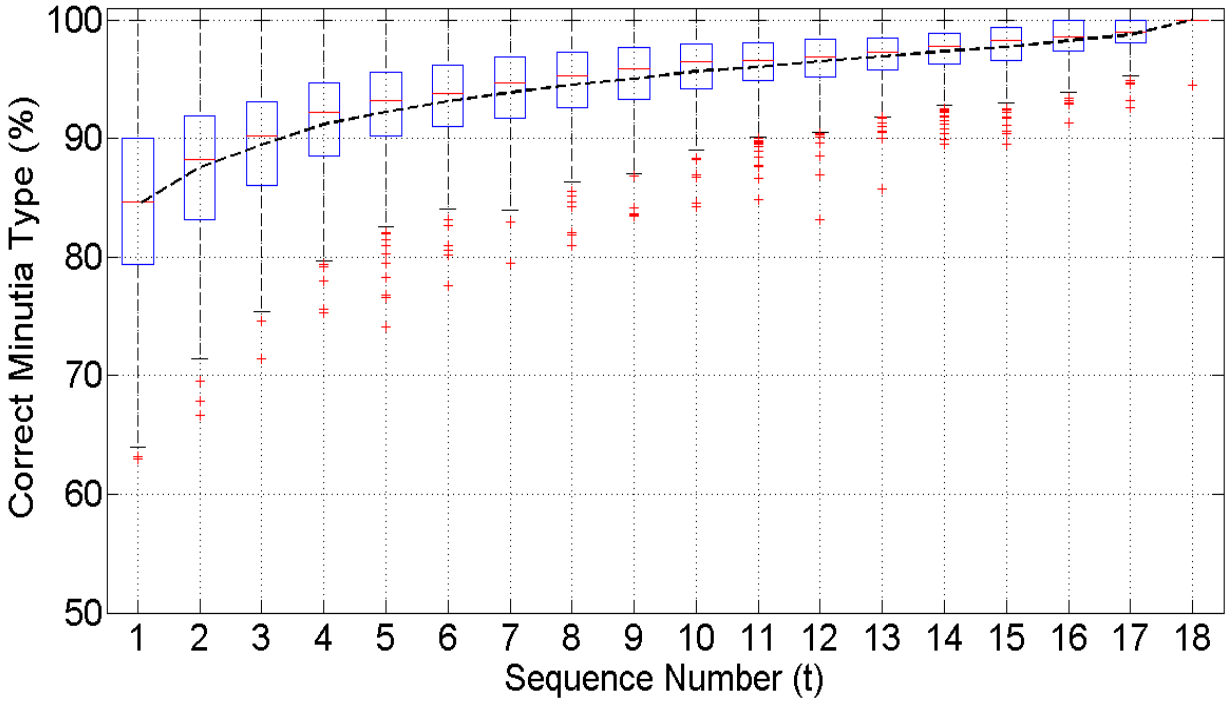

Figure 6-10: Boxplot indicating the percentage of correctly typed minutia throughout an impression sequence. In these results, the final image in the sequence was assumed to be the correct type. Data derived from 365 fingerprint impression sequences.

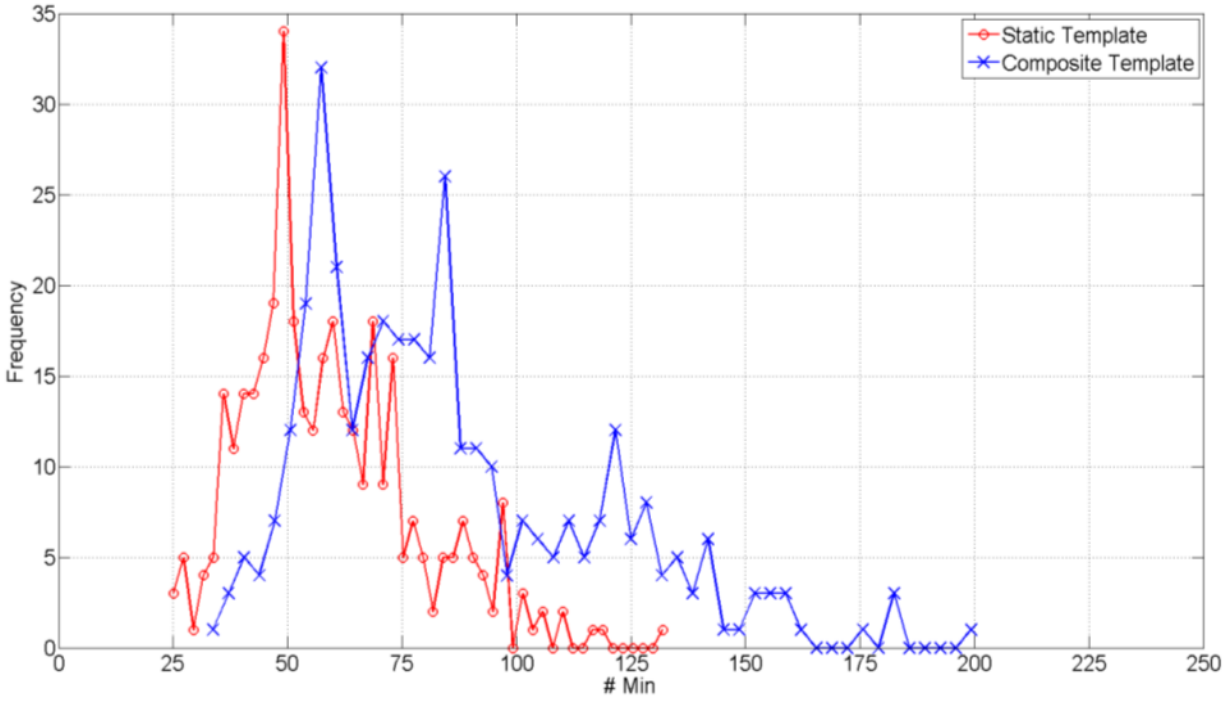

Figure 6-11: Histogram indicating the minutia count frequency for static templates and temporal composite templates.

6.4.3 Plain Print Matching

We first tested the ability of the system to improve plain-to-plain matching. Neurotechnology's minutia-based matcher provided with the VeriFinger SDK was used to compute match scores. Assuming that fingerprint scans ignore images taken prior to the final image; we create a template database representative of traditional static enrollment for the 365 samples. A separate database was created from the composite templates created using temporal analysis. We perform $1{:}\,N$ matching independently for each fingerprint in both databases. For plain-to-plain matching, we saw a minimal improvement. In this case, the EER for the ROC curve plotting the FAR vs. FRR was 3.7%. This might be expected, as the addition of new minutiae has less of an influence on matching when the minutia count is already high.

6.4.4 Partial Print Identification

In Figure 6-12, a Cumulative Match Characteristic (CMC) curve is shown comparing identification performance when the set of static templates were used as an imposter database versus when the temporal composite templates were used. Images and ground-truth data for partial prints are from National Institute of Standards and Technology's (NIST) Special Database 27 [91]. An identification rate of *r* in the CMC plots for rank *n* indicates that the correct match was among the top *n* matches for *r* of all attempts. For Rank-1, Rank-10, and Rank-20, the identification rate was increased by 9.31%, 5.81%, and 5.43%, respectively. These results were found to be significant at a 99.9% confidence level, with $p \approx 0$.

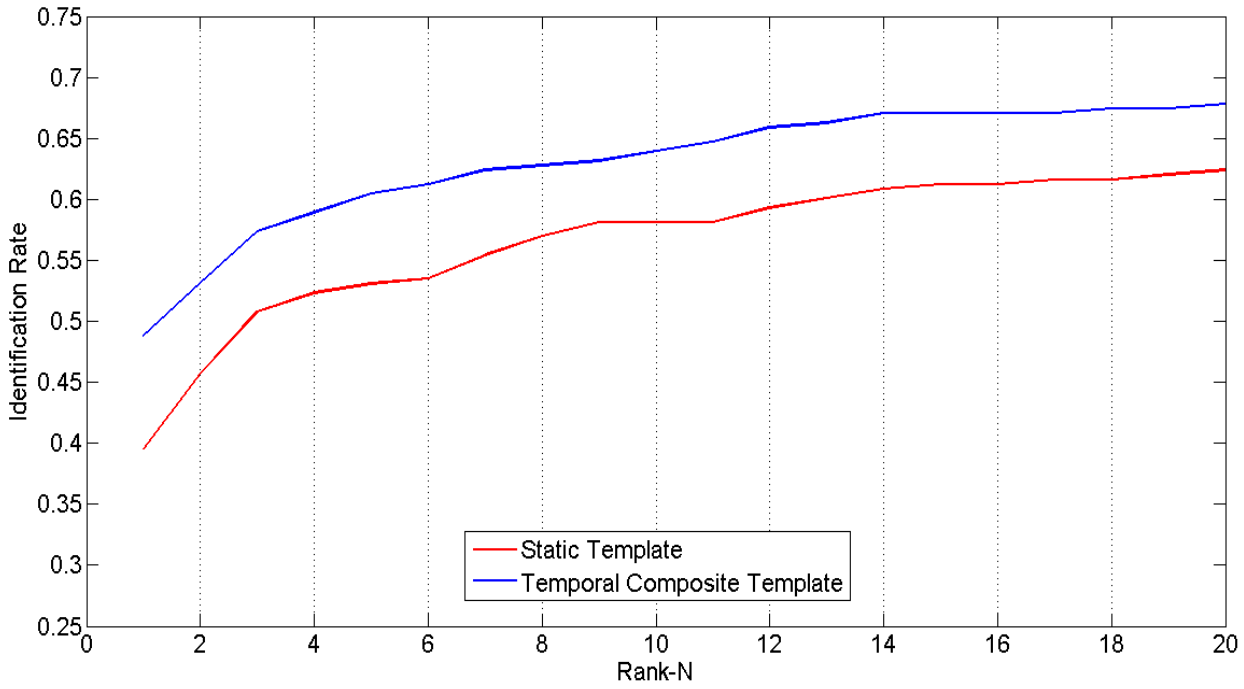

Figure 6-12: CMC plot showing identification rate for partial print matching with static imposter database (red) and temporal imposter database (blue). Genuine scores are computed from the matching ten-print images provided with the database.

6.5 Conclusions

In this chapter, we have introduced a novel approach to fingerprint analysis by introducing the time dimension. Traditionally, fingerprints have been thought of as static images and features are extracted from a single static image. Here, we have proposed a method for capturing a sequence of images from a single impression. The images are processed and composite templates are formed by tracking features throughout the entirety of the sequence. The method has led to more reliable feature extraction, including the detection of additional minutiae and more reliable feature descriptors than can be found in static fingerprint analysis. In theory, processing of the images can be extended to a multicore environment where the pre-processing and template creation can be done in parallel.

This approach is aimed at improving the reliability of feature extraction by addressing the variations in image quality during fingerprint image capture. A confidence measure for minutiae has been proposed that combines information concerning quality and existence over the image sequence. The results have shown a significant improvement in non-identification of partial prints against an imposter database using the proposed composite templates versus the traditional templates extracted from a static image. From temporal analysis, we also were able to determine that the type descriptor for minutiae can be unreliable.

Chapter 7

Summary and Contributions

Fingerprint recognition, one of the oldest forms of human identification, has seen rapid development in the last 20 years. Current state-of-the-art commercial matching systems have experienced high levels of accuracy and throughput speed. This is attributed mostly to the improvements in scanning hardware and quality standards that have been put in place by governing authorities. While fingerprint analysis in the commercial sector has been thought of as a relatively "solved problem", the same cannot be said for application areas in law enforcement and defense application when it comes to latent or partial fingerprint analysis.

In the partial fingerprint domain, it is necessary to require human interaction from latent examiners for both the feature extraction and comparison stages, leading to slow turn-around when requesting identification of a latent sample. Semi-automated systems, such as IAFIS, have been introduced to help alleviate the backlog of requests by providing a means of automatically searching a database of exemplar prints with a manually created template representing the latent print. These systems continue to be predominantly minutia-only matching systems, whereas a latent examiner has the ability to extract and match a variety of features. The result is a low identification rate, due to the inherently low minutia counts found in latent prints.

Additionally, the low identification rate in latent prints is not always a result of low minutia counts. Often times, there are a sufficient number of features for matching, but the reliable overlapping area with the corresponding template is small. There are a few scenarios

where the overlapping fingerprint region in the ten-print might be small: 1) the corresponding region in the ten-print is unavailable, did not make contact with the scan surface during enrollment or 2) the corresponding region in the ten-print is unreliable, the global quality of the print is good, but not all regions in the fingerprint are reliable. This thesis is aimed at improving latent print matching from not only the partial print side, but also improving the extraction from the rolled or plain print.

Publications related to this dissertation are listed below:

- N. J. Short, A. L. Abbott, M. S. Hsiao, and E. A. Fox, "Extraction of Hierarchical Extended Features in Fingerprint Images," presented at the CESCA 2010-001, Blacksburg, VA, 2010. [33]
- K. Hoyle, N. J. Short, M. S. Hsiao, A. L. Abbott, and E. A. Fox, "Minutiae + Friction Ridges = Triplet-Based Feature for Determining Sufficiency in Fingerprints," presented at the IET International Conference on Imaging for Crime Detection and Prevention, London, U.K., pp. 2-9, 2011. [34]
- N. J. Short, A. L. Abbott, M. S. Hsiao, and E. A. Fox, "A Bayesian Approach to Fingerprint Minutia Localization and Quality Assessment using Adaptable Templates," in *Proceedings of the IEEE International Joint Conference on Biometrics*, Crystal City, VA, USA, pp. 1-7, 2011. [32]
- N. J. Short, A. L. Abbott, M. S. Hsiao, and E. A. Fox, "Latent Fingerprint Segmentation using Ridge Template Correlation," presented at the IET International Conference on Imaging for Crime Detection and Prevention, London, U.K., pp. 28-34, 2011. [30]
- N. J. Short, A. L. Abbott, M. S. Hsiao, and E. A. Fox, "Reducing Descriptor Measurement Error through Bayesian Estimation of Fingerprint Minutia Location and Direction," *IET Biometrics,* vol. 1, no. 1, pp. 82-89, 2012. [31]
- N. J. Short, A. L. Abbott, M. S. Hsiao, and E. A. Fox, "Robust Feature Extraction in Fingerprint Images using Ridge Model Tracking," in *Proceedings of IEEE International Conference on Biometrics: Theory, Application, and Systems (BTAS)*, Arlington, VA, pp. 1-6, 2012. [29]

- N. J. Short, A. L. Abbott, M. S. Hsiao, and E. A. Fox, "Temporal Analysis of Fingerprint Impressions," in *Proceedings of IEEE International Conference on Biometrics: Theory, Application, and Systems (BTAS)*, Arlington, VA, pp. 1-6, 2012. [35]

A summary of this dissertation is provided below.

In Chapter 1, we introduced some popular modalities for human identification and outlined basic concepts that apply to all. In this chapter, we highlighted the fingerprint as being one of the oldest and most commonly used traits. We provided an explanation for the formation, acquisition, and representation of fingerprint images. A brief overview of common features found in a fingerprint and how they are used for analyzing prints was provided. Finally, we introduced the reader to the standard performance assessment methodology used for characterizing a biometric algorithm's performance.

Chapter 2 delivered more detail on the fingerprint, outlining the three levels of detail and provided examples of features that are found in each. Here, we looked beyond minutiae to a set of extended features that can be used to facilitate minutia-only based matching by increasing the discriminatory power of the entire set of features found in unique fingerprints. Finally, we discussed existing standards for representing all fingerprint features and the importance of standardized representation to promote interoperability.

Chapter 3 focused on the feature extraction stage of fingerprint analysis, including segmentation and enhancement of the fingerprint region, and detection and refinement of features contained in the fingerprint. In [30], we expanded the topic of segmentation and quality analysis to focus on low quality fingerprints with structured backgrounds. Also in this chapter, we have introduced methods for feature extraction in low reliability regions. This topic was covered in [29]. Experiments showed that the proposed ridge line tracking routine led to better match performance when compared to two long standing methods for extraction. The improvements were most significant for the low quality fingerprint images; however, fingerprints of all quality levels witnessed an increase in match accuracy. We also proposed a grayscale method for refining minutiae position and direction after initial extraction, which was also

described in [31, 32]. The results led to lower error in minutia position and were shown to be statistically significant.

Chapter 4 explores the use of extended features, namely fingerprint ridge components. A graph-based representation, originally introduced in [33], is proposed that represents the minutiae as nodes and the ridges as edges. Using this model, we create ridge clusters and characterize their existence in a typical fingerprint using a large database (see Appendix C). In addition, we have proposed a scheme for representing ridge components as a combination of cubic splines and linear splines, which allows for mathematical analysis of points along the curve.

In Chapter 5, we introduced a similarity measure between fingerprints and its implications on sufficiency. A minutia based similarity measure is extended to include ridge connections between minutiae. We have shown that a reduction in friction ridge surface, and consequently minutiae count, leads to a lower identification rate. Similarity score distributions for genuine matches and imposter matches are shifted closer together, leading to the conclusion that minutiae alone are insufficient for identifying partial prints with low minutiae counts. In [34], we discuss additional methods utilizing topological ridge information which led to a more accurate description of the sufficiency of a set of features found in a fingerprint region.

Finally, in Chapter 6 we introduce a novel approach to fingerprint analysis aimed toward reducing the effects of local quality variation during an image capture. This method, originally proposed in [35], captures a sequence of fingerprint images collected during a single impression of a fingertip. With a dynamic representation of a fingertip, temporal analysis is proposed that leads to an addition in reliable minutiae and improvement in identification over a traditional static fingerprint capture. We propose a model for determining existence and type of minutiae, based on the temporal analysis. In addition, we observe a high number of minutiae that change type throughout the sequence.

The main contributions of this thesis are:

- A ridge tracking algorithm based on Bayesian estimation for extraction of minutiae and ridges in low quality regions. A benefit of the proposed method is the ability to deal with regions where the ridge flow direction is unreliable or unavailable.

Significantly, the feature extraction routine led to an improvement in matching accuracy for low quality fingerprint images as well as an improvement in verification for all fingerprint quality levels.

- A method for reducing the variance in minutia descriptors after initial detection from independent extraction routines, including location and direction.
- Experimental results that demonstrated improvement of the proposed ridge tracking method over two traditional feature extraction approaches. The proposed method improved performance of two well-known fingerprint matchers.
- A method for extracting and representing topological ridge information from a fingerprint image, describing the inter-relationship among minutiae as a graph structure. We proposed a ridge connection descriptor for minutiae adjacent to a similar ridge; the set of all such connections led to a graph-based representation of a fingerprint.
- A representation of fingerprint ridge line structure using cubic splines; we showed that a combination of cubic and linear spline representation leads to better approximations.
- An extension to a minutia-based similarity measure to include ridge clusters. The extended measure led to an improvement in the rarity of a set of partial prints, which has been indicated by an increase in intra-class similarity and a decrease in inter-class similarity when compared to a database of rolled prints.
- A novel method for temporal analysis of fingerprint image sequences. We proposed the use of an entire sequence of images captured during enrollment. A database of enrollment sequences was collected and observations were made. It was observed through experimentation that a large number of minutiae appear and disappear from the foreground during image capture and are no longer present or reliable in the final static image. In addition, we found that almost 20% of minutiae change type at some point during the acquisition process due to increased pressure; we proposed a method to reduce the variation in minutia type. A system and method is proposed for collection, analysis, and fusion of data from a sequence of images taken during a fingerprint impression. The temporal analysis led to higher counts of reliable

minutiae than were found from static analysis of the same impressions. Temporal analysis led to increased accuracy when identifying partial prints.

- Proposed a novel dynamic representation of fingerprints by collecting a sequence of images taken during the entirety of the enrollment impression. We proposed a scheme for collection and have created a preliminary database of fingerprint impression sequences.
- Created a database of synthetic partial prints to support research in partial to full print matching. Currently, only one realistic database of 258 partial fingerprint images with matching genuine full prints exists. We created a database of partial prints by extracting from a database of full prints. The partial prints are analyzed, modeled, and synthesized so that their minutia count distributions and fingerprint area statistics follow similar distributions to those observed "in nature".

Reduced image quality, small overlapping region, and processing time continue to make partial to full fingerprint matching a non-trivial task. In some cases, tackling these problems will continue to require input from human experts. However, we have provided useful methods that help make the most of all features existing in the partial print. These methods provide the ability to obtain an optimal sample for enrollment which leads to a higher likelihood of finding correspondence with a genuine exemplar print.

Appendix A

Particle Filtering

Given a state and an observation, x and y respectively, Bayesian filtering attempts to estimate an unknown target state distribution of a system over time, denoted x_t, from the past and current observational measurements, $y_{1:t}$, and the previous state, x_{t-1}. In other words, we want to recursively estimate the posterior

$$p(x_t|y_t) \propto p(y_t|x_t)p(x_t|y_t, x_{t-1}), \qquad \text{(A.1)}$$

where $p(x_t|y_{t-1}, x_{t-1})$ defines the system dynamics and $p(y_t|x_t)$ represents the system observation.

If the posterior has a known distribution, the expectation of the state at time t is given by

$$E[x_t|y_t] = \int x_t \, p(x_t|y_t) dx_t. \qquad \text{(A.2)}$$

However, when the dynamic system is non-parametric, non-linear, or intractable, an exact solution is unlikely to be feasible. In such a case, the distribution can be approximated by a set of random samples and associated importance weights obtained from Sequential Monte Carlo (SMC) sampling. This type of filtering is known as particle filtering [92], bootstrap filtering [93],

and in the vision community as the Condensation algorithm [94]. The algorithm has been shown to exhibit robust performance for tracking objects against noisy backgrounds.

We can approximate the posterior distribution of x_t with a point-mass function,

$$\hat{p}(x_t|y_t) = \frac{1}{K}\sum_{i=1}^{K} \delta_{x_t^{(i)}}(x_t), \tag{A.3}$$

where δ is the Dirac delta function and $x_t^{(i)} \sim p(x_t|y_t)$.

With a large sample size, K, we can conclude that the approximation converges. This assumes, however, that the distribution is known. If the posterior is unknown, it can be approximated by a set of properly weighted random samples drawn from a known proposal distribution, $\pi(x_t|y_t, x_{t-1})$. In this case, Eqn. A.2 reduces to a simple weighted average of the sample weights,

$$E[x_t|y_t] = \sum_{i=1}^{K} \widehat{\omega}_t^{(i)} x_t^{(i)}, \tag{A.4}$$

and the variance can be approximated by

$$Var(x_t|y_t) = \sum_{i=1}^{K} \widehat{\omega}_t^{(i)} \left(x_t^{(i)} - E[x_t|y_t]\right)^2 \tag{A.5}$$

where $\widehat{\omega_t} = \{\widehat{\omega}_t^{(i)}\}$ is a set of normalized importance weights. These weights, before normalization, are found and propagated by the following update equation:

$$\omega_t^{(i)} = \omega_{t-1}^{(i)} \frac{p\left(y_t \middle| x_t^{(i)}\right) p\left(x_t^{(i)} | x_{t-1}^{(i)}\right)}{\pi\left(x_t^{(i)} | y_{1:t}, x_{0:t-1}^{(i)},\right)}. \tag{A.6}$$

The prior, $\pi(\cdot)$, is taken as a normal transition prior, $p(x_t|x_{t-1})$, for simplicity in traditional particle filters. This reduces Eqn. A.6 to

$$\omega_t^{(i)} = \omega_{t-1}^{(i)} p\left(y_t \middle| x_t^{(i)}\right). \tag{A.7}$$

In order to avoid the problem of degeneracy, where one particle begins to dominate the others due to varying weights, a Sampling Importance Resampling (SIR) particle filter is used, as described by Arulampalam et al. [95] and outlined in Table A-1. In Table A-2, a resampling algorithm is shown that avoids degeneracy, where CDF($\hat{\omega}_t^i$) is the Cumulative Distribution Function of the normalized weights and $U[0, N_s^{-1}]$ is the uniform distribution on the respective bounds. This particular resampling algorithm will remove sample points that have small weights, relative to the set, and replace them with other samples from the set.

Table A-1: SIR particle filter algorithm for minutia localization

SIR_PARTICLE_FILTER
for i= 1:N_s
Sample $P_t^i \sim p(P_t|P_{t-1}^i)$
Determine $\omega_t^i = p(O_t|P_t^i)$
end
Normalize sample weights: $\hat{\omega}_t^i = \frac{\omega_t^i}{\sum_{i=1}^{N_s} \omega_t^i}$
Resample P_t^i, $\hat{\omega}_t^i$

Table A-2: Resampling algorithm

RESAMPLE
C=CDF($\hat{\omega}_t^i$)
Let k=1, and draw starting point $u_1 \sim U[0, N_s^{-1}]$
for j=1:N_s
$u_j = u_1 + N_s^{-1} * (j-1)$
while $u_j > c_i$
k=k+1
end while
$P_t^{j*} = P_t^k$
$\hat{\omega}_t^i = N_s^{-1}$
end

Appendix B

Kalman Filter for Minutia Tracking

A Kalman filter is a state estimator for a given system using a series of noisy observational measurements over time. Like any estimator, the Kalman filter is divided into two stages, a prediction stage and a correction stage. As Figure B-1 (a) indicates, the process of predicting and correcting the system at time t is iterative. In the prediction stage, the current state of the system, x_t, is estimated, and once the current measurement is observed, the estimates are updated. The algorithm runs in real-time, due to the recursive nature of the filter and only relies on the measurement y_t and the previous state estimation, x_{t-1}; no past measurements are needed. The Kalman estimate of the system state maximizes the a posteriori probability of the previous state models and the current measurements.

The Kalman filter, as shown in Figure B-1 (b), takes the prior knowledge we have on previous states and measurements of the system, $p(x_k|x_{k-1}, y_{k-1})$, and combines it with the current measurement, $p(y_k|x_k)$, shown in black. For simplicity, the transition prior, $p(x_k|x_{k-1})$, shown in blue, is traditionally used as the prior. Resulting from the prior information and current measurement, we obtain the posterior estimate for the current state of the system, $p(x_k|y_k)$, shown in green. One restriction of the Kalman filter is that it is a linear system and has noise that can be modeled with a Normal distribution. The prior, $N(x_{t-1}, \sigma_{t-1})$, represents what we know about the system up to time t. The observation function, $N(y_t, \sigma_t)$, represents the state of the system that we measured at the current time t. The final posterior distribution, $N(\hat{x}_t, \hat{\sigma}_t)$ models what we now know about the system based on the prior state estimate and current

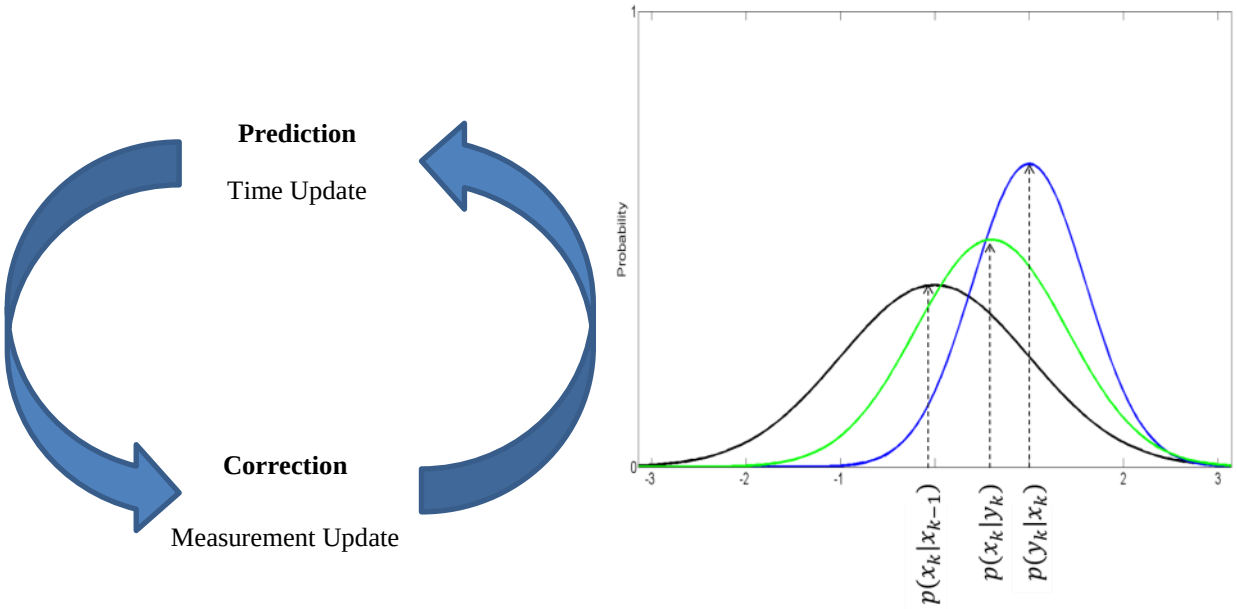

(a) (b)

Figure B-1: (a) Diagram describing the iterative two-stage estimator where a predication is made based on prior data and then updated using latest measurements. (b) A typical Kalman filter combining prior knowledge in black with current measured observation in blue to produce a new estimate model shown in green. All distributions are modeled as normal distributions.

measurements. This posterior distribution represents the best estimate of the current state of the system. The parameters σ_{t-1}, σ_t, and $\hat{\sigma}_t$ represent the uncertainties in the prior, observation, and posterior values, respectively.

The probability density of two measurements, both coming from Normal distributions, can be combined into one estimate by the product of the two probability densities:

$$p(x) = p_1(x)p_2(x) \tag{B.1}$$

where

$$p_i(x) = \frac{1}{\sqrt{2\pi\sigma_i^2}} e^{-\frac{(x-\bar{x}_i)^2}{2\sigma_i^2}}. \tag{B.2}$$

Here, $i = 1,2$ and represents the two distributions independently. Substituting Eqn. B.2 into B.1, we get:

$$p_{12}(x) \propto e^{-\frac{(x-\overline{x_1})^2}{2\sigma_1^2}} e^{-\frac{(x-\overline{x_2})^2}{2\sigma_2^2}} \tag{B.3}$$

Combining the two exponents and expanding the quadratics, we have:

$$p_{12}(x) \propto e^{-\frac{(x-\overline{x_1})^2}{2\sigma_1^2}+\frac{(x-\overline{x_2})^2}{2\sigma_2^2}} \tag{B.4}$$

Let

$$\alpha = \frac{(x-\overline{x_1})^2}{2\sigma_1^2} + \frac{(x-\overline{x_2})^2}{2\sigma_2^2}, \tag{B.5}$$

after rearranging and expanding, we have:

$$\alpha = \frac{x^2 - 2\frac{\overline{x_1}\sigma_2^2+\overline{x_2}\sigma_1^2}{\sigma_1^2+\sigma_2^2}x + \frac{\overline{x_1}^2\sigma_2^2+\overline{x_2}^2\sigma_1^2}{\sigma_1^2+\sigma_2^2}}{2\frac{\sigma_1^2\sigma_2^2}{\sigma_1^2+\sigma_2^2}}. \tag{B.6}$$

Given the normal observation distribution and conjugate prior, it follows that the posterior distribution is also normal. From Eqn. B.6, we see a quadratic form and find the mean and variance for our posterior:

$$p(x_t|y_t) \sim N\left(\frac{x_1\sigma_2^2 + x_2{\sigma_1}^2}{\sigma_1^2+\sigma_2^2}, \frac{\sigma_1^2\sigma_2^2}{\sigma_1^2+\sigma_2^2}\right) \tag{B.7}$$

It follows that our state estimation can be iteratively updated by combining the mean and variance for the prior and observation distributions as in Eqn. B.7, where $x_{t-1} = x_1, \sigma_{t-1}^2 = \sigma_1^2, y_t = x_2$, and $\sigma_2^2 = \sigma_t^2$.

In Figure B-2, a graphical model is shown describing the state-space model for the tracking filter created for each minutia in the fingerprint sequence. Here, I_t is the input fingerprint image at time t. The state estimation is represented by x_t^i, $i = 1,2,..N$, where N is the number of minutiae detected in the image sequence through time t. Lastly, y_t^i is the measured observation of the location of minutia i, typically a measure of grayscale information in the region of interest. The edges in the graph designate conditional dependencies, where the non-existence of an edge between two nodes indicates that two variables are conditionally independent.

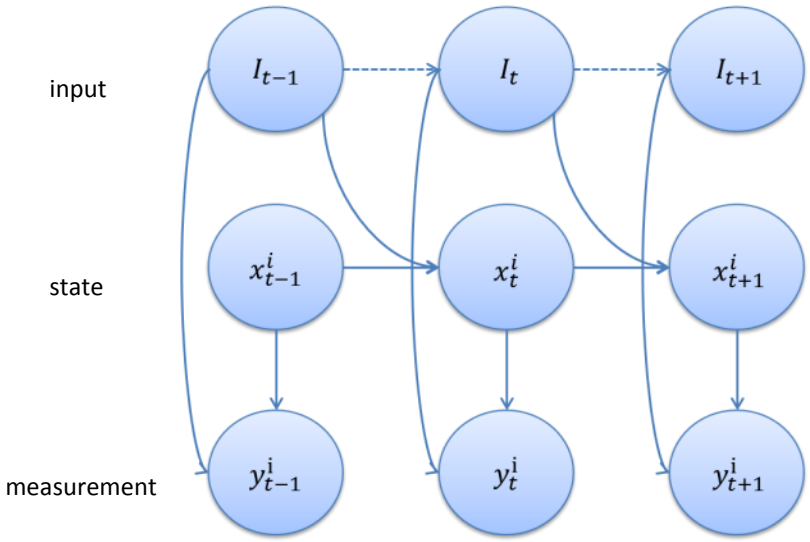

Figure B-2: Graphical model of minutia position state-space model.

Appendix C

FBI Fingerprint Database

This appendix describes the fingerprint database that was used to derive many of the fingerprint feature characteristics in this work. The database was provided by the FBI CJIS. The database contained 117,323 rolled and plain fingerprint images, of which, the 83,815 rolled fingerprint images were used for analysis. A total of 9,675 images were removed for various reasons, such as low quality, too many spurious minutiae, or no friction ridge information available. This reduced the collection to 74,140 from which there were 2,575 different subjects providing multiple impressions of 23,942 unique fingerprints. The distribution of samples provided by each of the subjects is described in Figure C-1

The images were further grouped into four groups, Very Good, Good, Bad, and Ugly as determined by the global image quality score assigned by VeriFinger SDK [66]. This information is summarized in Table C-1 below, where the quality level range is from 0-100. The value represented by N corresponds to the number of samples in each quality group, $\bar{X}$ and σ are the average and standard deviation for the quality measure of each group. The minutiae distributions are reported below in Figure C-2 for each quality group, only minutiae greater than a quality of 40 (with 100 being the highest quality) were used as reliable minutiae.

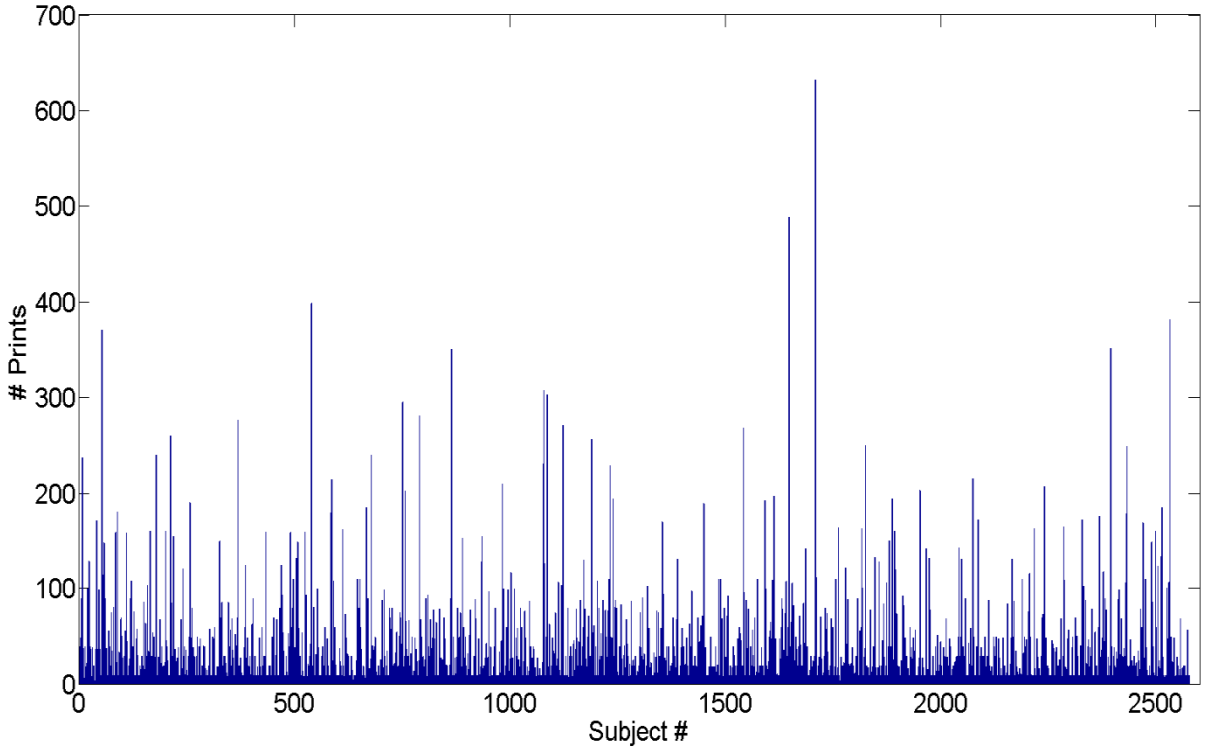

Figure C-1: Distribution of fingerprint samples provided by each subject in the FBI Fingerprint Database.

Table C-1: Summary of images contained in FBI Fingerprint Database.

Group	Quality Level	N	$\bar{X}$	σ
Very Good	(75-100)	59,673	98.3	5.0
Good	(50-75]	6,836	63.2	7.2
Bad	(25-50]	5,042	38.4	7.2
Ugly	(0-25]	2,589	12.6	8.1

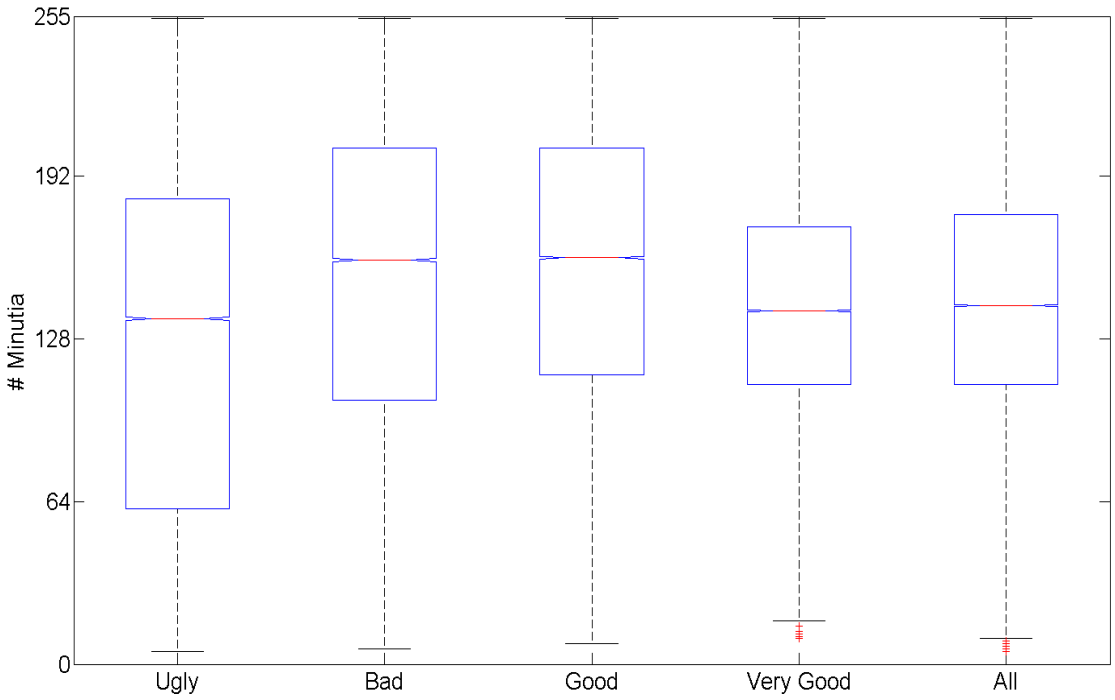

Figure C-2: Box and whisker plot indicating minutia counts for the different fingerprint quality groups.

Appendix D

Digital Media

A collection of digital media were created as visual support for some of the methods developed throughout this dissertation. In this appendix, we describe the additional media files uploaded with the dissertation. All videos have been compressed using the MPEG-4 format and can be downloaded along with this dissertation.

Short_NJ_D_2012_F1

This video describes the process outlined in Chapter 4 for robust fingerprint feature extraction. The demo shows the ridge position during a single step of the tracking process, r_t. Samples are drawn from a prior distribution, $p(\theta_t|\theta_{t-1})$. Weights are measured for each sample using the weighting function, $g(\cdot)$. A cross correlation score between the observed region and an ideal ridge template is used as input to the weighting function. Finally, the current direction is approximated from the posterior distribution. The expected direction, $E[\theta_t|\omega_t]$, calculated from the set of samples and associated weights, is used to update the ridge tracking point, r_{t+1}.

Short_NJ_D_2012_F2

In this video, an example of a sequence of images collected during a fingerprint impression is shown. The capture is taken from the instant the fingertip first touches the sensor until the capture process ends and shows how more surface area is detected by the sensor as the finger is applied. Also, the effect of increasing pressure on skin elasticity is shown, where as a result, the ridges spread away from the center of contact. This video is not representative of the database sequences collected in Chapter 6, but is slowed down to show the distortion more dramatically. As a result of ridges spreading and merging into each other, ridge terminations detected early in the sequence can turn to ridge bifurcation later in the sequence.

Short_NJ_D_2012_F3

This video shows the spline approximation to the skeleton ridge image representation of the same fingerprint impression from the *Short_NJ_D_2012_F2* video. The red spline approximation represents the first image in the sequence and the blue ridges represent the updated spline approximation as the fingerprint impression sequence progresses. In this video, the degree to which the ridges spread apart from increased pressure is apparent. By the end of the video, some of the ridges can be seen displaced an entire ridge peak-to-peak distance from its original position at the beginning of the sequence. Also, minutia type can be seen changing as some ridge endings become connected to neighboring ridges throughout the sequence.

Short_NJ_D_2012_F4

An entire impression sequence from the database collected as part of Chapter 6 is shown from beginning to end. In this video, it can be seen how the quality of the fingerprint varies from the beginning of the sequence to the end. In the first image, the ridge clarity at the center of the image is well defined, however, by the end of the sequence the ridge clarity at the center of contact has deteriorated. Conversely, as the sequence progresses, more sequence, more fingerprint surface area is visible toward the outer region of the print than is visible in earlier images. Using Temporal Analysis, we can combine all of this data to create a single template that benefits from the reliability of the center area earlier in the sequence and the additional features from the outer region of the finger detected in the images later in the sequence. Also

shown in this video is the skeleton representation extracted using Neurotechnology's VeriFinger for each of the fingerprint images in the sequence. The ridge skeleton further demonstrates the deterioration of the fingerprint image as the sequence progresses.

Short_NJ_D_2012_F5

The result of temporal analysis on a fingerprint impression sequence from the database in Chapter 6 is shown. The minutiae detected in each fingerprint image in the sequence are indicated by green circles (terminations), blue squares (bifurcations), and red circles (missing). In this demo, the red circles indicate minutia that were not detected in the current image of the sequence. In this example, all images in the sequence were found to be maximum quality by the VeriFinger quality assessment tool. At the end of the impression sequence, all of the minutiae marked in red are missing from the final image. There are two possibilities for why a minutiae would be missing: 1) the corresponding friction ridge surface area is no longer in contact with the sensor or 2) the friction ridge surface area from which the minutia was detected is no longer reliable. In a traditional fingerprint capture, these minutiae would not be included in the final template.

Short_NJ_D_2012_F6

A demonstration of the Kalman filter tracking for determining correspondences of minutiae throughout a fingerprint impression sequence is shown. In this sequence, the blue filled in circles indicate the positions of the minutiae in the previous image, $t-1$. The green circles indicate the predicted position of each minutia in the current image in the sequence at time t. The radius of the circle outlines the search space for a corresponding minutia. The red filled in circle indicates the measured position of the minutiae in the current image at time t. If the red circle is measured within a distance less than the radius of the predicted position, the minutia is marked as corresponding with the minutia form the previous image.

Short_NJ_D_2012_F7

This animation depicts a fingerprint card where fingerprint impressions are represented by dynamic sequences. The card shows the impression sequences for all ten rolled fingerprint

images, left/right four finger slaps, and left/right thumb slaps. This video shows the additional amount of information available in a fingerprint sequence as opposed to a single static fingerprint image representation.

References

[1] Fulcrum Biometrics. (2012, September 12). *i3 digID Mini*. Available: http:// www.fulcrumbiometrics.com/i3-DigID-Mini-p/101262.htm

[2] G. Gulick. (2008) Can You Find It? *Evidence Technology Magazine*. vol. 6, no. 3.

[3] American National Standards Institute/ National Institute of Standards and Technology, "Data Format for the Interchange of Fingerprint, Facial & Other Biometric Information," ed: NIST Special Publication 500-290, 2011.

[4] D. Maltoni, D. Maio, A. K. Jain, and S. Prabhakar, *Handbook of Fingerprint Recognition*. London: Springer-Verlag, 2009.

[5] Yi Chen, "Extended Feature Set and Touchless Imaging for Fingerprint Matching," Doctor of Philosophy Dissertation, Department of Computer Science, Michigan State University, 2009.

[6] R. Yen and J. Guzman, "Fingerprint Image Quality Measurement Algorithm," *Journal of Forensic Identification*, vol. 57, no. 2, pp. 274-287, 2007.

[7] National Institute of Justice, *The Fingerprint Sourcebook*. Washington, D.C.: U.S. Department of Justice, 2010.

[8] National Institute of Standards and Technology. (2012). *Fingerprint Minutiae from Latent and Matching Tenprint Images*. Available: http://www.nist.gov/srd/nistsd27.htm

[9] Z. Xiang-Xin and L. Chun-Ge, "The Historical Application of Hand Prints in Chinese Litigation," *Journal of Forensic Identification*, vol. 38, pp. 277-284, 1988.

[10] H. Cummins and C. Midlo, *Finger Prints, Palms and Soles: An Introduction to Dermatoglyphics*. New York: Dover, 1943.

[11] H. H. Wilder and B. Wentworth, *Personal Identification*. Boston: The Gorham Press, 1918.

[12] F. Galton, *Finger Prints*. London: Macmillan, 1892.

[13] E. Henry, *Classification and Uses of Fingerprints*. London: Routledge and Sons, 1900.

[14] Ewen Callaway. (2009). *Get a grip: Truth about fingerprints revealed*. Available: http://www.newscientist.com/article/dn17300-get-a-grip-truth-about-fingerprints-revealed.html

[15] Federal Bureau of Investigation. (2011). *Recording Legible Fingerprints*. Available: http://www.fbi.gov/about-us/cjis/fingerprints_biometrics/recording-legible-fingerprints/takingfps

[16] FBI Center of Excellence, "Electronic Biometric Transmission Specification Version 9.3," 2011. Available: https://www.fbibiospecs.org/docs/EBTS_v9_3_Final%2012_07_11_clean.pdf

[17] Identification International Inc. (2010). *The World's Most Portable Live Scan*. Available: http://www.idintl.com/products/index.html

[18] Identification International Inc., "digID Mini Brochure: Forensic Live Scan Device," ed, 2012.

[19] Physical Evidence Program Manager, "Latent Print Procedures Manual," *DFS document 241-D100*, pp. 1-56, 2012. Available: http://www.dfs.virginia.gov/manuals/latentPrints/procedures/241-D100%20Latent%20Print%20Procedures%20Manual.pdf

[20] E. R. Menzel and J. M. Duff, "Laser Detection of Latent Fingerprints - Treatment with Fluorescers," *Journal of Forensic Sciences*, vol. 24, no. 1, pp. 96-100, 1979.

[21] H. C. Lee and R. E. Gaensslen, *Advances in Fingerprint Technology* vol. 132296: National Criminal Justice Reference Service, 1991.

[22] H. C. Lee and R. E. Gaensslen, *Cyanoacrylate Fuming: Theory and Procedures*: Connecticut State Police Forensic Science Laboratory, 1984.

[23] Scientific Working Group on Friction Ridge Analysis and Technology. (2010). *Standards for the Documentation of Analysis, Comparison, Evaluation, and Verification (ACE-V).* Available: http://www.swgfast.org/documents/documentation/100310_Standard_Doumentation_ACE-V_1.0.pdf

[24] Federal Bureau of Investigation Center of Excellence. (2012). *Universal Latent Workstation*. Available: https://www.fbibiospecs.org/Latent/LatentPrintServices.aspx

[25] C. Wilson, "Fingerprint Vendor Technology Evaluation 2003: Summary of Results and Analysis Report," presented at the National Institute of Standards and Technology, 2004.

[26] J. Jia, L. Cai, P. Lu, and X. Lu, "Fingerprint Matching Based On Weighting method and the SVM," *Neurocomputing*, vol. 70, no. 4-6, pp. 849-858, 2007.

[27] J. Feng, "Combining Minutiae Descriptors for Fingerprint Matching," *Pattern Recognition*, vol. 41, no. 1, pp. 342-352, 2008.

[28] A. Lumini and L. Nanni, "Advanced Methods for Two-Class Pattern Recognition Problem Formulation for Minutiae-Based Fingerprint Verification," *Pattern Recognition*, vol. 29, no. 2, pp. 142-148, 2008.

[29] N. J. Short, A. L. Abbott, M. S. Hsiao, and E. A. Fox, "Robust Feature Extraction in Fingerprint Images using Ridge Model Tracking," in *Proceedings of IEEE International Conference on Biometrics: Theory, Application, and Systems (BTAS)*, Arlington, VA, pp. 1-6, 2012.

[30] N. J. Short, A. L. Abbott, M. S. Hsiao, and E. A. Fox, "Latent Fingerprint Segmentation using Ridge Template Correlation," presented at the IET International Conference on Imaging for Crime Detection and Prevention, London, U.K., pp. 28-34, 2011.

[31] N. J. Short, A. L. Abbott, M. S. Hsiao, and E. A. Fox, "Reducing Descriptor Measurement Error through Bayesian Estimation of Fingerprint Minutia Location and Direction," *IET Biometrics,* vol. 1, no. 1, pp. 82-89, 2012.

[32] N. J. Short, A. L. Abbott, M. S. Hsiao, and E. A. Fox, "A Bayesian Approach to Fingerprint Minutia Localization and Quality Assessment using Adaptable Templates," in *Proceedings of the IEEE International Joint Conference on Biometrics*, Crystal City, VA, USA, pp. 1-7, 2011.

[33] N. J. Short, A. L. Abbott, M. S. Hsiao, and E. A. Fox, "Extraction of Hierarchical Extended Features in Fingerprint Images," presented at the CESCA 2010-001, Blacksburg, VA, 2010.

[34] K. Hoyle, N. J. Short, M. S. Hsiao, A. L. Abbott, and E. A. Fox, "Minutiae + Friction Ridges = Triplet-Based Feature for Determining Sufficiency in Fingerprints," presented at the IET International Conference on Imaging for Crime Detection and Prevention, London, U.K., pp. 2-9, 2011.

[35] N. J. Short, A. L. Abbott, M. S. Hsiao, and E. A. Fox, "Temporal Analysis of Fingerprint Impressions," in *Proceedings of IEEE International Conference on Biometrics: Theory, Application, and Systems (BTAS)*, Arlington, VA, pp. 1-6, 2012.

[36] Y. He, R. Kohno, and H. Imai, "A Fast Automatic Fingerprint Identification Method Based on a Weighted-Mean of Binary Image," *IEICE Transactions on Fundamentals of Electronics, Communications, and Computer Sciences,* vol. E76-A, no. 9, pp. 1469-1482, 1993.

[37] D. Roberge, C. Soutar, and B. V. K. V. Kumar, "Optimal Trade-Off Filter for the Correlation of Fingerprints," *Optical Engineering,* vol. 38, no. 1, pp. 108-113, 1999.

[38] K. Venkataramani and B. V. K. V. Kumar, "Fingerprint Verification Using Correlation Filters," in *Proceedings of International Conference on Audio- and Video-Based Biometric Person Authentication*, Guildford, UK, pp. 886-895, 2003.

[39] K. Venkataramani and B. V. K. V. Kumar, "Performance of Composite Correlation Filters in Fingerprint Verification," *Optical Engineering,* vol. 43, no. 8, pp. 1820-1827, 2004.

[40] C. I. Watson and D. P. Casasent, "Recognition of Live-Scan Fingerprints with Elastic Distortions Using Correlation Filters," *Optical Engineering*, vol. 43, no. 10, pp. 2274-2282, 2004.

[41] C. I. Watson and C. L. Watson, "Effect of Image Size and Compression on One-to-One Fingerprint Matching," 2005.

[42] D. R. Ashbaugh, *Quantitative-Qualitative Friction Ridge Analysis: An Introduction to Basic and Advanced Ridgeology*: CRC Press, 1999.

[43] C. Wilson, G. Candela, and C. Watson, "Neural Network Fingerprint Classification," *Artificial Neural Networks*, vol. 1, no. 2, pp. 203-228, 1993.

[44] C. Champod, C. Lennard, P. Margot, and M. Stoilovic, *Fingerprints and Other Ridge Skin Impressions*: CRC Press, 2004.

[45] Criminal Justice Information Services, "Electronic Biometric Transmission Specification," ed: Federal Bureau of Investigation, 2011.

[46] National Institute of Standards and Technology. (2005). *Proprietary Fingerprint Template (PFT) Testing*. Available: http://fingerprint.nist.gov/SDK/

[47] National Institute of Standards and Technology. (2012). *Committee to Define an Extended Fingerprint Feature Set (CDEFFS)*. Available: http://fingerprint.nist.gov/standard/cdeffs/

[48] Scientific Working Groups. (2012). *Scientific Working Group on Friction Ridge Analysis, Study, and Technology (SWGFAST)*. Available: http://www.swgfast.org/

[49] National Institute of Standards and Technology. (2012). *National Institute of Standards and Technology's Biometric Image Software (NBIS)*. Available: http:// fingerprint.nist.gov/NFIS/

[50] US-VISIT, "Enhancing Security Through Biometric Identification," presented at the U.S. Department of Homeland Security, 2012.

[51] K. Zetter. (2009) FBI Processes 600 Billion Fingerprint Sets a Day. *Wired*. Available: http://www.wired.com/threatlevel/2009/07/fbifingerprints/

[52] A. K. Jain, L. Hong, and R. Bolle, "On-line Fingerprint Verification," *IEEE Transactions on Pattern Analysis and Machine Intelligence,* vol. 19, no. 4, pp. 302-314, 1997.

[53] D. Maio and D. Maltoni, "Direct Gray-Scale Minutiae Detection in Fingerprints," *IEEE Transactions on Pattern Analysis and Machine Intelligence,* vol. 19, no. 1, pp. 27-40, 1997.

[54] R. Gonzalez and R. Woods, *Digital Image Processing* vol. 3: Prentice Hall, 2008.

[55] J. Liu, Z. Huang, and K. L. Chan, "Direct Minutia Extraction from Gray-Level Fingerprint Image by Relationship Examination," in *Proceedings of the IEEE International Conference on Image Processing*, Vancouver, BC, Canada, pp. 427-430, 2000.

[56] X. Jiang, W. Yau, and W. Ser, "Detecting the Fingerprint Minutiae by Adaptive Tracing the Gray-level Ridge," *Pattern Recognition,* vol. 34, no. 5, pp. 999-1013, 2001.

[57] D. Arpit and A. Namboodiri, "Fingerprint Feature Extraction from Gray Scale Images by Ridge Tracing," in *Proceedings of the IEEE International Joint Conference on Biometrics*, Crystal City, VA, USA, pp. 1-8, 2011.

[58] R. Ma, Y. Qi, C. Zhang, and J. Wang, "A Novel Approach to Fingerprint Ridge Line Extraction," in *Proceedings of the IEEE International Symposium on Communications and Information Technologies*, Beijing, China, pp. 2-5, 2005.

[59] B. M. Mehtre, N. N. Murthy, S. Kapoor, and B. Chatterjee, "Segmentation of Fingerprint Images Using the Directional Image," *Pattern Recognition,* vol. 20, no. 4, pp. 429-435, 1987.

[60] N. K. Ratha, S. Y. Chen, and A. K. Jain, "Adaptive Flow Orientation-Based Feature Extraction in Fingerprint Images," *Pattern Recognition,* vol. 28, no. 11, pp. 1657-1672, 1995.

[61] V. Areekul, U. Watchareeruetai, K. Suppasriwasuseth, and S. Tantaratana, "Separable Gabor Filter Realization for Fast Fingerprint Enhancement," presented at the International Conference on Image Processing, Genoa, Italy, pp. 253-256, 2005.

[62] L. Hong, Y. Wan, and A. K. Jain, "Fingerprint Image Enhancement: Algorithms and Performance Evaluation," *IEEE Transactions on Pattern Analysis and Machine Intelligence*, vol. 20, no. 8, pp. 777-789, 1998.

[63] A. Doucet, "On Sequential Monte Carlo Methods for Bayesian Filtering," University of Cambridge, U. K.1998.

[64] M. S. Arulampalam, S. Maskell, N. Gordon, and T. Clapp, "A Tutorial on Particle Filters for Online Nonlinear/Non-Gaussian Bayesian Tracking," in *Proceedings of the IEEE Signal Processing*, pp. 174-188, 2002.

[65] Q. Xiao and H. Raafat, "Fingerprint Image Post-Processing: A Combined Statistical and Structural Approach," *Pattern Recognition,* vol. 24, no. 10, pp. 985-992, 1991.

[66] Neurotechnology. (2012). *VeriFinger SDK*. Available: http://www.neurotechnology.com

[67] D. G. Ress, *Essential Statistics*: Chapman & Hall, 2001.

[68] X. Luo, J. Tian, and Y. Wu, "A Minutia Matching Algorithm in Fingerprint Verification," in *Proceedings of the IEEE International Conference on Pattern Recognition*, Barcelona, Spain, pp. 833-836, 2000.

[69] J. Feng and A. Cai, "Fingerprint Representation and Matching in Ridge Coordinate System," in *Proceedings of International Conference on Pattern Recognition*, Hong Kong, China, pp. 485-488, 2006.

[70] Y. He, J. Tian, X. Luo, and T. Zhang, "Image Enhancement and Minutiae Matching in Fingerprint Verification," *Pattern Recognition Letters*, vol. 24, no. 9, pp. 1349-1360, 2003.

[71] A. Ross, S. C. Dass, and A. K. Jain, "Fingerprint Warping using Ridge Curve Correspondences," *IEEE Transactions on Pattern Analysis and Machine Intelligence*, vol. 28, no. 1, pp. 19-30, 2006.

[72] J. Feng, Z. Quyang, and A. Cai, "Fingerprint Matching Using Ridges," *Pattern Recognition*, vol. 39, no. 11, pp. 2131-2140, 2006.

[73] A. K. Jain and J. Feng, "Latent Fingerprint Matching," *Transactions on Pattern Analysis and Machine Intelligence*, vol. 33, no. 1, pp. 88-100, 2011.

[74] Bartels, Beatty, and Barsky, *An Introduction to Splines for Use in Computer Graphics and Geometric Modeling*: Morgan Kaufmann, 1995.

[75] A. Newman. (2001, April 07). *Fingerprinting's Reliability Draws Growing Court Challenges* N. Y. Times. Available: http://www.nytimes.com/2001/04/07/us/fingerprinting-s-reliability-draws-growing-court-challenges.html?pagewanted=all&src=pm

[76] National Institute of Standards and Technology, "Forensic Sciences: Review of Status and Needs," Gaithersburg, MD, 1999.

[77] S. Pankanti, S. Prabhakar, and A. K. Jain, "On the Individuality of Fingerprints," *IEEE Transactions on Pattern Analysis and Machine Intelligence,* vol. 24, no. 8, pp. 1010-1025, 2002.

[78] National Institute of Justice, "Forensic Friction Ridge (Fingerprint) Examination Validation Studies," 2000.

[79] J. Chen and Y. S. Moon, "The Statistical Modelling of Fingerprint Minutiae Distribution with Implications for Fingerprint Individuality Studies," in *Proceedings of the IEEE Computer Vision and Pattern Recognition,* Anchorage, AK, USA, pp. 1-7, 2008.

[80] Y. Zhu, S. C. Dass, and A. K. Jain, "Statistical Models for Assessing the Individuality of Fingerprints," *IEEE Transactions on Information Forensics and Security,* vol. 2, no. 3, pp. 391-401, 2007.

[81] C. Su and S. Srihari, "Evaluation of Rarity of Fingerprints in Forensics," in *Proceedings of Advances in Neural Information Processing systems*, Lake Tahoe, NV, USA, pp. 1207-1215, 2010.

[82] Y. Wang and J. Hu, "Global Ridge Orientation Modeling for Partial Fingerprint Identification," *IEEE Transactions on Pattern Analysis and Machine Intelligence,* vol. 33, no. 1, pp. 72-87, 2011.

[83] B. Y. Hiew, A. B. J. Teoh, and Y. H. Pang, "Touch-less Fingerprint Recognition System," in *Proceedings of the IEEE Workshop on Automatic Identification Advanced Technologies*, Alghero, Italy, pp. 24-29, 2007.

[84] G. Parziale, "Touchless Fingerprinting Technology," *Advances in Biometrics,* vol. 1, pp. 25-48, 2008.

[85] K. Choi, H. Choi, S. Lee, and J. Kim, "Fingerprint Image Mosaicking by Recursive Ridge Mapping," *IEEE Transactions on Systems Man and Cybernetics Part B-Cybernetics,* vol. 37, no. 5, pp. 1191-1203, 2007.

[86] K. Choi, H. Choi, and J. Kim, "Fingerprint Mosaicking by Rolling and Sliding," in *Proceedings of Audio and Video Based Biometric Person Authentication*, Rye Brook, NY, USA, pp. 260-269, 2005.

[87] N. Ratha, J. Connell, and R. Bolle, "Image Mosaicing for Rolled Fingerprint Construction," presented at the Pattern Recognition, Brisbane, Qld., AUS, pp. 1651-1653, 1998.

[88] W. Yau, K. Toh, D. Jiang, T. Chen, and J. Lu, "On Fingerprint Template Synthesis," in *Proceedings of International Conference on Control, Automation, Robotics and Vision*, Singapore, pp. 1-6, 2000.

[89] A. Ross, S. Shah, and J. Shah, "Image Versus Feature Mosaicing: A Case Study in Fingerprints," presented at the Conference on Biometric Technology for Human Identification, Orlando, FL, USA, pp. 1-12, 2006.

[90] P. Zarchan and H. Musoff, *Fundamentals of Kalman Filtering: A Practical Approach*. Reston, VA: American Institute of Aeronautics and Astronautics, 2000.

[91] Michael D. Garris and R. Michael McCabe, *NIST Special Database 27: Fingerprint Mintuiae From Latent and Matching Tenprint Images*: U.S. Department of Commerce, 2000.

[92] J. Carpenter, P. Clifford, and P. Fearnhead, "Improved Particle Filter for Non-Linear Problems," *Radar, Sonar, and Navigation*, vol. 146, no. 1, pp. 2-7, 1999.

[93] N. Gordon, D. Salmond, and A. F. M. Smith, "Novel Approach to Non-Linear and Non-Gaussian Bayesian State Estimation," *IET Radar and Signal Processing*, vol. 140, no. 2, pp. 107-113, 1993.

[94] A. Blake and M. Isard, "The CONDENSATION Algorithm - Conditional Density Propogation and Applications to Visual Tracking," *Advances in Neural Information Processing*, vol. 29, no. 1, pp. 5-28, 1996.

[95] M. S. Arulampalam, S. Maskell, N. Gordon, and T. Clapp, "A Tutorial on Particle Filters for Online Nonlienar/Non-Gaussian Bayesian Tracking," *Transactions on Signal Processing*, vol. 50, no. 2, pp. 174-188, 2002.